Hydrogen and halogen bonding in co-crystallization: from fundamentals to applications

by

Manomi Dharshika Perera

B.S., University of Colombo, 2010

AN ABSTRACT OF A DISSERTATION

submitted in partial fulfillment of the requirements for the degree

DOCTOR OF PHILOSOPHY

Department of Chemistry
College of Arts and Sciences

KANSAS STATE UNIVERSITY
Manhattan, Kansas

2017

Abstract

The impact of the molecular electrostatic potential values (MEPs) in halogen and hydrogen bond interactions were explored using two acceptors with multiple acceptor sites with twelve hydrogen-bond donors, five halogen bond donors and four mixed halogen and hydrogen bond donors. The results suggested if the difference between the two acceptor sites is above 38 kJ/mol both hydrogen and halogen bond donors prefer the acceptor site with the highest MEP value and this selectivity was lost if the difference is below 26 kJ/mol.

To examine the potential of halogen-bond donors in organocatalysis, a halogen-bond donor molecule was synthesized and the catalytic activity was measured using a benchmark Ritter type solvolysis reaction. Results suggested the catalytic activity of the halogen-bond donor molecule with > 90 % conversion of the product with the use of a stoichiometric amount of the catalyst for 96 hrs. Successful use of the control molecules confirm that the catalytic activity is an outcome of having halogen-bond donors in the molecule.

The benefit of using a structural mimic in landscaping the structural outcomes of poorly soluble molecules was explored using an anticancer drug erlotinib. A structural mimic was synthesized by maintaining all binding sites that are important to design a structural landscape and the structural outcomes were analyzed using five FDA approved dicarboxylic acids. The results suggested that the structural outcomes of the mimic can be related to the actual drug erlotinib. Solubility and thermal behavior analysis of the co-crystals also suggested that with the systematic changes of the co-crystallization agent, it is possible to make predictable changes to the physical properties.

To observe the effect of co-crystallization technology in reducing the chemical reactivity and sensitivity of an energetic compound dinitrobenzotriazole, a series of co-crystallization

experiments was carried out using fourteen nitrogen and oxygen based acceptors. Four co-crystals were obtained and the acceptors were identified as supramolecular protecting groups which led to successful diminish of chemical instability and decreased impact sensitivity.

Hygroscopicity and chemical reactivity of tetranitrobisimidazole, a potential RDX replacement, was successfully decreased by protecting the acidic N-H protons in the molecule by introducing suitable co-formers. Introduction of the N-oxide based acceptors into the system enhanced the stability while retaining most of the desirable energetic properties.

Hydrogen and halogen bonding in co-crystallization: from fundamentals to applications

by

Manomi Dharshika Perera

B.S., University of Colombo, 2010

A DISSERTATION

submitted in partial fulfillment of the requirements for the degree

DOCTOR OF PHILOSOPHY

Department of Chemistry
College of Arts and Sciences

KANSAS STATE UNIVERSITY
Manhattan, Kansas

2017

Approved by:

Major Professor
Christer B Aakeröy

Copyright

Abstract

The impact of the molecular electrostatic potential values (MEPs) in halogen and hydrogen bond interactions were explored using two acceptors with multiple acceptor sites with twelve hydrogen-bond donors, five halogen bond donors and four mixed halogen and hydrogen bond donors. The results suggested if the difference between the two acceptor sites is above 38 kJ/mol both hydrogen and halogen bond donors prefer the acceptor site with the highest MEP value and this selectivity was lost if the difference is below 26 kJ/mol.

To examine the potential of halogen-bond donors in organocatalysis, a halogen-bond donor molecule was synthesized and the catalytic activity was measured using a benchmark Ritter type solvolysis reaction. Results suggested the catalytic activity of the halogen-bond donor molecule with > 90 % conversion of the product with the use of a stoichiometric amount of the catalyst for 96 hrs. Successful use of the control molecules confirm that the catalytic activity is an outcome of having halogen-bond donors in the molecule.

The benefit of using a structural mimic in landscaping the structural outcomes of poorly soluble molecules was explored using an anticancer drug erlotinib. A structural mimic was synthesized by maintaining all binding sites that are important to design a structural landscape and the structural outcomes were analyzed using five FDA approved dicarboxylic acids. The results suggested that the structural outcomes of the mimic can be related to the actual drug erlotinib. Solubility and thermal behavior analysis of the co-crystals also suggested that with the systematic changes of the co-crystallization agent, it is possible to make predictable changes to the physical properties.

To observe the effect of co-crystallization technology in reducing the chemical reactivity and sensitivity of an energetic compound dinitrobenzotriazole, a series of co-crystallization

experiments was carried out using fourteen nitrogen and oxygen based acceptors. Four co-crystals were obtained and the acceptors were identified as supramolecular protecting groups which led to successful diminish of chemical instability and decreased impact sensitivity.

Hygroscopicity and chemical reactivity of tetranitrobisimidazole, a potential RDX replacement, was successfully decreased by protecting the acidic N-H protons in the molecule by introducing suitable co-formers. Introduction of the N-oxide based acceptors into the system enhanced the stability while retaining most of the desirable energetic properties.

Table of Contents

List of Figures

List of Tables

Acknowledgements

I would like to express my deepest gratitude to my advisor, Professor Christer Aakeröy for accepting me into his group and for his continual guidance, encouragement and motivation over the last five years. Your persuasion made me a confident individual and under your shadow I learned a lot to become a better presenter and a writer. You were always there to listen and showed the right direction whenever I feel lost. The invaluable lessons I learnt from you about science and life guided me to think differently and I will always follow the path you showed me. Thank you for being a wonderful advisor and it had been a great privilege to work with you.

I would also like to thank my Ph.D advisory committee, Professor Paul Smith, Professor James Edgar, Professor Tendai Gadzikwa and Professor Om Prakash for their valuable time and inputs on this dissertation.

I also like to thank Dr. Eric Maatta for being on my committee for three years and for all his support and encouragement.

I am grateful to Dr. John Desper and Dr. Abhijeet Sinha for providing nice crystal structures and without you two most of my chapters would not have been possible.

I would like to extend my gratitude to Dr. Christopher Levy and Dr. Kenneth Klabunde for being wonderful teachers and increasing my interest towards inorganic chemistry.

Thanks to Dr. Leila Maurmann for helping me with NMR studies and being a good friend who I always enjoyed spending time with.

Thanks to Ron Jackson for the help in fixing broken instruments and thanks to you things proceeded much efficiently and smoothly.

I also would like to thank Dr. Yasmin Patell, Mr. Jim Hodgson, Mr.Tobe Eggers, Ms. Mary Dooley and Ms. Kimberly Ross for making my research life easy at K-State.

Thanks to Dr. Earline Dikeman and Dr. Michael Hinton for helping and guiding me to become a better teacher

A special thank goes to Dr. Dhanushi Welideniya for mentoring and motivating me and showing how to set up reactions correctly.

Thank you all the past and present Aakeröy group members for the endless support and for all the fun time we had together. It was so easy to work in the lab because of all of you.

I am very thankful to all my friends in Manhattan who were there in all the good and bad times. Among you I never felt I am away from my home and the time we spend together is amazing. Thank you for your care during my hard times.

I am very grateful to my loving parents who supported me to come this far. The strength and love you gave me made who I am today. I am thankful to my loving brothers who were always there to cheer me up and knowing that you both are there to help me always gives me confidence.

Last but not least I want to thank my loving husband for his endless love and support from the day we met. No one would have done the things you did for me and without you it would not have been easy to reach this far. Thanks for being such a caring, loving and a supporting husband.

Dedication

To my loving husband for his endless love and the strength he gave me

Chapter 1 - Introduction

1.1 Structure- property relationship of molecules

A fundamental axiom in science and technology is that "form follows function' and in chemistry this is recognized by that the properties and behavior of molecules follow from their structures.[1]A great deal of information about molecular properties can be obtained by observing how atoms in molecules are connected. Nearly seventy years ago pioneering work on structure-property relationships was carried out by Weiner[2] who investigated the properties of hydrocarbons and recognized that properties change with molecular bulk and branching.[2, 3] Since then, structure-property relationships have long guided the discovery and optimization of novel materials.[4] Studies of structure-property relations in organic molecules can be divided into two main categories. Under the first category, bulk properties of materials were analyzed based on the presence of strong interactions between molecules. Under the second category, properties were analyzed based on the variations on the molecular structure (Figure 1-1).[5]

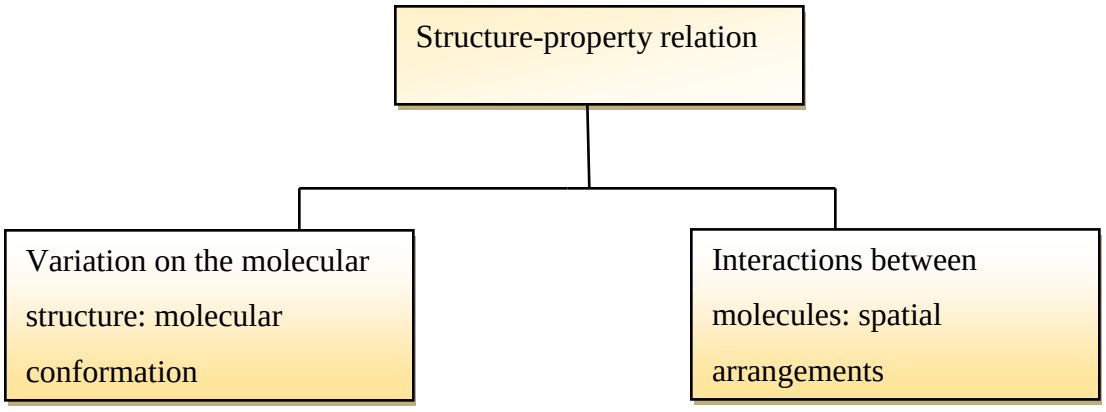

Figure 1-1 Two main categories of structure-property relation in organic molecules

A study of melting point changes of dicarboxylic acids provides an example of the influence of both intermolecular interactions and structural conformation in the structure-property relationship.[6] Figure 1-2 shows the correlation of the melting points of the even chain dicarboxylic acids. With the addition of even number of carbon atoms into the chain, melting points were gradually decreased. However as soon as a dicarboxylic acid with an odd number of carbon atoms in the chain was introduced this correlation was no longer observed. Even and odd chain length dicarboxylic acids have difference in structural conformation which leads to different spatial arrangements (Figure 1-3).

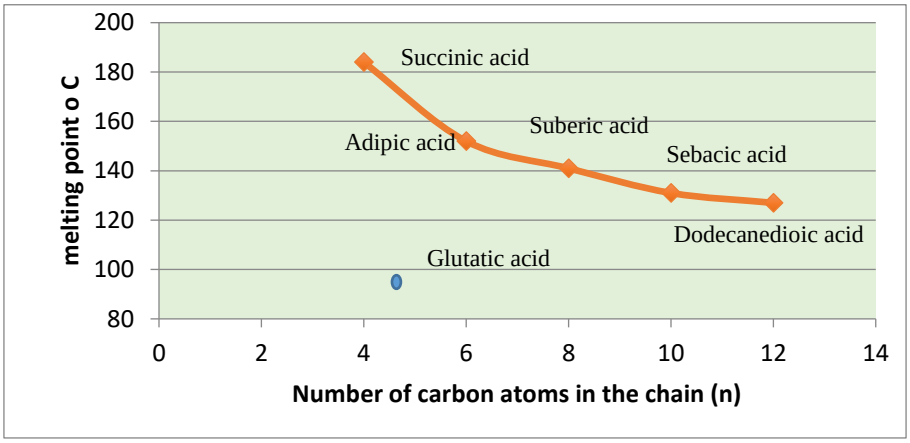

Figure 1-2 Correlation of the melting points with the dicarboxylic acid chain length

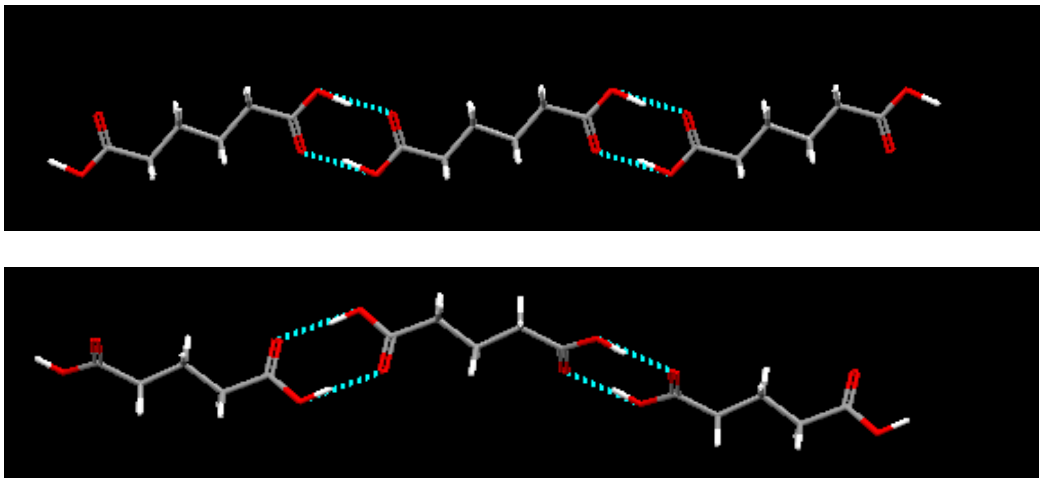

Figure 1-3 Difference of the spatial arrangement of the even chain (top) and odd chain (bottom) dicarboxylic acids[7]

This example highlights that the understanding of both molecular and intermolecular interactions are important in the design of novel materials with predictable properties. Therefore in parallel to the studies of the effect of molecular conformations in altering the structural properties, analysis of non-covalent interactions also has been developed as a separate research field, and has played a central role in the design of new materials with specific properties.[8]

1.2 Supramolecular chemistry: The chemistry of the non-covalent bond

Supramolecular chemistry is defined as the 'chemistry of molecular assemblies and of the intermolecular bond'.[9] The term was first introduced by one of its leading proponents Jean-Marie Lehn, who won the Nobel prize for his work in the area in 1987.[10] More generally supramolecular chemistry is 'chemistry beyond the molecule' in which it goes beyond the scope of using only covalent bonds to make and alter the properties of molecules. In an ideal supramolecular process, molecular building blocks are designed to express the specific intermolecular interactions to achieve controlled and directional assembly which in turn leads to a better understanding of the macroscopic properties of materials (Figure 1-4).

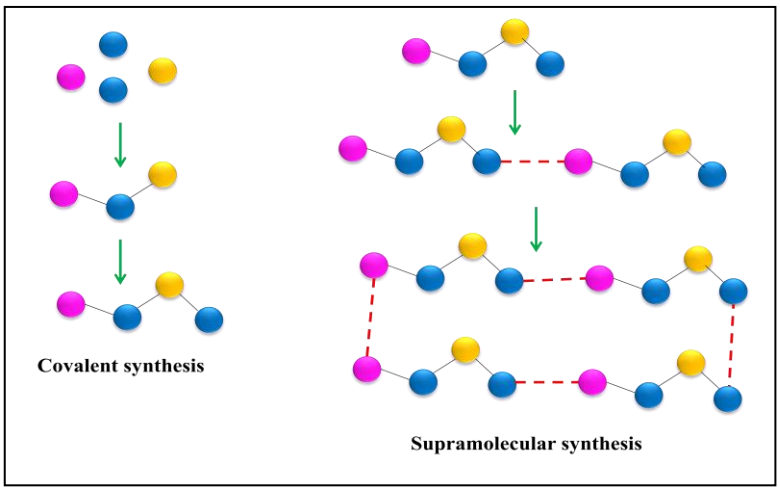

Figure 1-4 Difference between covalent synthesis and supramolecular synthesis

Supramolecular chemistry uses relatively weak non-covalent interactions like hydrogen bonds, halogen bonds, van der Waals forces and π-π interactions in molecular recognition and communication[8] (Table 1-1).

Table 1-1 Estimated strengths of molecular interactions[11, 12]

Type of interaction	Strength (kJ/mol)
Covalent	100-400
Hydrogen bond	10-65
π-π	0-50
Metal-ligand	0-400
Van der Waal	<5
Halogen bond	5-180

1.2.1 Crystal engineering: A direction of supramolecular chemistry

Crystals are the ultimate examples of supramolecular assemblies. Dunitz[13] describes a crystal as a supramolecular *par-excellence* in which millions of molecules are held together by non-covalent interactions in a periodic arrangement. A crystal engineer uses non-covalent interactions to design ordered supramolecular aggregates whereas a synthetic chemist aims to generate molecules through covalent bonds.[14] Solid state applications of crystal engineering were greatly influenced by the pioneering work done by Schmidt[15] who emphasized that the physical and chemical properties of crystals are highly dependent on the distribution of the molecular components within the crystal lattice. He correlated the idea of solid state reactivity through the analysis of 2+2 photodimerization reactions with favorable molecular spacing of the two components in the crystal lattice [15] (Figure 1-5).

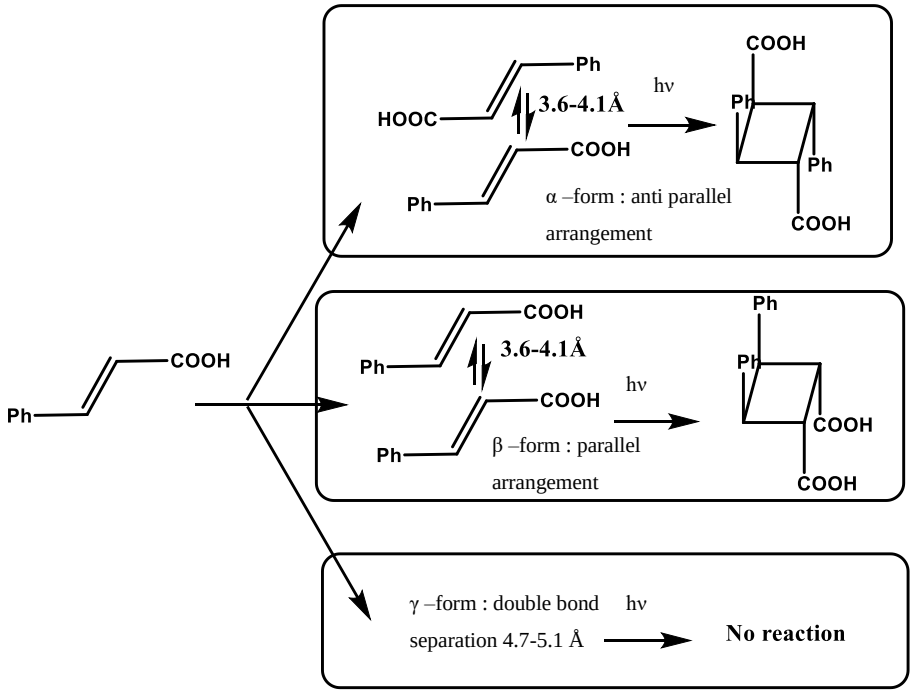

Figure 1-5 Alignment of molecules in a desired orientation to get a photodimerized product[15]

In another example, Desiraju and co-workers[16] showed the importance of the arrangement of stilbene based chromophores in a non-centrosymmetric fashion to obtain non-linear optical materials[17] (Figure 1-6).

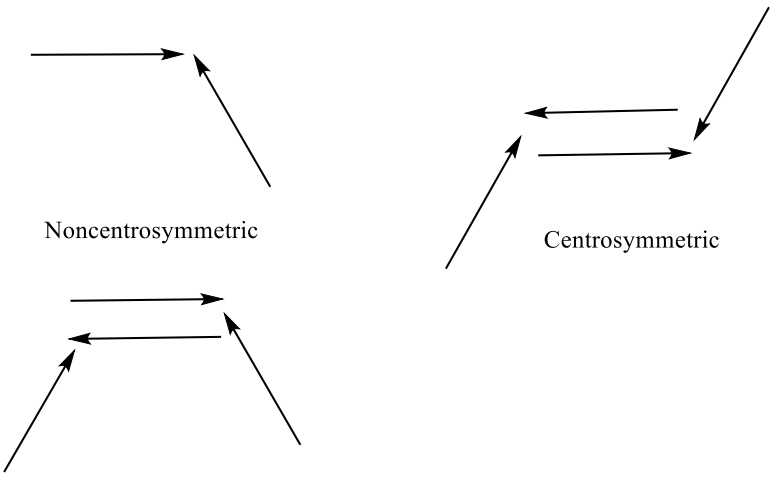

Figure 1-6 Primary arrangement of chromophores, noncentrosymmetic arrangement gives NLO materials and centrosymmetric arrangements gives non functional materials[17]

Therefore the term crystal engineering can be best defined as the "*understanding of intermolecular interactions in the context of crystal packing and the utilization of such understanding in the design of new solids with desired physical and chemical properties*"[18]

1.2.2 Supramolecular synthon

One of the challenging question in crystal engineering is, given a molecular structure compound what is the crystal structure?[19] Identification of structural units in a supramolecule which can be assembled logically opens a dream path for every crystal engineer.[20] Desiraju provided a simplification by introducing structural units called supramolecular synthons, which are the simplest robust units within the supermolecule which can be assembled by known or conceivable intermolecular interactions.[21] By dissecting a complex supramolecule into simpler structural units, defined by 'supramolecular retrosynthesis,[21,22] it helps to understand the molecular arrangement and the interchangeability of synthons in crystal arrangement (Figure1-7).

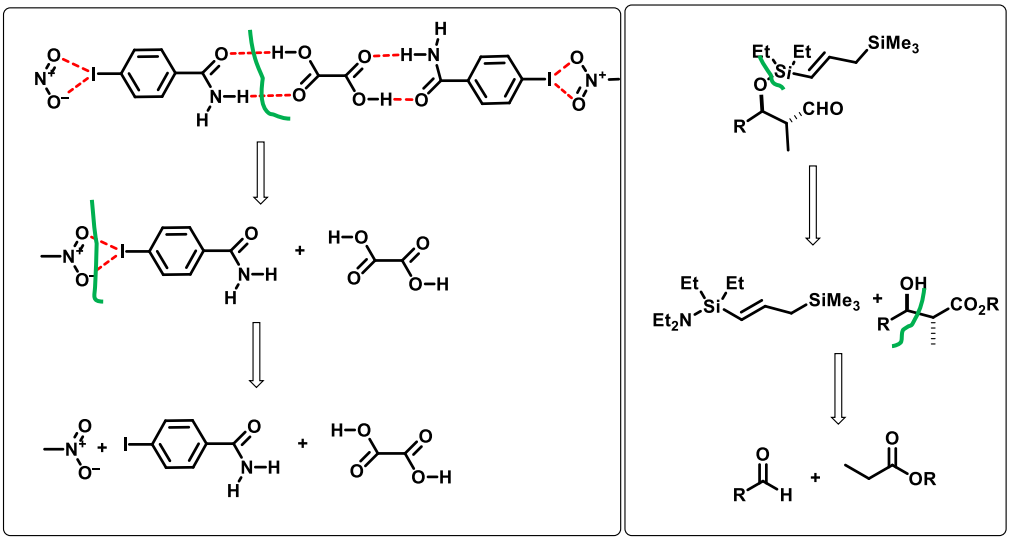

Figure 1-7 Schematic representation of a supramolecular retrosynthesis and covalent retrosynthesis

Supramolecular synthons carry the key information of the molecular recognition unit and since these units are common to many structures, they can be used to arrange molecules in a predictable manner.[23] Supramolecular synthons are mainly divided into two categories, homosynthons and heterosynthons (Figure 1-8). Figure 1-9 illustrates a few examples of robust supramolecular synthons which are commonly used in crystal engineering.[24]

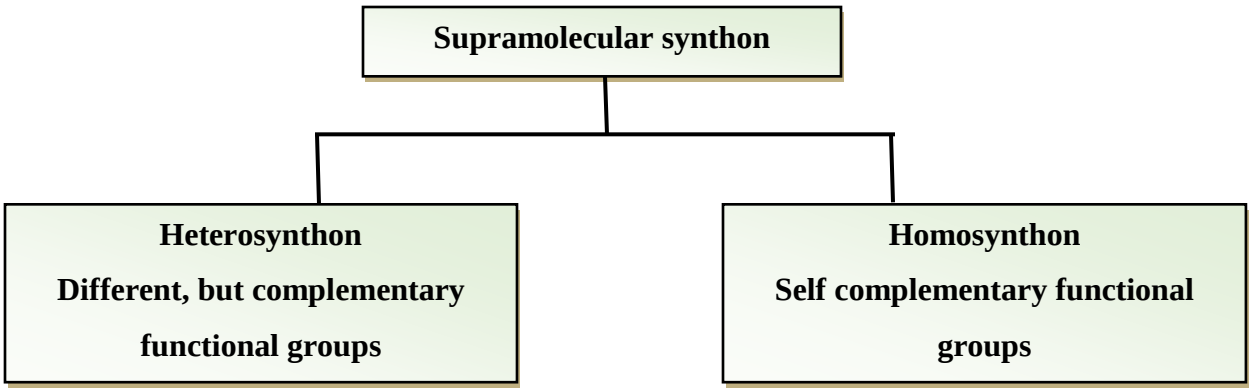

Figure 1-8 Two main categories of the supramolecular synthon

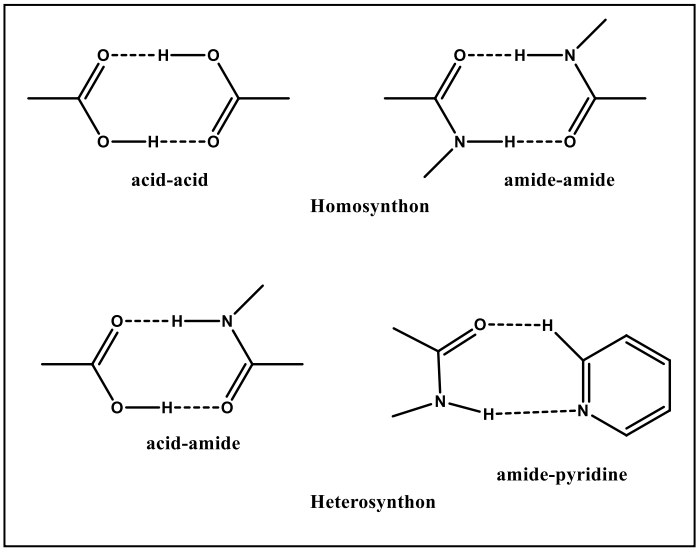

Figure 1-9 Examples of commonly used homo and hetero supramolecular synthons in crystal engineering[25]

1.3 Co-crystallization: A strategy to obtain multicomponent crystals

Co-crystals are multi component crystals designed through non-covalent interactions. They are defined as "solids that are crystalline materials, composed of two or more molecules in the same crystal lattice."[26] In co-crystallization molecules are brought together without making or breaking covalent bonds, in this process molecules can undergo either homomeric interactions (recrystallization) or heteromeric interactions (co-crystallization). Molecules prefer to undergo recrystallization over co-cystallization,[27] however selecting molecules with complementary intermolecular interactions favor the formation of the latter product (Figure 1-10).

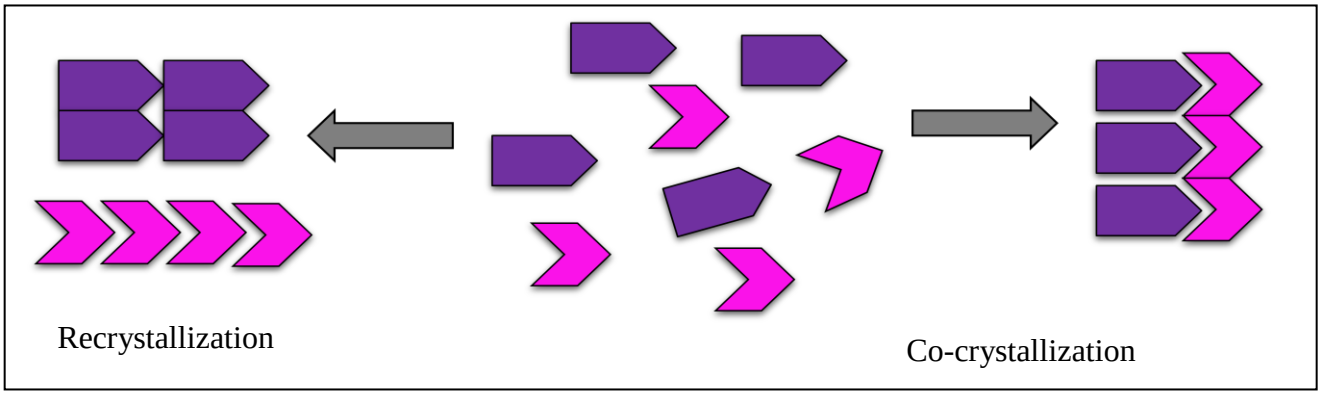

Figure 1-10 Schematic representation of co-crystallization and recrystalization

1.3.1 Non-covalent interactions: The glue in crystal engineering

In co-crystals, molecular components are brought together by several types of intermolecular interactions, namely, hydrogen bonds,[28] halogen bonds,[29] π-π interactions,[30] etc.[31] Recognizing the significance of intermolecular interactions on the formation of solid state structures has greatly influenced crystal engineering.[32] Therefore understanding the properties of intermolecular interactions allow for the design of molecules whose functional groups can interact non-covalently so that the molecules will pack in a predicted fashion[23] (Figure 1-11).

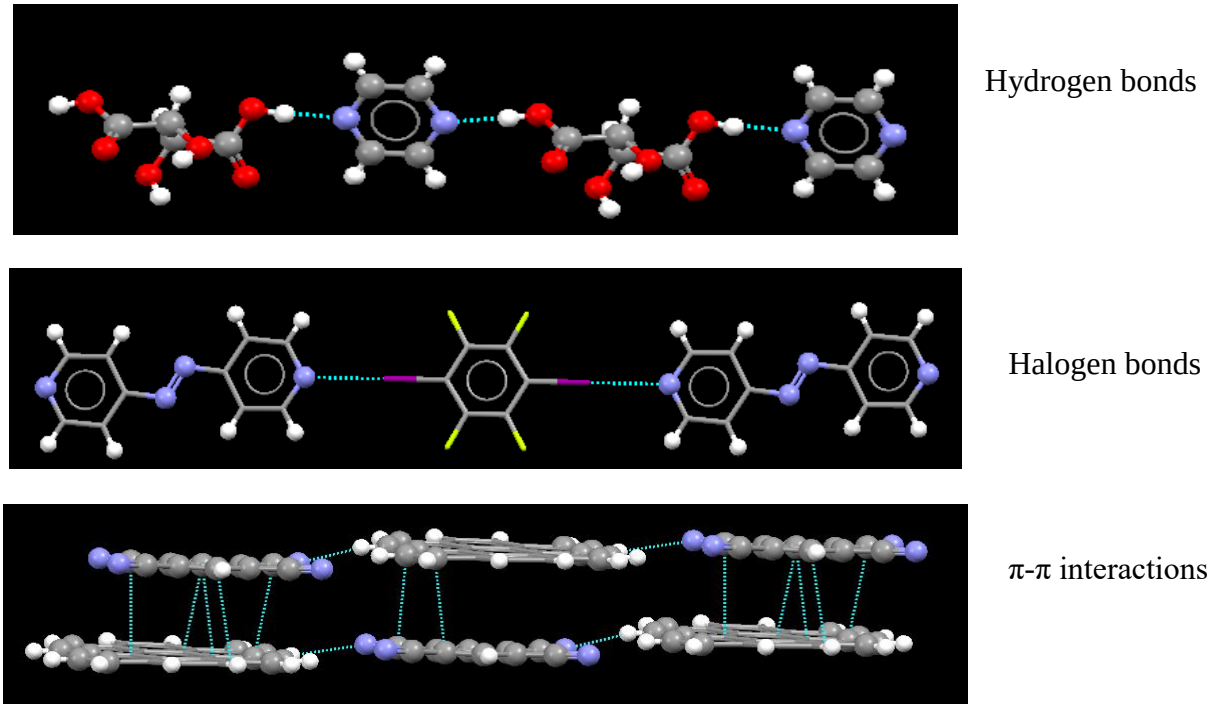

Figure 1-11 Co-crystals based on different of non-covalent interactions [33]

1.3.1.1 Hydrogen bond based co-crystals

The hydrogen bond is the most studied intermolecular interaction in supramolecular chemistry and crystal engineering. The strength and the directionality of the hydrogen bond has made it more advantageous in designing functionalized materials in solid state chemistry.[34] The IUPAC definition of a hydrogen bond is "an attractive interaction between a hydrogen atom from a molecule or a molecular fragment X–H in which X is more electronegative than H, and an atom or a group of atoms in the same or a different molecule, in which there is evidence of bond formation."[35] The field of crystal engineering and solid state chemistry is greatly indebted to the influencing work done by Etter and co-workers who started to focus on the control of hydrogen bonds in molecular crystallization. Through the analysis of the Cambridge Structural Database of neutral molecules with accessible hydrogen bonding functionalities, Etter and co-workers identified possible preferences of hydrogen bonds in terms of selectivity and pattern of molecular

aggregation.[36] Together with this observation, they proposed a set of guidelines for the selectivity of hydrogen bonding, which is known as Etter's rules.[36] The first three general rules are highlighted below,

1. All good proton donors and acceptors are used in hydrogen bonding

2. If a six membered intramolecular hydrogen bond can form, it will usually do so in preference to forming intermolecular hydrogen bonds

3. The best proton donors and acceptors remaining after intramolecular hydrogen-bond formation, form intermolecular hydrogen bonds to one another.

These guidelines have had a great influence on the development of crystal engineering especially the structures built from molecules specifically designed to incorporate multiple hydrogen bonding and oriented in arrays to obtain predictable architectures.[20]

1.3.1.2 Halogen- bond based co-crystals

Halogen bond is another non-covalent interaction which has been added into the supramolecular tool box recently.[37] They are similar to their more widespread counterpart hydrogen bonds.[38] Based on the IUPAC recommendations, *"a halogen bond occurs when there is evidence of a net attractive interaction between an electrophilic region associated with a halogen atom in a molecular entity and a nucleophilic region in another, or the same, molecular entity"*.[39] Figure 1-12 illustrates the formation of a halogen bond with different nucleophilic species.

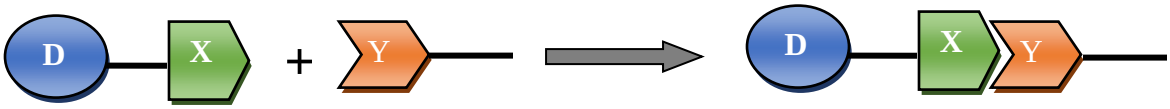

D- C, N, halogen etc.

X- Cl, Br, I

Y- N, O, S, Cl, Br, I, Cl^-, Br^-,I^-

Figure 1-12 Schematic diagram showing the formation of a halogen bond with different nucleophiles

A covalently bound halogen atom has an anisotropic distribution of electron charge, which results in excess negative charge perpendicular to the C-X bond and a depletion of negative charge along the C-X bond leading to a positive charge at the tip of the halogen atom, which is referred as the 'σ' hole.[40] Therefore a covalently bound halogen atom has a capacity to interact with both nucleophilic and electrophilic species (Figure 1-13).

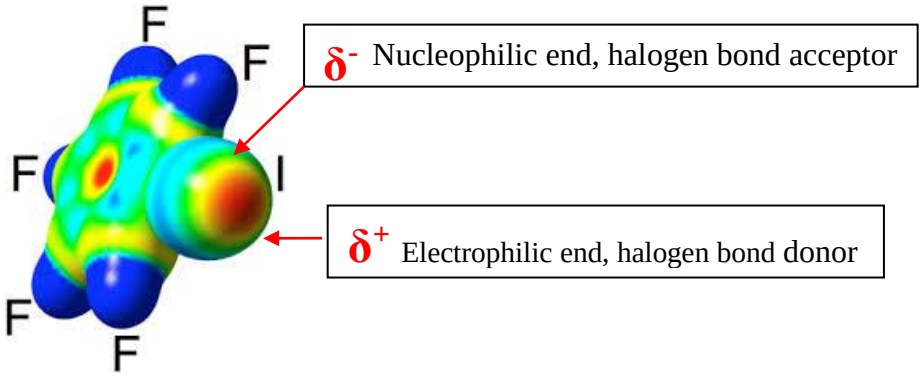

Figure 1-13 Anisotropic distribution of positive and negative charges around the halogen atom of iodopentafluorobenzene

Following the pioneering work of Metrangolo and Resinati, it is become evident that halogen bonds can be used to fine tune the structural outcomes of the self-assembly [37, 41] and

Figure 1-14 shows the use of halogen bonds in the assembly of a linear supramolecular arrangement.[42]

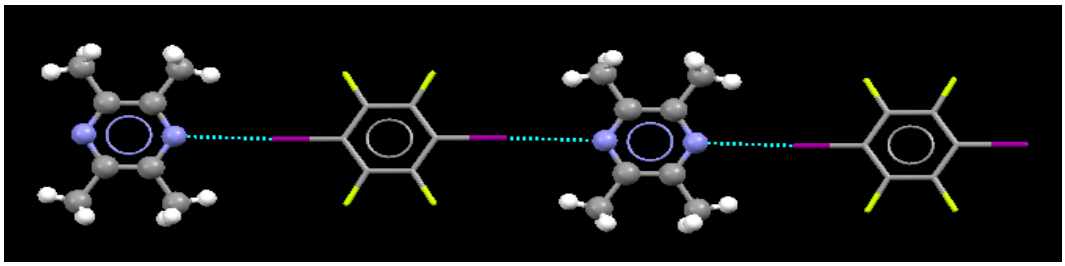

Figure 1-14 Designing supramolecular linear arrangements using halogen bonds[42]

1.3.2 Applications of hydrogen and halogen-bond based systems

Co-crystal technology has been widely used for altering physical properties of pharmaceuticals,[6, 43, 44] agrochemicals,[45]energetic materials,[46, 47, 48] organic semiconductors,[49] non-linear optics,[50] ferroelectric materials[51] and charge transfer complexes.[52] Furthermore co-crystallization has been applied in chiral resolution,[53] separation and purification processes[54] and solvent free synthesis processes.[55]

1.3.2.1 Pharmaceuticals

Pharmaceutical co-crystals have gained widespread attention in the pharmaceutical industry with the aim of modifying physiochemical properties of active pharmaceutical ingredients (API).[56] Changing the solid form of an API can alter physical properties like solubility, thermal stability and bioavailability.[43, 57] For example, co-crystals of even chain dicarboxylic acids with an anticancer agent hexamethylenebisacetamide showed increase of solubility with the use of succinic, adipic and suberic acids as co-formers (Figure 1-15).[58] In another example, 2-[4-(4-chloro-2-fluorophenoxy)phenyl]pyrimidine-4-carboxamide (used in preventing surgical, chronic and neuropathic pain and has extremely low solubility

characteristics) and glutaric acid co-crystal shows an increased *in vitro* rate of delivery of API into the aqueous environment of the dissolution media.[59]

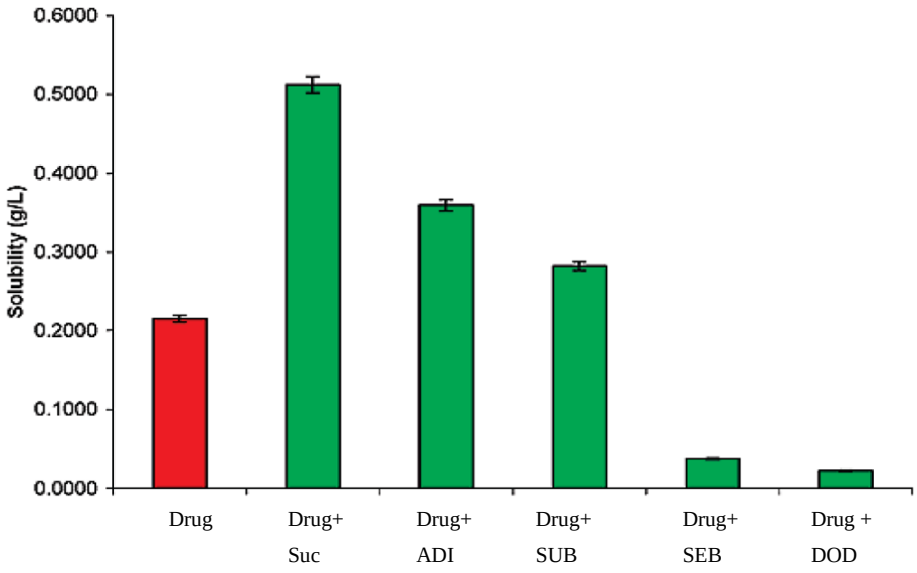

Figure 1-15 Changes of solubility of drug molecule with increase of the hydrophobicity of di acids[58]

1.3.2.2 Agrochemicals

In the agrochemical industry, there is a need to design agrochemical active ingredients to meet the requirements of the 21st century. Co-crystallization has successfully assisted in achieving this goal through improved physical properties such as decreased solubility, improved melting points, and storage and formulation stability.[60] Successful fine tuning of solubility of an agrochemical active cyprodinil, through co-crystallization is illustrated in Figure 1-16.[12]

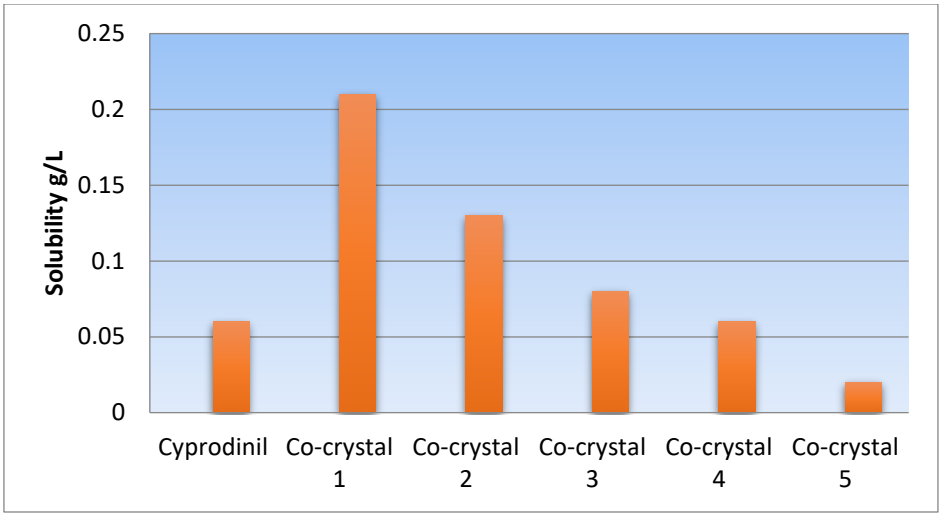

Figure 1-16 Solubility profile of cyprodinil co-crystals[12]

1.3.2.3 Energetics

Another successful application of co-crystallization can be found in the field of designing energetic materials. Even though this is still an emerging area, there are successful examples of using co-crystals to alter properties like impact and friction sensitivity and thermal stability of energetic materials.[46, 61] One such example was reported by Matzger and co-workers, where a co-crystal of two energetic materials, CL-20 and TNT was synthesized as a novel high-power, low-sensitivity explosive.[48]

1.3.2.4 Organocatalysis

Hydrogen bond based catalytic systems are widely applied in organocatalysis.[62] Specially the involvement of thiourea based catalysts has shown many advantages in supramolecular chemistry.[63] Similar to hydrogen bond based organocatalysts, halogen bond based organocatalysts are also effective in catalytic systems, through activation of an electrophile towards a nucleophilic attack owing to the directionality and selectivity of halogen bonds.[64] In

one such example, iodine trichloride act as a halogen bond donor in catalyzing ring opening polymerization reaction of L-lactide by activating the carbonyl group[65] (Figure 1-17).

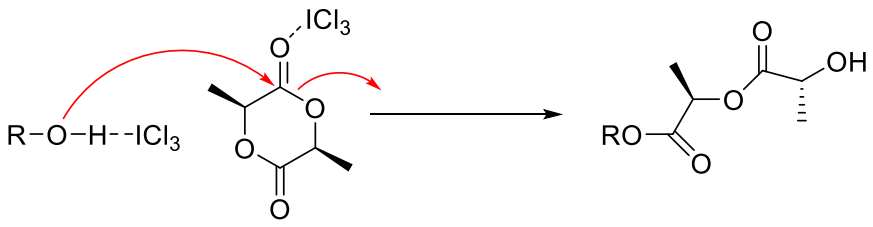

Figure 1-17 Halogen bond catalyzed ring opening polymerization of l-lactide[65]

1.4 Goals of the study

An improved knowledge of intermolecular interactions is crucial in designing new solid forms with pre-determined connectivities. Controlled synthesis of supramolecular assemblies will lead to supramolecular networks with high prediction and hence control of the final structure-property relationships.

The goals of this thesis are as follows,

1. Finding the impact of electrostatic potential values in landscaping the structural outcomes in hydrogen and halogen bond based interactions in the solid state and implementing an electrostatic view for co-crystal synthesis. (Chapter 2)

2. Designing new organocatalysts based on halogen bond donors. In this study concepts used in well-known hydrogen bond based organocatalysis will be extracted to design halogen based organo- catalytic systems. (Chapter 3)

3. Exploring the effect of structural mimics in landscaping the structural outcomes of poorly soluble molecules. In this study, a poorly soluble API and a synthesized mimic is analyzed in terms of the structural behavior in the presence of FDA approved even-chain dicarboxylic acids (Chapter 4)

4. Application of co-crystallization technology to corrosive energetic materials to reduce chemical reactivity. In this study effect of nitrogen and oxygen based acceptors in modulating the performance and sensitivity of the energetic materials has studied. (Chapter 5)

5. Decreasing the hygroscopicity of energetic materials through successful replacement of water molecules with suitable co-formers. Interaction of acidic N-H protons of the energetic material will be analyzed through different nitrogen and oxygen based acceptor molecules. (Chapter 6)

1.5 References

1. P. G. Seybold, M. May and U. A. Bagal, *J. Chem. Educ.*, 1987, **64**, 575.
2. H. Weiner, *J. Chem.Phys.*, 1947, **15**, 766.
3. H. Wiener, *J. Phys. Chem.*, 1948, **52**, 425;. H. weiner, *J.Am.Chem.Soc*, 1947, **15**, 766.
4. M. She, Z. Yang, L. Hao, Z. Wang, T. Luo, M. Obst, P. Liu, Y. Shen, S. Zhang and J. Li, 2016, **6**, 28972; A. Sosnowska, M. Barycki, A. Gajewicz, M. Bobrowski, S. Freza, P. Skurski, S. Uhl, E. Laux, T. Journot, L. Jeandupeux, H. Keppner and T. Puzyn, *ChemPhysChem*, 2016, **17**, 1591-1600; G. E. Wnek, *J. Chem. Educ.*, 2017.
5. J. Bernstein, *J. Phys. D: Appl. Phys.*, 1993, **26**, B66.
6. C. B. Aakeröy, S. Forbes and J. Desper, *CrystEngComm*, 2014, **16**, 5870-5877.
7. R. Srinivasa Gopalan, P. Kumaradhas, G. U. Kulkarni and C. N. R. Rao, *J. Mol. Struct.*, 2000, **521**, 97-106.
8. A. S. Mahadevi and G. N. Sastry, *Chem. Rev.*, 2016, **116**, 2775-2825.
9. J.-M. Lehn, *Angew. Chem. Int. Ed.*, 1988, **27**, 89-112.
10. J. W. Steed, J. L. Atwood, *Supramolecular chemistry*, John Wiley & Sons, Ltd, 2000.

11. A. Gavezzotti, *New J. Chem.*, 2016, **40**, 6848-6853; G. A. D. Alberto Otero de la Roza, *Non-covalent Interactions in Quantum Chemistry and Physics: Theory and physics : Theory and applications*, Elsevier, 2011.
12. S. Panikkattu, Designing molecular solids with structural control and tunable physical properties using co-crystallization techniques, Kansas State University, 2013.
13. J. D. Dunitz, in *Implications of Molecular and Materials Structure for New Technologies*, eds. J. A. K. Howard, F. H. Allen and G. P. Shields, Springer Netherlands, Dordrecht, 1999, **12**, 175-184.
14. E. R. T. Tiekink, *Supramolecular Chemistry: From Molecules to Nanomaterial*, 2012.
15. G. M. J. Schmidt, *Pure Appl. Chem.*, 1971, **27**, 647-678.
16. G. R. Desiraju, *Cryst. Growth Des.*, 2011, **11**, 896-898.
17. M. Muthuraman, R. Masse, J.-F. Nicoud and G. R. Desiraju, *Chem. Mater.*, 2001, **13**, 1473-1479.
18. G. R. Desiraju, *Crystal Engineering: The Design of Organic Solids* ,Elsevier, Amsterdam, 1989.
19. D. S. Reddy, D. C. Craig and G. R. Desiraju, *J. Am. Chem. Soc.*, 1996, **118**, 4090-4093.
20. O. V. Shishkin, R. I. Zubatyuk, S. V. Shishkina, V. V. Dyakonenko and V. V. Medviediev, *PCCP*, 2014, **16**, 6773-6786.
21. G. R. Desiraju, *Angew. Chem.Int. Ed.*, 1995, **34**, 2311-2327.
22. V. R. Thalladi, B. S. Goud, V. J. Hoy, F. H. Allen, J. A. K. Howard and G. R. Desiraju, *Chem. Commun.*, 1996, 401-402.
23. G. R. Desiraju, *J. Am. Chem. Soc.*, 2013, **135**, 9952-9967.
24. C. V. K. S. a. R. D. Rogers, *Mater. Today*, 1998.

25. J. K. Savjani, *Asian J. Pharm.*, 2015, **9**, 147-151.

26. S. Aitipamula, R. Banerjee, A. K. Bansal, K. Biradha, M. L. Cheney, A. R. Choudhury, G. R. Desiraju, A. G. Dikundwar, R. Dubey, N. Duggirala, P. P. Ghogale, S. Ghosh, P. K. Goswami, N. R. Goud, R. R. K. R. Jetti, P. Karpinski, P. Kaushik, D. Kumar, V. Kumar, B. Moulton, A. Mukherjee, G. Mukherjee, A. S. Myerson, V. Puri, A. Ramanan, T. Rajamannar, C. M. Reddy, N. Rodriguez-Hornedo, R. D. Rogers, T. N. G. Row, P. Sanphui, N. Shan, G. Shete, A. Singh, C. C. Sun, J. A. Swift, R. Thaimattam, T. S. Thakur, R. Kumar Thaper, S. P. Thomas, S. Tothadi, V. R. Vangala, N. Variankaval, P. Vishweshwar, D. R. Weyna and M. J. Zaworotko, *Cryst Growth Des.*, 2012, **12**, 2147-2152.

27. C. B. Aakeröy and D. J. Salmon, *CrystEngComm*, 2005, **7**, 439-448.

28. B. I. Harriss, L. Vella-Zarb, C. Wilson and I. R. Evans, *Cryst Growth Des.*, 2014, **14**, 783-791; B. Sarma and B. Saikia, *CrystEngComm*, 2014, **16**, 4753-4765.

29. M. Baldrighi, G. Cavallo, M. R. Chierotti, R. Gobetto, P. Metrangolo, T. Pilati, G. Resnati and G. Terraneo, *Mol. Pharm.*, 2013, **10**, 1760-1772; Q.-N. Zheng, X.-H. Liu, T. Chen, H.-J. Yan, T. Cook, D. Wang, P. J. Stang and L.-J. Wan, *J. Am. Chem. Soc.*, 2015, **137**, 6128-6131.

30. J. Zhang, L. A. Mitchell, D. A. Parrish and J. M. Shreeve, *J. Am. Chem. Soc.*, 2015, **137**, 10532-10535.

31. S. K. Dey, R. Saha, S. Biswas, A. Layek, S. Middya, I. M. Steele, M. Fleck, P. P. Ray and S. Kumar, *Cryst Growth Des.*, 2014, **14**, 207-221.

32. N. R. Chamness, Christer B. Aakeröy, and C. Janiak, *CrystEngComm,* 2010, **12**, 22-43.

33. P. Ravat, S. SeethaLekshmi, S. N. Biswas, P. Nandy and S. Varughese, *Cryst Growth Des.*, 2015, **15**, 2389-2401; D. Braga, F. Grepioni and G. I. Lampronti, *CrystEngComm*, 2011, **13**, 3122-3124; S. V. Rosokha, J. Lu, B. Han and J. K. Kochi, *New J. Chem.*, 2009, **33**, 545-553.

34. F. G. Dario Braga, A. Guy Orpen, *Crystal engineering: From molecules to crystals to materials*, Springer, 1999.

35. E. Arunan, R. Desiraju Gautam, A. Klein Roger, J. Sadlej, S. Scheiner, I. Alkorta, C. Clary David, H. Crabtree Robert, J. Dannenberg Joseph, P. Hobza, G. Kjaergaard Henrik, C. Legon Anthony, B. Mennucci and J. Nesbitt David, *Definition of the hydrogen bond-IUPAC recommendations*, 2011, **83**, 1637.

36. M. C. Etter, *Acc. Chem. Res.*, 1990, **23**, 120-126.

37. G. Cavallo, P. Metrangolo, R. Milani, T. Pilati, A. Priimagi, G. Resnati and G. Terraneo, *Chem. Rev.*, 2016, **116**, 2478-2601.

38. K. Riley and K.-A. Tran, *Faraday Discuss.*, 2017.

39. R. Desiraju Gautam, P. S. Ho, L. Kloo, C. Legon Anthony, R. Marquardt, P. Metrangolo, P. Politzer, G. Resnati and K. Rissanen, *Pure.Appl.Chem*, 2013, **85**, 1711.

40. T. Brinck, J. S. Murray and P. Politzer, *Int. J. Quantum Chem*, 1992, **44**, 57-64; P. Politzer and J. S. Murray, *ChemPhysChem*, 2013, **14**, 278-294; P. Politzer, J. S. Murray and T. Clark, *Phys. Chem. Chem. Phys.*, 2010, **12**, 7748-7757.

41. P. Metrangolo, F. Meyer, T. Pilati, G. Resnati and G. Terraneo, *Angew. Chem. Int. Ed.*, 2008, **47**, 6114-6127; P. Metrangolo, H. Neukirch, T. Pilati and G. Resnati, *Acc. Chem. Res.*, 2005, **38**, 386-395.

42. J.-L. Syssa-Magale, K. Boubekeur, P. Palvadeau, A. Meerschaut and B. Schollhorn, *CrystEngComm*, 2005, **7**, 302-308.

43. P. Khadka, J. Ro, H. Kim, I. Kim, J. T. Kim, H. Kim, J. M. Cho, G. Yun and J. Lee, *Asian J. Pharm.l Sci.*, 2014, **9**, 304-316.

44. A. V. Yadav, A. S. Shete, A. P. Dabke, P. V. Kulkarni and S. S. Sakhare, *Indian J. Pharm. Sci.*, 2009, **71**, 359-370.

45. E. Nauha and M. Nissinen, *J. Mol. Struct.*, 2011, **1006**, 566-569.

46. C. B. Aakeröy, T. K. Wijethunga and J. Desper, *Chem. Eur. J.*, 2015, **21**, 11029-11037; H. J. Lloyd, S. Corless and C. R. Pulham, *Acta Crystallogr. Sect. A*, 2013, **69**, s515-s516.

47. S. R. Anderson, D. J. am Ende, J. S. Salan and P. Samuels, *Propellants, Explos. Pyrotech.*, 2014, **39**, 637-640.

48. O. Bolton and A. J. Matzger, *Angew. Chem. Int. Ed.*, 2011, **50**, 8960-8963.

49. H. T. Black and D. F. Perepichka, *Angew. Chem. Int. Ed.*, 2014, **53**, 2138-2142.

50. E. D. D'silva, G. K. Podagatlapalli, S. V. Rao, D. N. Rao and S. M. Dharmaprakash, *Crystal Growth & Design*, 2011, **11**, 5362-5369; P. Baskaran, M. Vimalan, P. Anandan, G. Bakiyaraj, K. Kirubavathi and K. Selvaraju, *Journal of Taibah University for Science*, 2017, **11**, 11-17; C. Bosshard, F. Pan, M. S. Wong, S. Manetta, R. Spreiter, C. Cai, P. Günter and V. Gramlich, *Chem. Phys.*, 1999, **245**, 377-394.

51. G. Bolla, H. Dong, Y. Zhen, Z. Wang and W. Hu, *Sci. China Mater.*, 2016, **59**, 523-530; S. Horiuchi, F. Ishii, R. Kumai, Y. Okimoto, H. Tachibana, N. Nagaosa and Y. Tokura, *Nat Mater*, 2008, **7**, 922-922.

52. T. Salzillo, M. Masino, G. Kociok-Köhn, D. Di Nuzzo, E. Venuti, R. G. Della Valle, D. Vanossi, C. Fontanesi, A. Girlando, A. Brillante and E. Da Como, *Cryst Growth Des.*,

2016, **16**, 3028-3036; W. Zhu, R. Zheng, X. Fu, H. Fu, Q. Shi, Y. Zhen, H. Dong and W. Hu, *Angew. Chem. Int. Ed.*, 2015, **54**, 6785-6789.

53. G. Springuel and T. Leyssens, *Cryst Growth Des.*, 2012, **12**, 3374-3378.

54. C. Matheys, N. Tumanova, T. Leyssens and A. S. Myerson, *Cryst.Growth Des.*, 2016, **16**, 5549-5553.

55. E. Stoler and J. Warner, *Molecules*, 2015, **20**, 14833.

56. N. K. Duggirala, M. L. Perry, O. Almarsson and M. J. Zaworotko, *Chem. Commun.*, 2016, **52**, 640-655.

57. D. D. Gadade and S. S. Pekamwar, *Adv. Pharm. Bull.*, 2016, **6**, 479-494; D. J. Good and N. Rodríguez-Hornedo, *Cryst Growth Des.*, 2009, **9**, 2252-2264; A. K. Nair, O. Anand, N. Chun, D. P. Conner, M. U. Mehta, D. T. Nhu, J. E. Polli, L. X. Yu and B. M. Davit, *AAPS J.*, 2012, **14**, 664-666.

58. S. Forbes, J. Desper, and C.B. Aakeröy, *J. Am. Chem. Soc.*, 2009, **131**, 17048-17049.

59. D. P. McNamara, S. L. Childs, J. Giordano, A. Iarriccio, J. Cassidy, M. S. Shet, R. Mannion, E. O'Donnell and A. Park, *Pharm. Res.*, 2006, **23**, 1888-1897.

60. K. A. Powell, D. M. Croker, C. D. Rielly and Z. K. Nagy, *Chem. Eng. Sci.*, 2016, **152**, 95-108; E. Nauha, 2012.

61. V. D. G. A. Sudheer Kumar, S. Subrahmanyam,and Akhila K. Sahoo, *Chem. Eur. J.* , 2013, **19**, 509 – 518.

62. H. Pellissier, *Tetrahedron*, 2007, **63**, 9267-9331; I. R. Shaikh, *J. Catal.*, 2014, **2014**, 35.

63. A. P. Dove, R. C. Pratt, B. G. G. Lohmeijer, R. M. Waymouth and J. L. Hedrick, *J. Am. Chem. Soc.*, 2005, **127**, 13798-13799.

64. F. Kniep, S. H. Jungbauer, Q. Zhang, S. M. Walter, S. Schindler, I. Schnapperelle, E. Herdtweck and S. M. Huber, *Angew. Chem. Int. Ed.*, 2013, **52**, 7028-7032; T. M. Beale, M. G. Chudzinski, M. G. Sarwar and M. S. Taylor, *Chem. Soc. Rev.*, 2013, **42**, 1667-1680; S. H. Jungbauer and S. M. Huber, *J. Am. Chem. Soc.*, 2015, **137**, 12110-12120.

65. G. R. Pierangelo Metrangolo, *Halogen Bonding II: Impact on Materials Chemistry and Life Sciences*, 2015.

Chapter 2 - Impact of electrostatic potential calculations on predicting structural patterns in hydrogen and halogen bonding

2.1 Introduction

2.1.1 Importance of structural predictions

Developing new solid state structures with advanced physical and chemical properties is of great interest in crystal engineering.[1] To understand the potential of crystalline materials it is important to correlate molecular structure with crystalline structure and macroscopic properties.[2] Predicting the crystal packing of a molecule is not asy,[3] as there can be many possible arrangements, therefore it would be advantageous to design strategies to simplify structural predictions in crystal engineering. Crystal engineering is driven by non-covalent interactions like hydrogen[4] and halogen bonding. These are widely studied and frequently used as synthetic vectors in molecular recognition events.[5] Thus having precise control over hydrogen- bond formation can provide robust synthetic strategies for designing supramolecular architectures. In 1990, Margaret Etter proposed that "the best proton donors and acceptors remaining after intermolecular hydrogen- bond formation form bonds to one another"[6,7] and this concept was illustrated by using an example of 2-aminopyrimidine-carboxylic acid co-crystals in which the ring nitrogen acceptors (better acceptor than acid carbonyl) form interactions with the acid O-H (better donor than amino group hydrogens), and the second best donor (N-H protons) and acceptor (carbonyl oxygen) forms hydrogen- bond interactions, respectively (Figure 2-1). Etters' work has been very important to current efforts for controlling and predicting the hydrogen-bond based structures and composition in molecular crystals.[6]

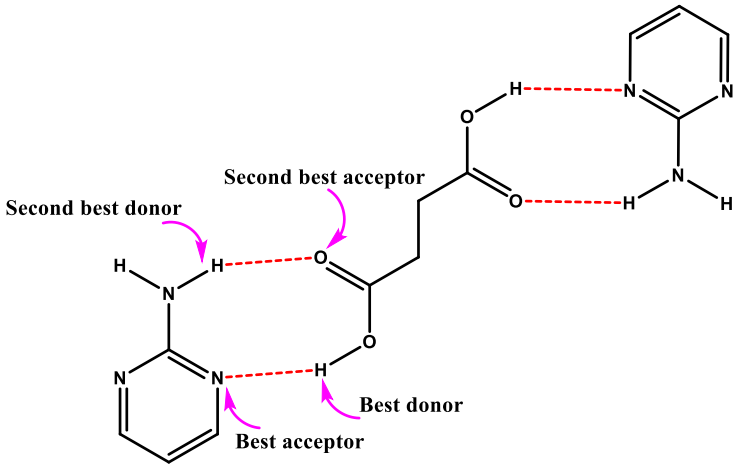

Figure 2-1 Aminopyrimidine-carboxylic acid co-crystal system governed by Etter's best donor/acceptor concept[6]

2.1.2 Electrostatic potential approach

Recently Hunter used calculated molecular electrostatic potential (MEP) values for rationalizing hydrogen bond preference. This method relies on the assumption that the long-range effect of electrostatic interactions play a key role in initial stages of molecular recognition compared to other forces like repulsion, induction and dispersion[8]. The maximum positive electrostatic potential value on the molecule is usually located close to an acidic hydrogen atom, and the most negative value is located over a lone pair or an area of π-electron density. The governing electrostatic interaction between two molecules is a pair- wise interaction which occurs between the minima and maxima of atoms.[8] Therefore calculated electrostatic potential values (MEPs) on acceptors and donors can be employed as an effective method for estimating hydrogen- bond capability over a series of functionalities.[9, 10]

Halogen bonds are also found in many supramolecular architectures which has led to the synthesis of many discrete and polymeric crystal arrangements.[11] Being able to predict structural outcomes in halogen bond based molecular systems would be highly significant in crystal

engineering. Similar to hydrogen bonds, halogen bonds are also considered primarily electrostatic in nature.[12] Murray and Politzer have shown that the electrostatic potential values computed on the halogens' surfaces, along the σ-hole of the halogen atom, can be related to the strength of halogen bonds in RX halides[13] (Figure 2-2).

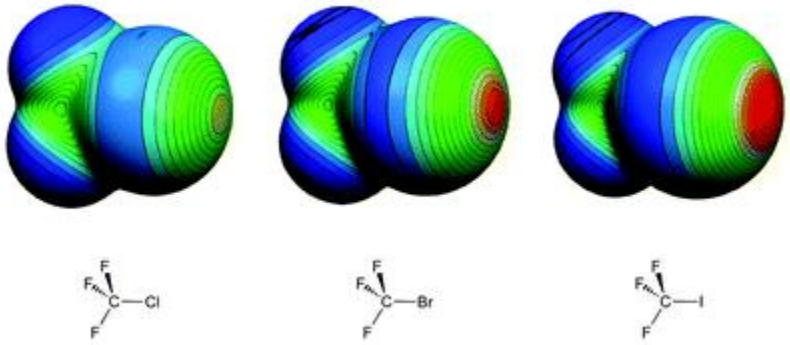

Figure 2-2 Changes of the strength of the σ hole with respect to the halide group[14]

Also, Taylor and co-workers showed that systematic changes of the electronic properties of halogen-bond donors can affect the halogen-bond interactions in a molecular system.[15] Therefore it is reasonable to assume that the electrostatic component of halogen bonding makes supramolecular interactions amenable to similar MEP based rankings and binding preferences. Several effects have been made to find the robustness of calculated MEPs for predicting structural outcomes in halogen and hydrogen bond based supramolecular systems.[9, 16, 17, 18] In these approaches, multi-component acceptor and donor groups were selected and the acceptor atoms with the highest negative electrostatic potential value was considered as the best acceptor and the donor atoms (halogen or hydrogen) with the highest positive MEP value was considered as the best donor group. Dominant intermolecular interactions were expected to occur between the best donor and the best acceptor groups. Figure 2-3 shows the application of calculated MEPs in predicting the structural outcome in a muticomponent donor system.[9] In this study, the best

donor group (hydroxyl moiety) forms an interaction with the best acceptor and the second best donor (carboxylic acid moiety) forms an interaction with the second best acceptor. Figure 2-4 shows structural predictions in a system with multiple acceptors. In this system, the best acceptor group (with highest negative MEP value) forms a halogen-bond interaction leaving the second best acceptor site intact.[18] In both examples it illustrates the best donor is determined by the highest positive electrostatic potential value and the best acceptor is determined by the highest negative electrostatic potential value.

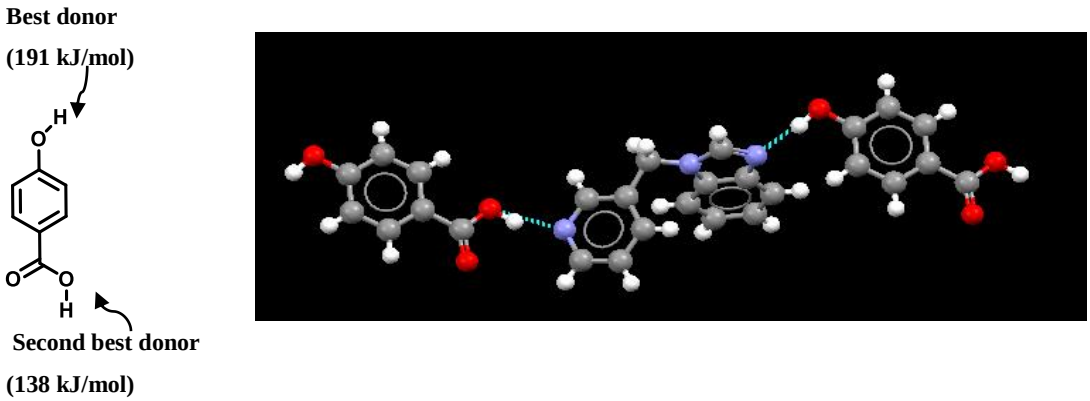

Figure 2-3 Best donor/acceptor interaction in a system with multiple donors[16]

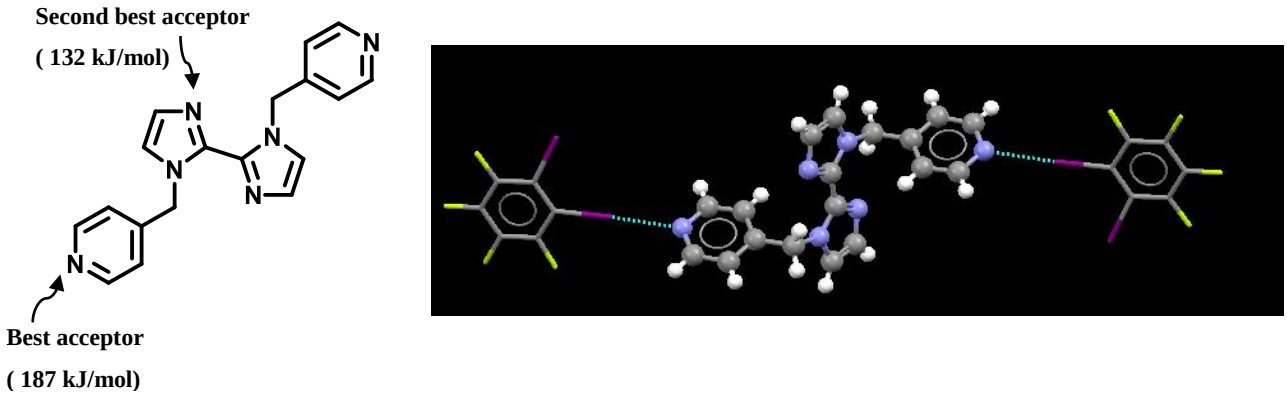

Figure 2-4 Best donor/acceptor interaction in a system with multiple acceptors[18]

2.1.3 Goal

Even though calculated MEPs values can be used for ranking acceptors and donors we do not know much about the details and limitations for using calculated MEPs of acceptors and donors before providing a label as a best donor or acceptor for intermolecular interactions. Previous attempts found that when the difference of calculated MEPs value between two acceptor sites is greater than 60 kJ/mol, the site with the highest negative potential has a higher tendency form a hydrogen or halogen bond interaction and is the best acceptor. But a difference of less than 30 kJ/mol was too small to be selective; both acceptors had equal chances to form interactions (Figure 2-5). In this study, we decided to find a boundary for MEPs values in ranking acceptor sites in multi component systems. With this in mind, two acceptor molecules **A1** and **A2** were synthesized (Figure 2-6). **A1** had a MEPs difference of 38 kJ/mol and **A2** had a difference of 26 kJ/mol between the competing acceptor sites. Since both **A1** and **A2** have nitrogen atoms as potential acceptors, hydrogen and halogen bond based donors were selected to examine the intermolecular interactions (Figure 2.7). In this study, we mainly focused on the nature of the calculated electrostatic potential values on acceptor atoms, thus the electrostatic nature of the donor molecules was not considered.

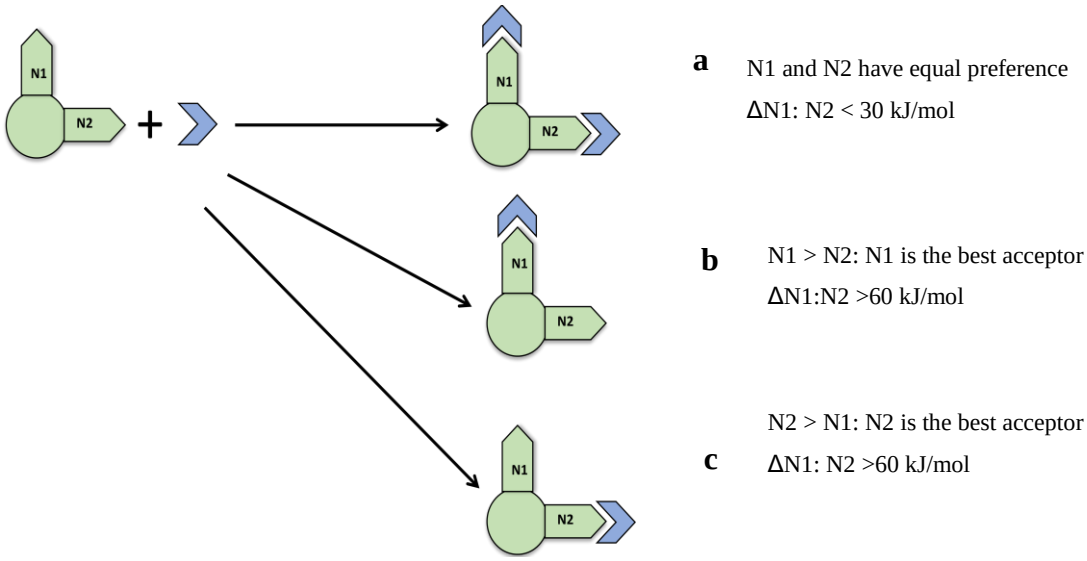

Figure 2-5 Possible structural outcomes of two acceptors (N1 and N2) in the presence of a donor molecule

With this study, we are expecting to answer the following questions;

1) Are these differences in MEPs large enough to obtain selectivity in forming intermolecular interactions?
2) With these differences can we label one site as a best acceptor site over the other acceptor site?
3) Can we obtain precise control in crystal arrangements with calculated MEP values in the presence of different donor molecules (Figure 2-7)

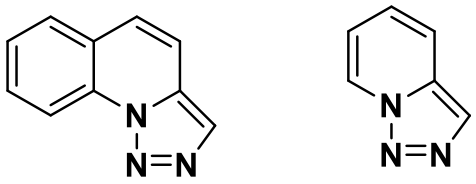

A1 **A2**

Figure 2-6 Acceptor molecules, A1 and A2 used in this study

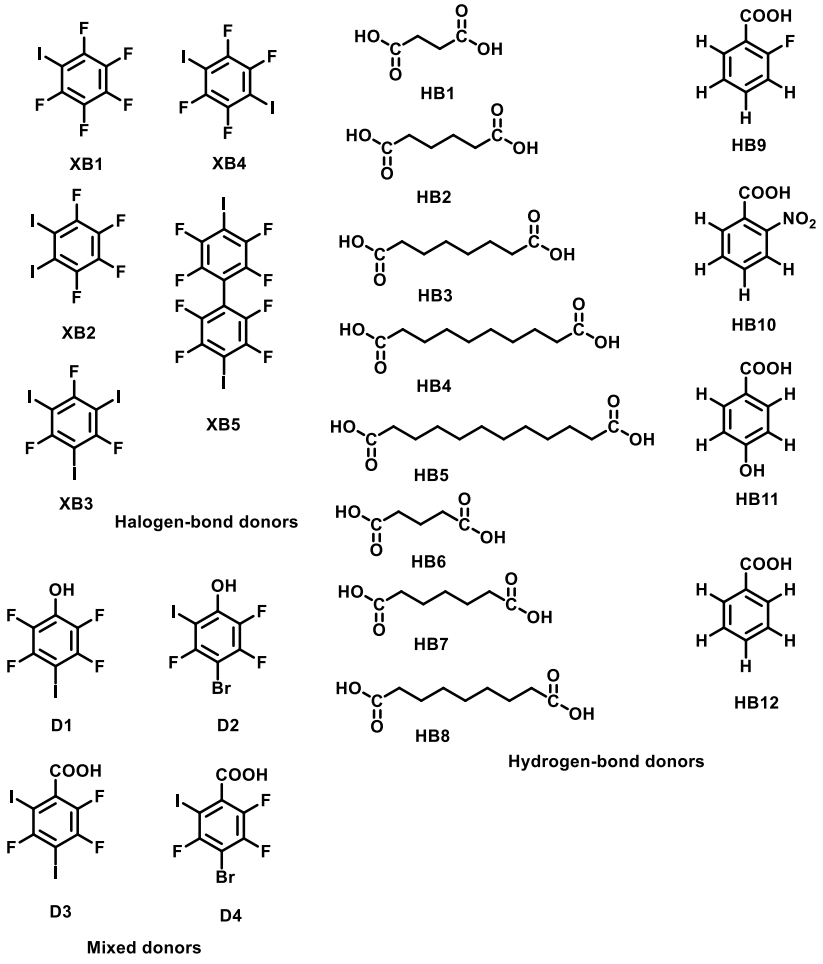

Figure 2-7 Donor molecules used in the co-crystallization experiments

2.2 Experimental

Quinoline-2-carbaldehyde and pyridine-2-carbaldehyde were purchased from Aldrich and utilized without further purification. Hydrogen bond donors **HB1- HB12**, halogen bond donors **XB1-XB5** and mixed donors **D1** and **D2** were purchased from commercial sources and used as received. Mixed donor **D3** and **D4** (Figure 2-7) were prepared according to reported procedures. [1,2,3]triazalo-[3,5-α]quinoline and [1,2,3]triazalo-[3,5-α]pyridine were synthesized following literature data. Melting points were measured using a Fisher-Johns melting point apparatus. ^{1}H

NMR and ^{19}FNMR spectra were reported using a Varian Unity plus 400 MHz spectrophotometer in $CDCl_3$. IR spectra were recorded on a Nicolet 380 FT-IR.

2.2.1 Molecular electrostatic potential calculations

Molecular electrostatic potential surfaces for **A1** and **A2** were obtained via density functional theory (B3LYP) using 6-31G* basis set in vacuum. All calculations were carried out using the Spartan'08 software.

2.2.2 Synthesis of acceptors and donors

2.2.2.1 Synthesis of [1,2,3]triazalo-[3,5-α] quinolone (A1)[19]

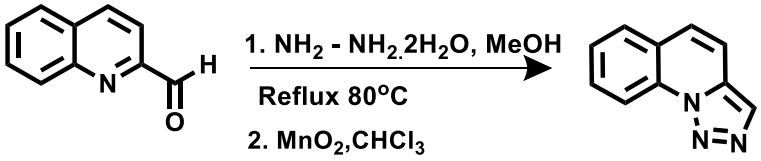

A mixture of quinolone-2-carboxaldehyde (17.5 mmol, 1.37 g) and hydrazine hydrate (206 mmol, 5.20 g, 5.00 ml) was heated under reflux in methanol (50 ml). Upon completion of the reaction (4h), the mixture was quenched with an aqueous solution of NaOH (20 ml, 30%) and the resulting mixture was extracted with dichloromethane (3X50 ml). The organic extracts were combined, washed with brine (20 ml) and dried over anhydrous $MgSO_4$. The mixture was filtered and concentrated to get the corresponding hydrazone. The hydrazone was directly diluted in chloroform (20 ml), then activated manganese dioxide (42.0 mmol 1.85 g) was added, heated under reflux (12h) and the resulting mixture was cooled to room temperature and filtered with celite. After concentrating the solution [1,2,3]triazalo-[3,5-α] quinoline was obtained as a yellow solid. 65% yield. Mp: 135-140^{o}C (Lit value 144^{o}C). ^{1}HNMR (δH,400 MHZ,$CDCl_3$) 8.13 (s 1H), 8.84 (d 1H), 7.88 (d 1H) 7.77 (t 1H) 7.65 (m 2H), 7.56 (d 1H)

2.2.2.2 Synthesis of [1,2,3]triazalo-[3,5-α] pyridine *(A2)*[20]

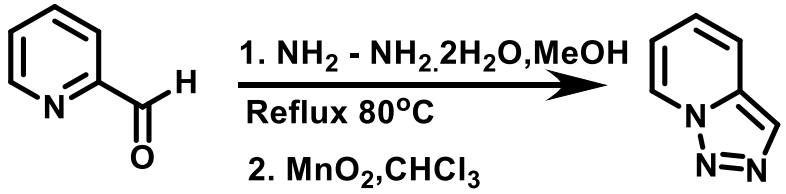

A mixture of pyridine-2-carboxaldehyde (17.5 mmol, 1.37 g) and hydrazine hydrate (206 mmol, 5.20 g, 5.00 ml) was heated under reflux in methanol (50 ml). Upon completion of the reaction (4h), the mixture was quenched with an aqueous solution of NaOH (20 ml, 30%) and the resulting mixture was extracted with dichloromethane (3X 50 ml). The organic extracts were combined, washed with brine (20 ml) dried over anhydrous $MgSO_4$. The mixture was filtered and concentrated to get the corresponding hydrazone. The hydrazone was diluted in chloroform (20 ml) then activated manganese dioxide (42 mmol 1.85 g) was added, heated under reflux (12h) and the resulting mixture was cooled to room temperature and filtered with celite. After concentrating the solution [1,2,3]triazalo-[3,5-α] pyridine was obtained as a yellow solid. 40% yield. M.p: 32-34 ^oC. (Lit value: 34-39^oC). (^{1}HNMR, 400 MHZ, $CDCl_3$ δ H) 8.77 (s 1H) 7.74 (s 1H) 7.27 (t 1H) 7.00 (m 1H)

2.2.2.3 Synthesis of D3[21]

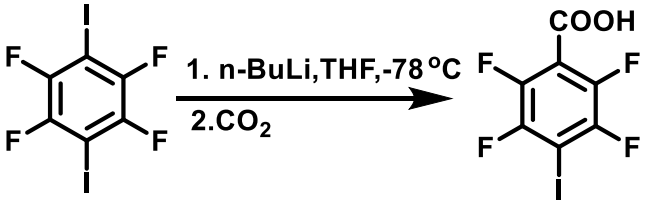

To an oven dried one neck round-bottomed flask equipped with a stir bar, 1,4-diiodo-2,3,5,6-tetrafluorobenzene (1.0 g,2.5 mmol) was added under a stream of N_2 and the flask was sealed with a rubber septum. Freshly distilled THF (70 ml) was added via a cannula. This

solution was cooled to -78^{o}C by immersing into dry ice-acetone bath for 5-7 min. To this solution *n*-butyllithium (1.6 M solutions in hexane, 1.7 ml, 2.6 mmol) was added slowly. After 30 minutes, carbon dioxide gas was purged into the reaction mixture for 15 min followed by addition of excess solid dry ice. The reaction mixture was slowly warmed to 0^{o}C and quenched with 2M HCl. The solvent was removed on a rotary evaporator and the product was extracted in methylene chloride. The organic layer was washed with saturated sodium thiosulfate solution, brine solution and dried over anhydrous $MgSO_4$. Solvent was removed on a rotary evaporator to get the crude product and after washing with hexane the pure product was obtained in 52 % yield. (0.414 g, M.p. 130-135^{o}C) (Lit value 140^{o}C)[21] (^{19}FNMR, 400 MHZ, $CDCl_3$ δ F) -121.33 (2F) -139.89 (2F)

2.2.2.4 Synthesis of D4[21]

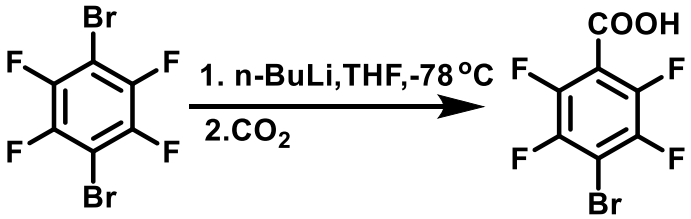

To an oven-dried round-bottomed flask equipped with a stir bar, 1,4-dibromo-2,3,5,6-tetrafluorobenzene (1.0 g,2.5 mmol) was added under a stream of N_2 and the flask was sealed with a rubber septum. Freshly distilled THF (70 ml) was added via a canula. This solution was cooled to -78^{o}C by immersing it into dry ice-acetone bath for 5-7 min. To this solution, *n*-butyllithium (1.6 M solutions in hexane,1.7 ml, 2.6 mmol) was added slowly. After 30 minutes carbon dioxide gas was purged into reaction mixture for 15 min followed by addition of excess solid dry ice to the reaction mixture. The reaction mixture was slowly warmed to 0^{o}C and quenched with 2M HCl. The solvent was removed on a rotary evaporator and product was extracted in methylene chloride. The organic layer was washed with saturated sodium thiosulfate

solution, brine solution and dried over anhydrous $MgSO_4$. The solvent was removed on rotary evaporator to get the pure product in 86 % yield. (0.764 g, M.p 128-130^oC, Lit value 128-130^oC)[21] (^{19}FNMR, 400 MHZ, $CDCl_3$ δ F) -131.72 (2F) -137.14 (2F)

2.2.3 Synthesis of co-crystals[22]

[1,2,3]Triazalo-[3,5-α] quinoline (**A1**) and [1,2,3]triazalo-[3,5-α] pyridine (**A2**) were subjected to co-crystallization against twelve hydrogen bond donors, five halogen bond donors and four mixed donors (Figure 2.7). Donors and acceptors were combined according to the stoichiometric ratio and ground together with a drop of methanol until a solid paste was obtained. The resulting solid was then analyzed via IR spectroscopy for product formation. This procedure was continued for all 42 experiments and X-ray quality single crystals were obtained by dissolving the ground mixture in suitable solvents and allowing slow evaporation or vapor diffusion method. (Eight co-crystals produced single crystals suitable for single-crystal X-ray diffraction)

2.2.3.1 Synthesis of [1,2,3]triazalo-[3,5-α] quinoline pentafluoroiodobenzene, A1:XB1

A1 (0.010 g, 0.060 mmol) was dissolved in 1 mL of ethyl acetate. To this solution pentafluoroiodobenzene (0.035 g, 0.12 mmol) in 1 mL of ethyl acetate was added. The resulting solution was left for slow evaporation in a 2-dram borosilicate vial at room temperature. Colorless prism-shaped crystals were obtained within one week. M.p 85-90^oC.

2.2.3.2 Synthesis of di-[1,2,3]triazalo-[3,5-α] quinoline 1,4-diiodoterafluorobenzene, $(A1)_2$:XB4

A1 (0.010 g, 0.060 mmol) was dissolved in 1 mL of ethyl acetate. To this solution 1,4-diiodotetrafluorobenzene (0.024 g, 0.060 mmol) in 1 mL of ethyl acetate was added. The

resulting solution was left for slow evaporation in a 2-dram borosilicate vial at room temperature. Bronze color plate shaped crystals were obtained within one week. M.p78-84^{o}C.

2.2.3.3 Synthesis of di-[1,2,3]triazalo-[3,5-α] quinolineadipic acid, *$(A1)_2$:HB2*

A1 (0.010 g, 0.060 mmol) and adipic acid (0.004 g, 0.029 mmol) was dissolved in 2 mL of methylenechlorid in a 2-dram borosilicate vial at room temperature. The open vial was kept in a closed container with 4 mL of hexane and left for vapor diffusion. Colorless plate shaped crystals were obtained within one week. M.p100-110^{o}C.

2.2.3.4 Synthesis of di- [1,2,3]triazalo-[3,5-α] quinoline glutaric acid, *$(A1)_2$:HB6*

A1 (0.010 g, 0.06 mmol) was dissolved in a 1 mL of methanol. To this solution glutaric acid (0.039 g, 0.029 mmol) in 1 mL of methanol was added. The resulting solution was left for slow evaporation in a 2-dram borosilicate vial at room temperature. Colorless needle shaped crystals were obtained within one week. M.p75-80^{o}C.

2.2.3.5 Synthesis of [1,2,3]triazalo-[3,5-α] quinoline 2-fluorobenzoic acid, *A1:HB9*

A1 (0.010 g, 0.06 mmol) was dissolved in a 1 mL of methanol. To this solution 2-fluorobenzoic acid (0.0082 g, 0.06 mmol) in 1 mL of methanol was added. The resulting solution was left for slow evaporation in a 2-dram borosilicate vial at room temperature. Bronze color prism shaped crystals were obtained within one week. M.p 62-70^{o}C.

2.2.3.6 Synthesis of di-[1,2,3]triazalo-[3,5-α] quinoline tetrafluoro-4-iodobenzoic acid, *$(A1)_2$:D3*

A1 (0.010 g, 0.060 mmol) and tetrafluoro-4-iodobenzoic acid (0.010 g, 0.029 mmol) was dissolved in 2 mL of methylenechloride in a 2-dram borosilicate vial at room temperature. The open vial was kept in a closed container with 4 mL of hexane and allowed for vapor diffusion. Bronze color plate shaped crystals were obtained within one week. M.p115-120^{o}C.

2.2.3.7 Synthesis of [1,2,3]triazalo-[3,5-α] pyridine and 1,2-diiodotetrafluorobenzene, A2:XB2

A2 (0.010 g, 0.084 mmol) and 1,2-diiodotetrafluorobenzene (0.067 g, 0.17 mmol) was dissolved in 2 mL of methylenechloride in a 2-dram borosilicate vial at room temperature. The open vial was kept in a closed container with 4 mL of hexane and left for vapor diffusion. Colorless prism-shaped crystals were obtained within one week. M.p 55-60^{o}C.

2.2.3.8 Synthesis of [1,2,3]triazalo-[3,5-α] pyridine and 1,3,5-triiodotrifluorobenzene, A2:XB3

A2 (0.010 g, 0.084 mmol) was dissolved in a 1 mL of methanol. To this solution 1,3,5-triiodotrifluorobenzene acid (0.085 g, 0.168 mmol) in 1 mL of methanol was added. The resulting solution was left for slow evaporation in a 2-dram borosilicate vial at room temperature. Colorless prism-shaped crystals were obtained within one week. M.p 105-110^{o}C.

2.2.4 Single crystal X-ray crystallography

All datasets were collected on a Bruker APEX II system using MoKα radiation. Data were collected using APEX2 software. Initial cell constants were found by small widely separated “matrix” runs. Data collection strategies were determined using COSMO. Scan speed and scan widths were chosen based on scattering power and peak rocking curves. All datasets were collected at -153°C using an Oxford Cryostream low-temperature device. Unit cell constants and orientation matrix were improved by least-squares refinement of reflections thresholded from the entire dataset. Integration was performed with SAINT,using this improved unit cell as a starting point. Precise unit cell constants were calculated in SAINT from the final merged dataset. Lorenz and polarization corrections were applied. Multi-scan absorption corrections were performed with SADABS. Data were reduced with SHELXTL. The structures

were solved in all cases by direct methods without incident. Except as noted, hydrogen atoms were located in idealized positions and were treated with a riding model. All non-hydrogen atoms were assigned anisotropic thermal parameters. Refinements continued to convergence, using the recommended weighting schemes. In **A1:HB9** the asymmetric unit contains one molecule each of the triazole-based ligand and aromatic carboxylic acid. The aromatic carboxylic acid molecule is disordered over two closely related positions. The same coordinates have been utilized for atoms occupying the same site using the EXYZ command. Thermal parameters for closely located atoms were pairwise constrained using the EADP command. Coordinates of the carboxylic acid proton H31 was allowed to refine. In **$(A1)_2$:HB6** and **$(A1)_2$:HB2** Coordinates of the carboxylic acid proton H31 was allowed to refine. In **$(A1)_2$:D3** the asymmetric unit contains two molecules of the triazole-based ligand and one molecule of the aromatic carboxylic acid. The aromatic carboxylic acid molecule is disordered over two closely related positions, thus representing different orientations. Relative populations were allowed to refine. Thermal parameters for closely located atoms were pair-wise constrained using EADP commands. Geometry of the aromatic ring was restrained using the SAME command. The bond distances were fixed to idealized distances using the DFIX command

2.3 Results

2.3.1 Molecular electrostatic potential values

Electrostatic potential values of **A1** showed -209 kJ/mol and -171 kJ/mol values on N_1 and N_2, respectively, a difference of 38 kJ/mol between the two acceptor sites. **A2** showed MEPs of -206 kJ/mol and -180 kJ/mol on **N1** and **N2** respectively with a difference of 26 kJ/mol. (Figure 2-8)

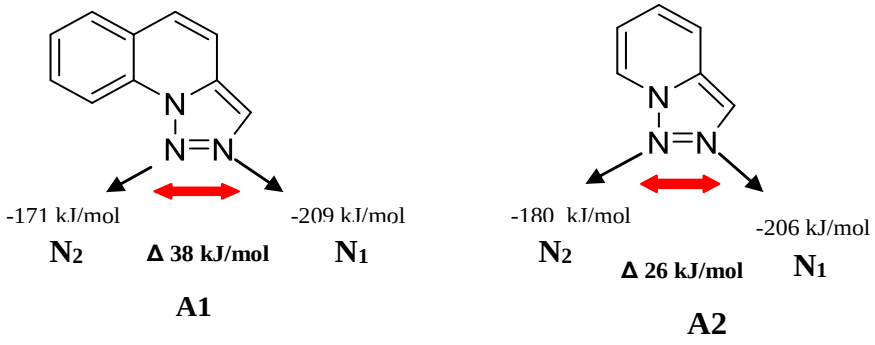

Figure 2-8 Calculated MEP values of A1 and A2

2.3.2. Grinding and IR analysis

A1 and **A2** were initially screened for co-crystal formation using liquid assisted grinding followed by IR spectrometric characterization of the product. Two broad bands around 1850-2450 cm^{-1}, indicative of the formation of intermolecular O-H……N hydrogen bonds,[23] were used as the primary markers for determining co-crystal formation (Figure 2-9).

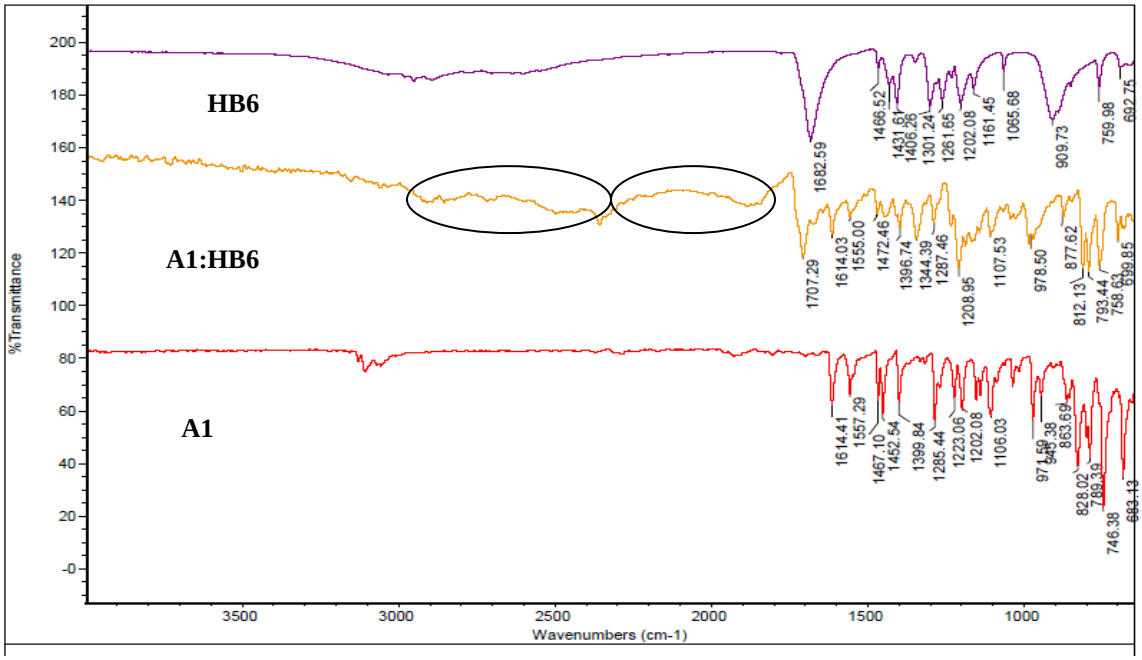

Figure 2-9 IR spectrum of $(A1)_2$:HB6 (middle) with broad bands indicating intermolecular O-H---N interactions (black circle)

Co-crystals with halogen bonds were confirmed by significant changes to several IR stretches in the ground mixture compared to the spectra of the pure acceptor and donor compounds. 33 of the 42 reactions produced co-crystals.

Table 2-1 IR table of grinding experiments of A1 and A2, ✓ indicates a positive result and × indicates a negative result

Hydrogen bond donors	A1	A2	Halogen bond donors	A1	A2
Succinic acid **(HB1)**	✓	✓	Pentafluoroiodobenzene **(XB1)**	✓	✓
Adipic acid **(HB2)**	✓	✓	1,2-Diiodotetrafluorobenzene **(XB2)**	×	✓
Suberic acid **(HB3)**	✓	✓	1,3,5-Triiodotriflurobenzene **(XB3)**	✓	✓
Sebacic acid **(HB4)**	✓	✓	1,4-Diiodotetrafluorobenzene **(XB4)**	✓	✓
Dodecanedioic acid **(HB5)**	✓	✓	4,4'-Diiodo-1,1'-	✓	×

			biphenyloctafluorobenzene **(XB5)**		
Glutaric acid **(HB6)**	✓	✓	**Mixed donors**	**A1**	**A2**
Pimelic acid **(HB7)**	×	✓	4-Iodotetrafluorophenol **(D1)**	✓	✓
Azaleic acid **(HB8)**	×	×	4-Bromotetrafluorophenol **(D2)**	✓	✓
2-Fluorobenzoic acid **(HB9)**	✓	✓	4-Iodotetrafluorobenzoic acid **(D3)**	✓	✓
2-Nitrobenzoic acid **(HB10)**	✓	✓	4-Bromotetrafluorobenzoic acid **(D4)**	✓	✓
4-Hydroxybenzoic acid **(HB11)**	×	×			
Benzoic acid **(HB12)**	×	×			

2.3.3 Analysis of the crystal structures

Even though co-crystal analysis through IR spectroscopy provides unambiguous confirmation of intermolecular hydrogen or halogen bond formation, it does not allow us to determine how the two reactants bind. To understand the molecular interactions, X-ray crystallography was carried out. Figure 2-10 shows the predicted structural outcomes of **A1** and **A2** with different donors.

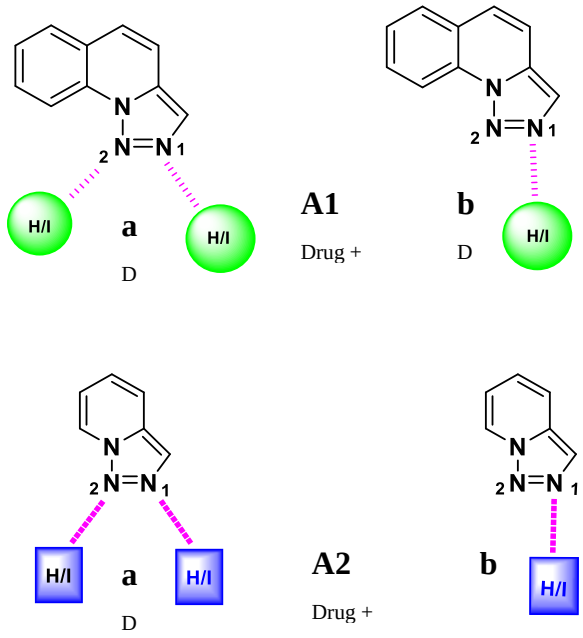

Figure 2-10 Predicted structural outcomes of A1 **and** A2: (a) **no binding preference for** N1 **and** N2 **acceptor sites** (b) **shows a binding preference for best acceptor** N1

2.3.3.1Crystal structure of A1:XB1

The crystal structure of **A1:XB1** was obtained in a 1:1 stoichiometry. The structure showed a discrete architecture with the formation of a halogen bond between an activated iodine atom and **N_1** from the acceptor with the highest electrostatic potential value. The **N_2** acceptor atom with the lowest electrostatic potential value does not participate in any significant halogen-bond interaction (Figure 2-11).

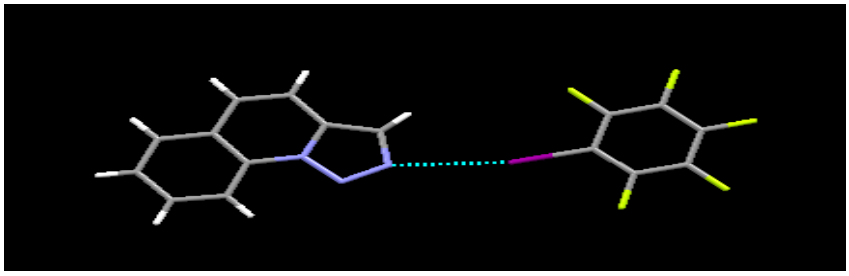

Figure 2-11 N---I halogen bond formed between N_1 **and** XB1

2.3.3.2 Crystal structure of $(A1)_2$*:XB4*

In the crystal structure of **$(A1)_2$:XB4** both iodine atoms in the ditopic halogen bond donor, form halogen bonds with **N_1** (highest electrostatic potential value). Similar to the previous structure **N_2** (with the lowest electrostatic potential value) does not form any significant halogen bonds or short contacts (Figure 2-12).

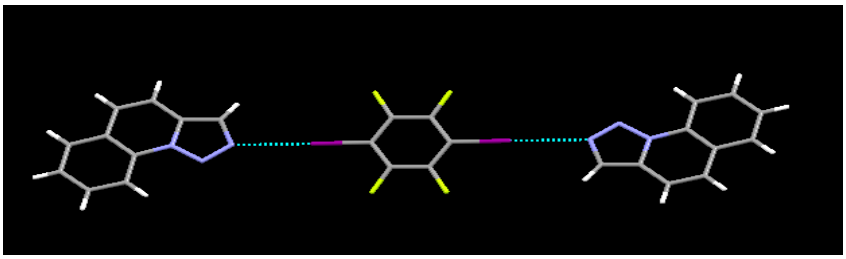

Figure 2-12 XB4 forms N----I halogen bonds with N_1

2.3.3.3 Crystal structure of $(A1)_2$*:HB2 and* $(A1)_2$*:HB6*

The crystal structure of **A1** with both **HB2** and **HB6** showed a 2:1 stoichiometry. Similar to halogen- bond interactions both ditopic carboxylic acids forms discrete architecture via O-H---N interactions with **N_1**. **N_2** did not participate in any significant hydrogen-bond interaction (Figure 2-13).

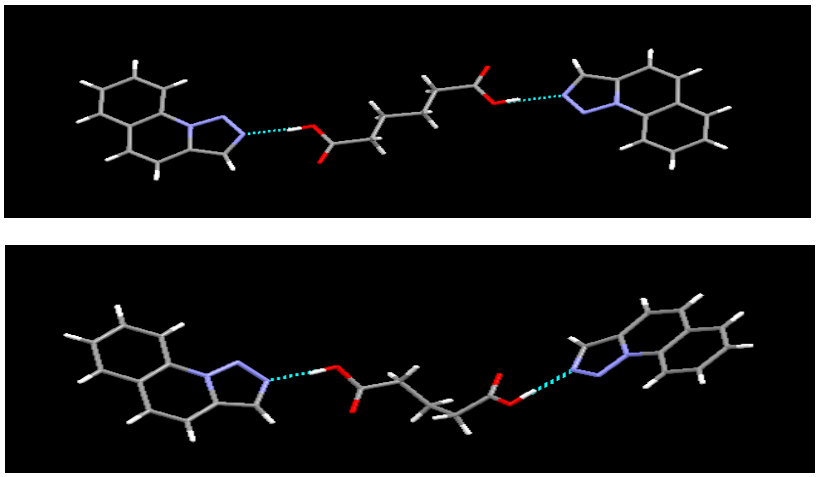

Figure 2-13 O-H----N hydrogen-bond interaction formed between N1 and –OH group of the carboxylic acids (top: $(A1)_2$:HB2 **and bottom** :$(A1)_2$:HB6)

2.3.3.4 Crystal structure of (A1):HB9

The crystal structure of **A1** with **HB9** showed 1:1 stoichiometry, with O-H---N hydrogen bond interaction between the acceptor site $\mathbf{N_1}$ leaving the second-best acceptor site intact (Figure 2-14).

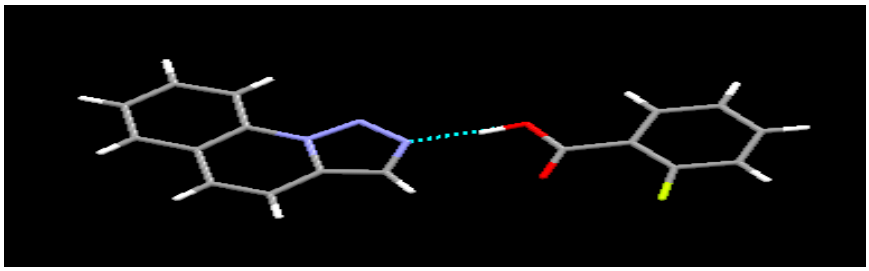

Figure 2-14 O-H----N hydrogen-bond formation between N1 and O-H in (A1):HB9

2.3.3.5 Crystal structure of $(A1)_2$:D1

The crystal structure of **A1** with **D1** showed 2:1 stoichiometry and this structure again led to a discrete architecture. The iodine atom and the O-H group formed N---I and O-H---N interactions respectively. This structure shows that both hydrogen and halogen based donors prefer to form intermolecular interactions with the best acceptor site $\mathbf{N_1}$ (Figure 2-15).

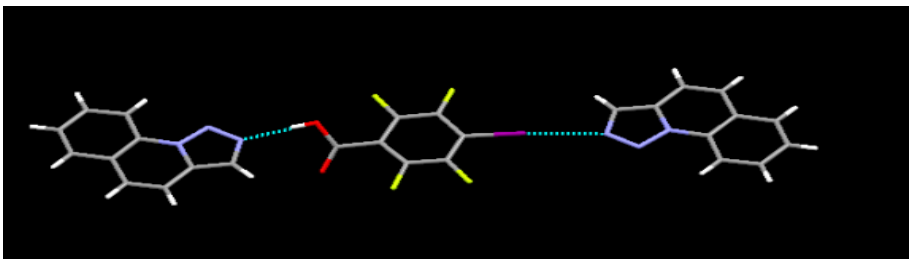

Figure 2-15 O-H---N and N---I interactions formed by –OH and I groups, respectively with N1 **of** A1

2.3.3.6 Crystal structures of A2:XB2 and A2:XB3

The Crystal structure of **A2** with **XB2** and **XB3** showed that, both nitrogen atoms in **A2** form halogen bonds. There is no selectivity in forming non-covalent interactions even though $\mathbf{N_1}$ has a higher positive electrostatic potential value. However, there was a significant difference in the bond lengths of the halogen-bond interactions formed by $\mathbf{N_1}$ and $\mathbf{N_2}$**.** The $\mathbf{N_1}$----I bond is shorter than the $\mathbf{N_2}$---I interactions. (**A2:XB2,** 2.907(4), 2.9883(3), respectively and **A2:XB3,** 2.845 (3),2.992 (3) respectively. This data suggests that halogen-bond interaction with the best acceptor (site with the highest positive electrostatic potential) is stronger than the interaction with the second-best acceptor (Figure 2-16).

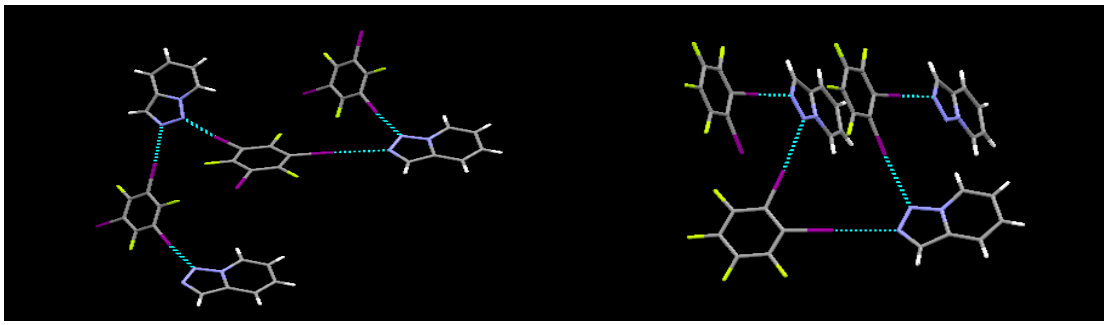

Figure 2-16 Crystal structure of A2:XB2 **(right) and** A2:XB3 **(left) with N1----I and N2----I halogen-bond interactions**

Table 2-2 Bond lengths and angles of hydrogen bonds in the crystal structures

Compound		D-H (Å)	H----A (Å)	D----A (Å)	DH-A (°)
$(A1)_2$:HB6	O(31)-H(31)---N(13)	1.00(3)	1.68(3)	2.679(3)	175(3)
$(A1)_2$:HB2	O(31)-H(31)---N(13)	0.940(16)	1.767(16)	2.7022(13)	172.5(14)
A1:HB9	O(31)-H(31)---N(13)	1.006(18)	1.652(18)	2.6544(15)	173.2(16)
$(A1)_2$:D3	$O(51_A)$-$H(51_A)$----N(13)	0.84	1.89	2.725(3)	175.1
	$O(51_B)$-$H(51_B)$---N(33)	0.84	1.92	2.751(6)	73.1

Table 2-3 Bond lengths and angles of halogen bonds in the crystal structures

Compound		X----A (Å)	DX—A (º)
A1:XB1	**N(13)---I(1)**	**3.0662(17)**	**167.49(6)**
$(A1)_2$:XB4	**N(13)---I(1)**	**2.99379(14)**	**175.98(5)**
A2:XB2	**N(12)---I(1)** **N(13)---I(2)**	**2.988(3)** **2.907(4)**	**171.93(13)** **179.53(13)**
A2:XB3	**N(13)---I(1)** **N(12)---I(2)**	**2.845(3)** **2.992(3)**	**177.31(10)** **173.32(11)**

2.4 Discussion

2.4.1 Hydrogen and halogen bond prediction through IR spectroscopy

Co-crystal analysis of **A1** and **A2** with hydrogen and halogen bond donors was initially carried out through IR spectroscopy. In this study, donor molecules with carboxylic acid groups were primarily chosen as the hydrogen-bond donors and the fluorinated iodine carrying molecules were chosen as the halogen-bond donors. Therefore, changes of the main functional groups in both halogen and hydrogen bond donors can be used as indicative of co-crystal formation. In the hydrogen bonded networks co-crystal formation were mainly identified through characteristic double "humps" for O-H---N interaction which appeared in 1800-2200 cm^{-1} and 2300-2600 cm^{-1} region.

2.4.2 Interpretation of the structural outcomes

A1 and **A2** both contain two possible acceptor sites. The analysis of the crystal structures of **A1** showed that with both halogen and hydrogen bond donors the acceptor site with the highest electrostatic potential value (-206 kJ/mol) had a preference for forming an intermolecular interaction over the acceptor site with the lower electrostatic potential value (Figure 2-17).

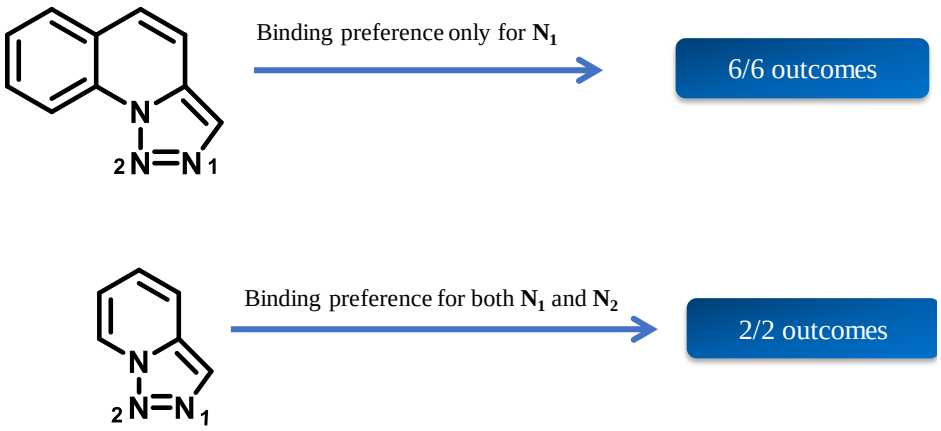

Figure 2-17 Structural outcomes of A1 and A2 in co-crystallization experiments

Even though the difference between two acceptor sites is only38 kJ/mol it is still enough to make one acceptor site preferred over the other. This conclusion was supported by all six crystal structures. Two co-crystals of **A2** (with a potential difference of 26 kJ/mol) suitable for X-ray diffraction were obtained with halogen bond donors. In the crystal structures of **A2:XB2** and **A2:XB3**, both nitrogen atoms participated in halogen bonding indicating that the electrostatic potential difference between two acceptor sites is not large enough to make one site structurally dominant. This observation was consistent with previous results which showed that MEPs difference < 30 kJ/mol is strong not enough to make structural selectivity.

2.4.3 Elimination of a geometrical explanation for selectivity in A1

Even though the understanding all six crystal structures of **A1** underscores the importance of MEPs in predicting outcomes of potential competing non-covalent interactions it was possible that this supramolecular selectivity was the result of some geometric factor which prevented the second nitrogen atom from participating in forming either a hydrogen or a halogen bond. However the crystal structure of **A1** by itself shows that both nitrogen atoms in **A1** are available for hydrogen- bond formation, which include C-H---N (best acceptor) and C-H---N (second best acceptor) hydrogen bonds (Figure 2-18).

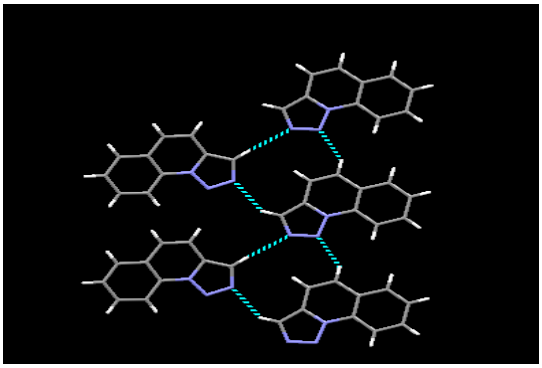

Figure 2-18 Crystal structure of A1 showing that both N1 and N2 are capable in forming intermolecular interactions

This suggests that there is no inherent geometric barrier in this molecule which would prevent it from forming a halogen/ hydrogen bonds with $\mathbf{N_2}$. Therefore, as $\mathbf{N_1}$ is engaged in hydrogen bonds in all six co-crystals of **A1** the results correlate with the calculated MEPs values.

2.5 Conclusion

Our experimental data suggest that a simple electrostatic approach for ranking different interaction sites provides reliable guidelines in predicting outcome of competing non-covalent interactions. We have not carried out extensive polymorph screening for each supramolecular reaction, however we assume that the molecular preferences showed by **A1** and **A2** will not change drastically even if several new structures were to be added. The analysis of **A1** by itself showed that both acceptor atoms are accessible to form non-covalent interactions. This observation confirms that the outcomes are not related to the steric effect of the molecules.

To summarize our results,

1) The electrostatic potential difference of 38 kJ/mol is enough to produce selectivity within the structural landscapes in multitopic acceptors, but the selectivity is lost when this difference is < 30 kJ/mol

2) With the difference of 38 kJ/mol the acceptor site with the highest electrostatic potential value can be labeled as the best acceptor, but with a difference of < 30 kJ/mol both acceptor sites have equal preference in XB/HB interactions

3) Crystal structures of **A1** and **A2** with different halogen and hydrogen bond donors showed 6/6 and 2/2 structural outcomes, respectively showing that calculated MEPs values can be used for successful structural outcome predictions.

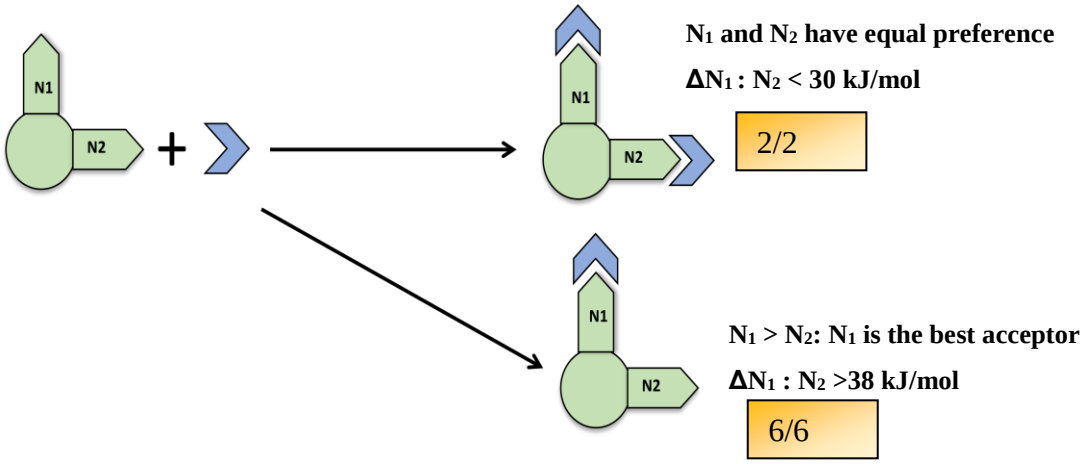

Figure 2-19 Overview of the structural outcomes with new boundaries

2.6 References

1. G. R. Desiraju, *Angew. Chem. Int. Ed.*, 1995, **34**, 2311-2327.
2. J. A. Z. Donovan N.Chin, Hohn C. Macdonald, George M.Whitesides, ed. J. K.Whitesell, John Wiley and Sons Ltd, 1999.
3. J. Fayos and F. H. Cano, *Cryst Growth Des.*, 2002, **2**, 591-599.
4. G. R. Desiraju, *Cryst. Growth Des.*, 2011, **11**, 896-898.
5. E. D. Glowacki, M. Irimia-Vladu, S. Bauer and N. S. Sariciftci, *J. Mater. Chem. B*, 2013, **1**, 3742-3753.

6. M. C. Etter, *Acc. Chem. Res.*, 1990, **23**, 120-126.

7. Z. U.-L. Margaret C. Etter, S Mohammad Zia-Ebrahimi, and Thomas W. Panunto' *J. Am. Chem. Soc*, 1990, **112**.

8. C. A. Hunter, *Angew. Chem. Int. Ed.*, 2004, **43**, 5310-5324.

9. C. B. Aakeröy and K. Epa, *Top. Curr. Chem.*, 2014, **351**, 125-147.

10. C. B. Aakeröy, C. L. Spartz, S. Dembowski, S. Dwyre and J. Desper, *IUCrJ*, 2015, **2**, 498-510; P. W. Kenny, *J. Chem. Inf. Model.*, 2009, **49**, 1234-1244.

11. N. G. White, A. Caballero and P. D. Beer, *CrystEngComm*, 2014, **16**, 3722-3729; L. C. Gilday, S. W. Robinson, T. A. Barendt, M. J. Langton, B. R. Mullaney and P. D. Beer, *Chem. Rev.*, 2015, **115**, 7118-7195.

12. G. Cavallo, P. Metrangolo, R. Milani, T. Pilati, A. Priimagi, G. Resnati and G. Terraneo, *Chem. Rev.*, 2016, **116**, 2478-2601.

13. P. Politzer, J. S. Murray and T. Clark, *Phys. Chem. Chem. Phys.*, 2010, **12**, 7748-7757.

14. L. C. Roper, C. Prasang, A. C. Whitwood and D. W. Bruce, *CrystEngComm*, 2010, **12**, 3382-3384.

15. T. M. Beale, M. G. Chudzinski, M. G. Sarwar and M. S. Taylor, *Chem. Soc. Rev.*, 2013, **42**, 1667-1680.

16. C. B. Aakeröy, K. Epa, S. Forbes, N. Schultheiss and J. Desper, *Chem. Eur. J.*, 2013, **19**, 14998-15003.

17. C. B. Aakeröy, T. K. Wijethunga and J. Desper, *New J. Chem.*, 2015, **39**, 822-828; M. D. Perera, J. Desper, A. S. Sinha and C. B. Aakeroy, *CrystEngComm*, 2016, **18**, 8631-8636.

18. C. B. Aakeroy, T. K. Wijethunga and J. Desper, *J. Mol. Struct.*, 2014, **1072**, 20-27.

19. R. Ballesteros-Garrido, F. R. Leroux, R. Ballesteros, B. Abarca and F. Colobert, *Tetrahedron*, 2009, **65**, 4410-4417.

20. F. Blanco, I. Alkorta, J. Elguero, V. Cruz, B. Abarca and R. Ballesteros, *Tetrahedron*, 2008, **64**, 11150-11158.

21. C. B. Aakeröy, S. Panikkattu, P. D. Chopade and J. Desper, *CrystEngComm*, 2013, **15**, 3125-3136.

22. D. Hasa, G. Schneider Rauber, D. Voinovich and W. Jones, *Angew. Chem. Int. Ed.*, 2015, **54**, 7371-7375.

23. C. B. Aakeroy, S. V. Panikkattu, B. DeHaven and J. Desper, *Cryst. Growth Des.*, 2012, **12**, 2579-2587.

Chapter 3 - Halogen-bond based organocatalysis: An alternative to hydrogen-bond based catalysis

3.1 Introduction

3.1.1. Organocatalysis by hydrogen bonding

Organocatalysis is referred to as the use of small organic molecules to catalyze organic transformations, and the emergence of this type of catalysis has huge impact on organic synthesis over the last two decades.[1] Organic catalysis has had many advantages compared to the classic metal- based catalysis: it is cheap, non-toxic and insensitive to moisture and air. Due to these properties, organocatalysis is attractive to the scientific community, particularly in the pharmaceutical industry where the presence of metal ions causes problems in-vivo.[2] Activation of substrates through organocatalyis is mainly divided into two categories:[3]covalent catalysis and non-covalent catalysis[4] (Figure 3-1).

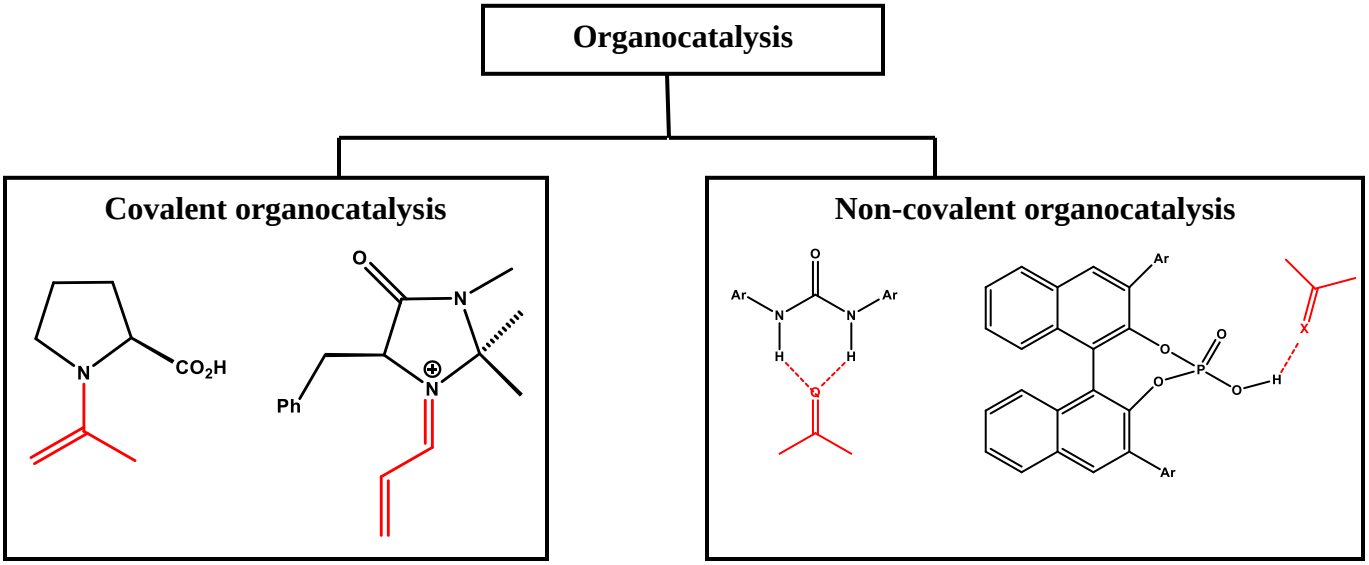

Figure 3-1 Two main categories of organocatalysis

The most powerful non-covalent interaction used to date is hydrogen bonding and [2,3] most common hydrogen-bond based concepts in organocatalysis are bidentate functional groups, mainly with thiourea derivatives dominating the field. Figure 3-2 shows two examples of thiourea based organocatalysis which uses two different concepts of modes of activation. First example is a benchmark Diels-Alder reaction, where the hydrogen-bond donors bind to the carbonyl moiety and activates the substrate through electron withdrawal.[5] Second example shows the binding of anions (mainly halides) released during the course of an S_N1-type reaction.[6] Removal of anions through hydrogen- bond formation enhances the product formation by increasing the reaction rate.

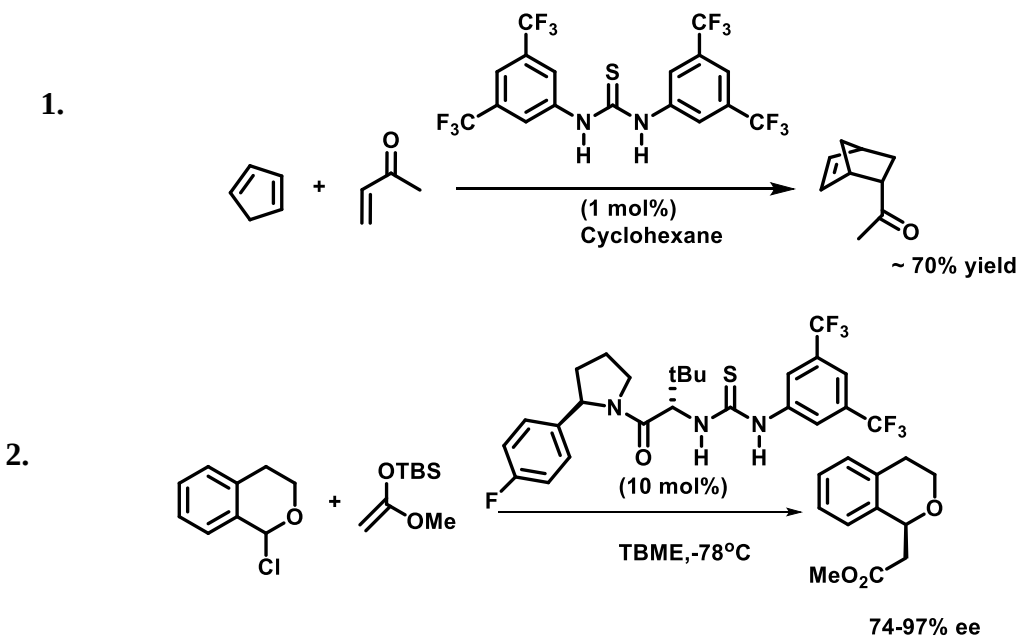

Figure 3-2 Two examples of hydrogen-bond based organocatalysis 1. Based on the activation of a carbonyl compound 2. Based on the activation through halide abstraction[5, 6]

3.1.2 Comparison of hydrogen and halogen bond based systems

Even though halogen bonds are considered as a close kin to hydrogen bonds, there are some distinctive features which make halogen bonds more suitable in organocatalysis. Halogen bonds are more directional (R-X----LB ~ 180^{o}C) than hydrogen bonds, which is due to the repulsion of halogen lone pairs with the Lewis base at obtuse angles. Also halogen bonding provides more tunability than hydrogen bonding, with the availability of four principle halogen atoms (F,Cl,Br,and I).[7] Lewis acidity of halogen bond donors increases in the order of Cl<Br<I with the increase of polarizability.[8, 9] However there are very few examples of fluorine acting as a halogen-bond donor[10] and interactions are mainly based on iodine-based halogen-bond donors. With the increase of electronegativity of the halogen bearing substituent, more Lewis- acidic halogen-bond donors are produced and mostly polyfluorinated or cationic moieties are used as backbones (Figure 3-3).

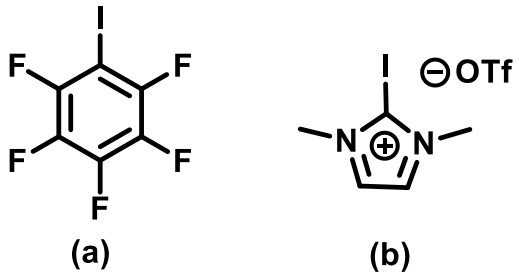

Figure 3-3 Common backbones used in halogen-bond based adducts; (a) fluorinated backbone (b) cationic backbone

Since polyfluorinated halogen-bond donors are apolar, they may be used for applications that rely on low polarity, whereas the hydrogen-bond based systems are often considered as polar with the presence of polar –OH or –NH groups.[11] Another prominent difference in halogen-bond based systems is the electronic nature of the hydrogen and halogen atoms. Since hydrogen and iodine reside on the opposite ends of the periodic table, there is a significant difference in orbital

size and polarizability. Therefore hydrogen-bond based systems and halogen-bond based systems can be used for different classes of Lewis bases in organocatalysis.[9]

3.1.3 Concept use in halogen-bond based catalysis

Similar to thiourea based catalysts, we can use mono or multidentate halogen-bond donors as Lewis acidic activators (catalysts), however using mulidentate donors is more advantageous since these molecules bind more strongly to the substrate and create a more rigid structure. Figure 3-4 shows the concept transfer of hydrogen-bond donors and halogen bond donors in a multidentate system.[9]

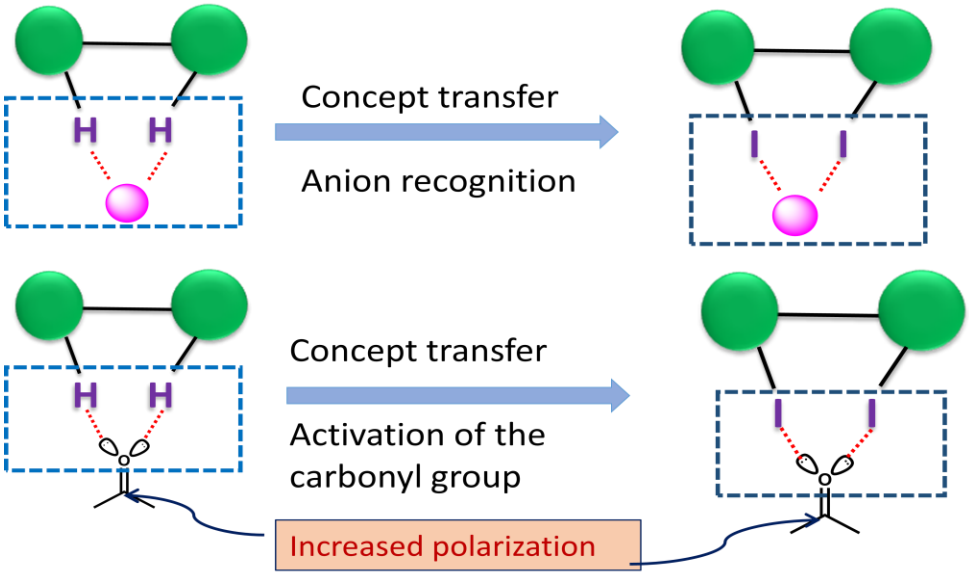

Figure 3-4 Concept transfer from a hydrogen-bond based system to a halogen-bond based system

In the anion-bonding approach, halogen-bond donors interact with the leaving anion which is formed during a S_N1 reaction. With the removal of the anion the reaction will be accelerated, however the liberated anion binds strongly to the halogen-bond donors and there is a strong risk of catalyst inhibition and catalytic transformation requires special reaction design[9] (Figure 3-5).

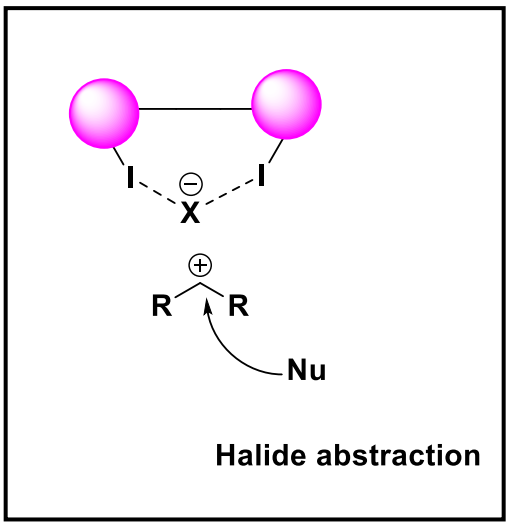

Figure 3-5 Mode of activation through halide abstraction

3.1.4 Examples of halogen based organocatalysis

Even though halogen based organocatalysis provides a new avenue in organic chemistry there are only few multidentate halogen-bond donors reported and the synthesis and design is significantly challenging due to the limited availability of backbones. Therefore halogen-bond based catalysis is still an emerging area. In most of the early studies, evidence of activation of substrates through halogen bonding was not clearly reported as they were unable to rule out the hidden acid based catalysis and the exact mode of action was not properly understood.[12] However in recent studies Huber and his co-workers reported on a few examples of halogen-based organocatalysis, ruling out other possible substrate activations and provide significant evidence for catalysis, purely based on halogen- bond donors. They synthesized different cationic and neutral halogen-bond donors which were applied to many bench mark reactions to observe the effect of halogen-bond donors in catalysis (Figure 3-6).[9, 13, 14]

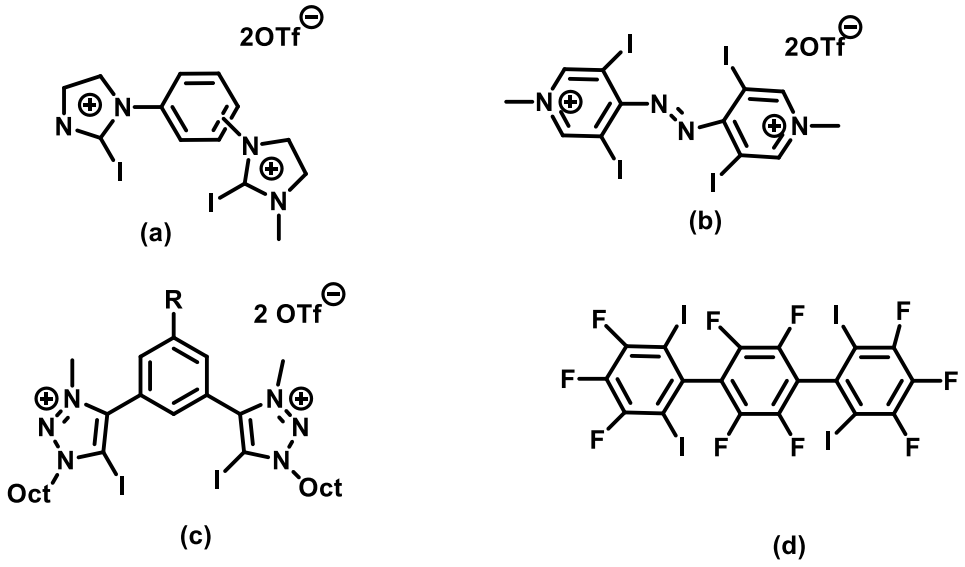

Figure 3-6 Examples of cationic and polyfluorinated backbones used in halogen-based catalytic systems.

In one such example, activation of carbonyl compounds through halogen bonding was reported using a benchmark Diels-Alder reaction. In this study, cationic halogen-based catalysts were used in the presence of non-coordinating BAr_4F^- anion. A 63 % product formation was formed, compared to a thiourea- based catalyst, which produced only 38 % (Figure 3-7 and 3-8).

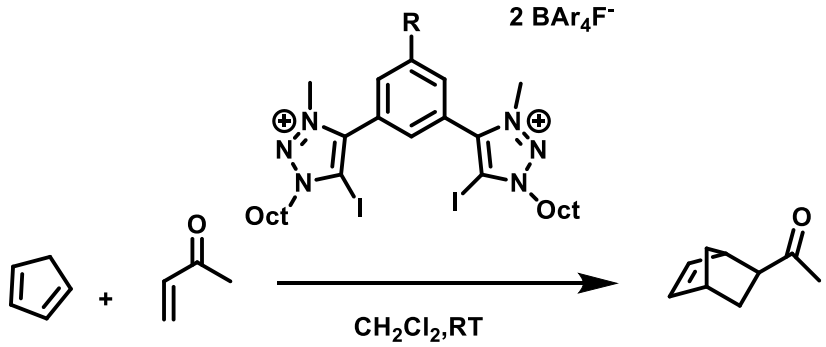

Figure 3-7 Benchmark Diels-Alder reaction for catalytic studies based on halogen bonding

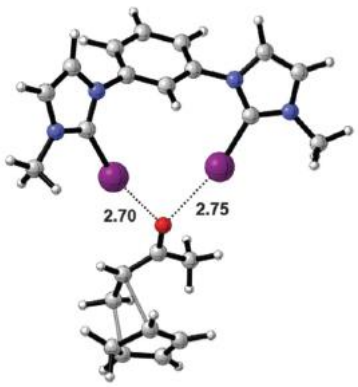

Figure 3-8 Proposed mechanism of carbonyl activation through halogen bonding

Although the first steps were taken towards designing halogen-based catalysts, it is still underdeveloped. Therefore, it is important to develop suitable catalysts and reaction conditions using the knowledge of existing solid state crystal structures to apply the concept of halogen-based catalysis into more complex structures.

3.1.5 Goals of this study

With increasing demand for halogen–bond based catalysis as an alternative to well-known hydrogen-bond based catalysis, we decided to apply our knowledge in designing halogen based supramolecular synthons for solid state applications to solution based studies to design an effective catalytic system.

The goals are,

1) To synthesize a suitable halogen-based catalyst
2) To observe the catalytic activity in a benchmark reaction through anion recognition mechanism
3) To eliminate possible hidden catalysis and confirm the feasibility of halogen bond donors in the catalysis using control molecules

3.2 Experimental

All the chemicals were purchased from available commercial sources and used without further purification.^{1}H NMR was reported using a Varian Unity plus 400 MHz spectrophotometer in $CDCl_3$. IR Spectroscopy was carried out on a Nicolet 380 FT-IR. Melting points were measured on Fisher-Johns melting point apparatus.

3.2.1 Synthesis of a new halogen- bond based catalyst (L1)

A new class of catalyst was designed based on an iodine group as a halogen-bond donor. The iodine group was activated by attaching to a *sp* hybridized carbon atom. To compare the catalytic activity of the activated halogen-bond donor, two control molecules, one without any halogen atom and another molecule without activating the halogen atom was synthesized. After successful synthesis, catalytic activity was analyzed on a benchmark Ritter-type solvolysis reaction.

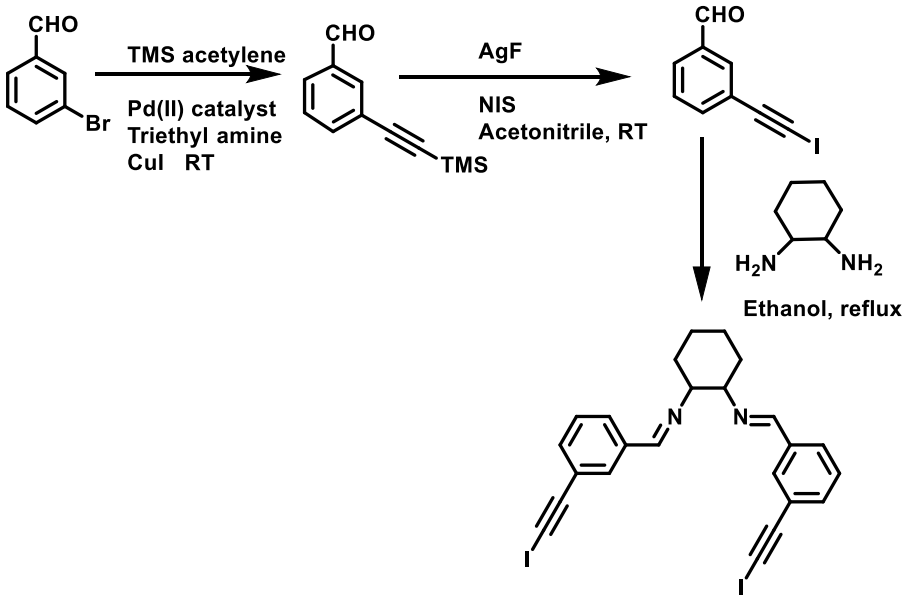

Figure 3-9 Reaction scheme for the synthesis of L1

3.2.1.1 Synthesis of 3-((trimethylsilyl)ethynyl)benzaldehyde

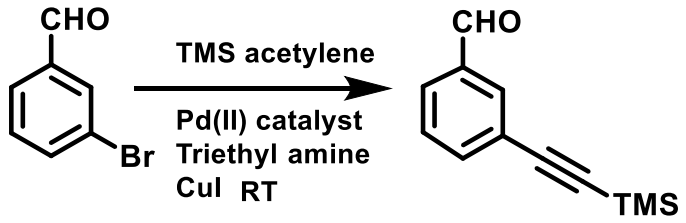

To a one-neck round-bottom flask equipped with a stir bar, 3-bromobenzaldehyde (1.89 mL, 0.0162 mmol) and 150 mL of triethyl amine were added and degassed with nitrogen gas for 20 mins. To the reaction mixture (0.113 g, 0.162 mmol) of *bis*(triphenylphosphine)palladium*(*II*)* dichloride and (0.0600 g, 0.324 mmol) of CuI was added followed by the addition of trimethylsilyl acetylene (2.5 mL,0.0178 mol). Nitrogen gas was bubbled through the mixture for an additional 30 min until the reaction medium was saturated and the reaction was stirred at room temperature for 24 hours. Upon the completion of the reaction (confirmed by TLC), the solvent was removed by rotary evaporator. The resulting solid was extracted in $CHCl_3$, washed with brine and dried over anhydrous Mg_2SO_4. The organic layer was removed in a rotary evaporator and the pure product was obtained as a brown color liquid (43%) after column chromatography with hexane. (^{1}HNMR, $CDCl_3$, δH) 9.98 (s 1H), 7.96 (s 1H), 7.81 (d 1H) 7.69 (d 1H) 7.47 (t 1H)

3.2.1.2 Synthesis of 3-(iodoethynyl)benzaldehyde

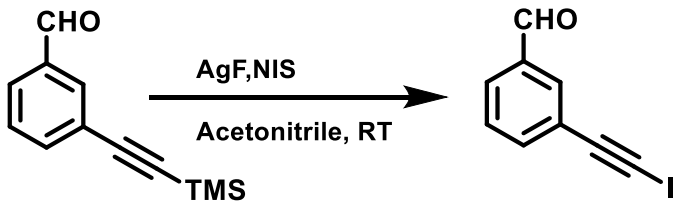

To a one-neck round-bottom flask equipped with a stir bar, 3-trimethylsilyl benzaldehyde (1.4 g, 6.9 mmol) and 0.87 g (6.9 mmol) of silverfluoride was added followed by the addition of 75 mL of acetonitrile. The flask was then wrapped with aluminum foil and the stirring was continued for 24 hrs. The reaction mixture was then passed through a silica plug using acetonitrile and concentrated using a rotary evaporator. The resulting solid was then extracted in diethyl ether and washed with water. After concentration, pure yellow color product was obtained in 88% yield. (1.50 g) M.p 95-100^{o}C, ^{1}HNMR, $CDCl_3$, δ H) 9.99 (s 1H) 7.94 (d 1H) 7.82 (d 1H) 7.68 9d 1H) 7.51 (t 1H)

3.2.1.3 Synthesis of N,N'-(cyclohexane-1,2-diyl)bis(1-(3-iodoethynyl)phenylmethanimine (L1)

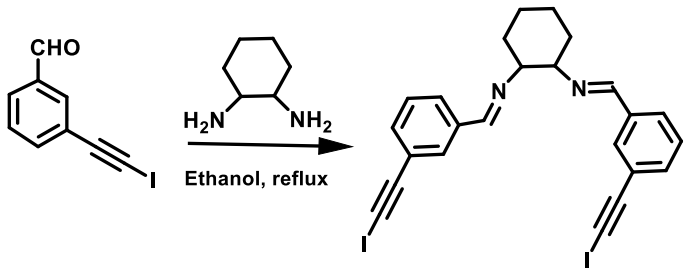

To 0.068 g (0.60 mmol) of 1,2-diaminocyclohexane, 100 mL of ethanol was added and heated to 70^{o}C for 10 min. To this a solution of 3-(iodoethynyl)benzaldehyde (0.30 g, 1.2 mmol) was added and heated under reflux for 2 hrs. The reaction mixture was cooled and the volume

was reduced to half using a rotary evaporator. To the reaction 200 mL of water was then added to induce precipitation. The resulting solid was filtered and redissolved in 120 mL of methylene chloride, washed with distilled water and brine. The organic layer was evaporated and the resulting brown color solid was collected in 60 % yield. M.p 60-65^{o}C (^{1} HNMR, DMSO-d_6 δ H) 8.18 (s 1H) 7.62 (d 2H) 7.41(d 1H) 7.34 (t 1H) 3.18 (s 1H) 15-1.8 (m 5H)

3.2.1.4 Synthesis of N,N'-(cyclohexane-1,2-diyl)bis(1-phenylmethanimine) *(L1-phenyl)*

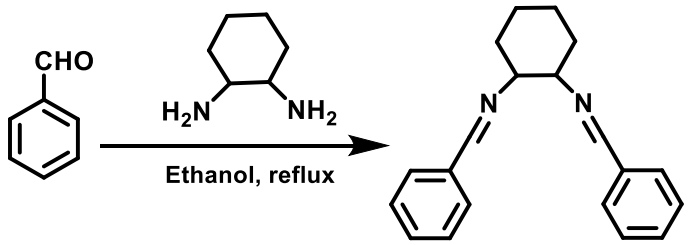

To 1,2-diaminocyclohexane (0.23 g, 2.0 mmol) 100 mL of ethanol was added and heated to 70^{o} for 10 min. To the reaction mixture, 0.42 g, 4.0 mmol of benzaldehyde was added and heated under reflux for 2 hrs. The volume was reduced to half using a rotary evaporator and to the reaction mixture was then added 200 mL of water to induce precipitation. The resulted solid was redissolved in 120 mL of methylene chloride, washed with water and brine. After concentrating the organic layer, the product was obtained in 80% yield as a white solid. M.p 115-120^{o}C (^{1}HNMR DMSO-d_6 δ H) 8.18 (s 1H) 7.60 (m 3H) 7.35(m 2H) 3.41(s 1H) 1.45-1.85 (m 4H)

3.2.1.5 Synthesis of N,N'-(cyclohexane-1,2-diyl)bis(1-(3-chlorophenyl)methanimine)

(L1-Chloro)

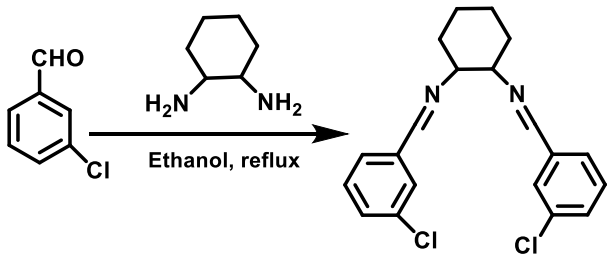

To 1, 2-diaminocyclohexane (0.11 g, 1.0 mmol) 100 mL of ethanol was added and heated to 70^{o} for 10 min. To the reaction mixture 0.25 g, 2.0 mmol of 3-chlorobenzaldehyde was added and heated under reflux for 2 hrs. The volume was reduced to half using a rotary evaporator and to the reaction mixture 200 mL of water was added to induce precipitation. The resulting solid was re-dissolved in 120 mL of methylene chloride, washed with water and brine. After concentrating the organic layer product was obtained in 75% yield as a white solid. M.p 95-100^{o}C (^{1}HNMR DMSO-d_6 δ H) 8.18 (s 1H) 7.61 (d 2H) 7.39 (d 2H) 3.34 (s 1H) 1.42-1.77 (m 4H)

3.2.2 Analysis of the catalytic activity

Catalytic activity of **L1, L1-Chloro** and **L-Phenyl** were measured using the benchmark Ritter-type solvolysis of benzhydryl bromide in acetonitrile. (The benchmark Diels-Alder reaction was not studied due to the poor solubility of **L1** in methylene chloride) (Figure 3-10).

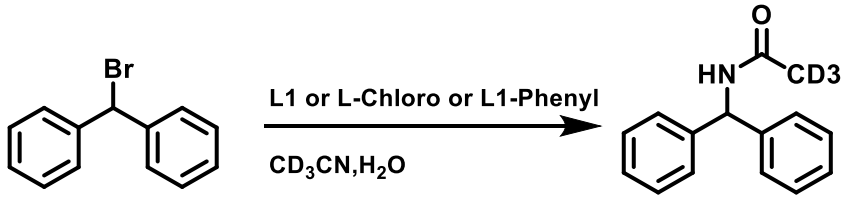

Figure 3-10 Benchmark Ritter type solvolysis of the benzhydryl bromide

3.2.2.1 Initial screening of the catalytic activity

Benzyhydryl bromide (0.0098 g, 0.0040 mmol) was dissolved in 0.5 mL of CD_3CN at room temperature in a 2-dram borosilicate vial. **L1** 0.020 g, (100 %) 0.040 mmol dissolved in 0.5 ml of CD_3CN was then added and the reaction was stirred at room temperature for 24 h, 48 h, 72 h and 96 h. Temperature was kept constant by keeping the reaction mixture in a water bath. At each time interval, the reaction progress was monitored using ^{1}H NMR spectroscopy. The procedure was repeated using 0.0020 g (10 %) and 0.0040 g (20%) of **L1** to

observe the changes of activity with respect to the amount of catalyst. Each experiment was performed three times. The reaction progress without any catalyst was analyzed by dissolving 0.0098 g of benzhydryl bromide in 1 mL of CD_3CN and stirring at room temperature without any catalyst for 24 h, 48 h, 72 h and 96 h. Reaction progress was analyzed using ^1H NMR spectroscopy. Reaction was carried out with **L1-Phenyl** and **L1-Chloro** to observe any catalytic activity without halogen-bond donors as activating agents. Benzyhydryl bromide (0.0098 g, 0.040 mmol) was dissolved in 0.5 mL of CD_3CN in a 2-dram vial and to the mixture 0.014 g (stoichiometric amount) of **L1-Chloro** in 0.5 mL of CD_3CN was added. The reaction was stirred at room temperature for 24 h, 48 h, 72 h and 96 h. Reaction progress was monitored using ^1H NMR spectroscopy. The reaction was repeated for **L1-phenyl** (0.012 g, stoichiometric amount) following the same procedure.

3.3 Results and discussion

3.3.1 Choice of the catalyst

One of the biggest challenges in designing a functional halogen-bond based catalyst is having a suitable backbone with an activated halogen atom which has the capability to form a strong halogen-bond. In our previous studies we found that the iodo ethynyl group has a potential to form strong halogen-bonds with nitrogen based acceptor groups and halide anions (Figure 3-11).

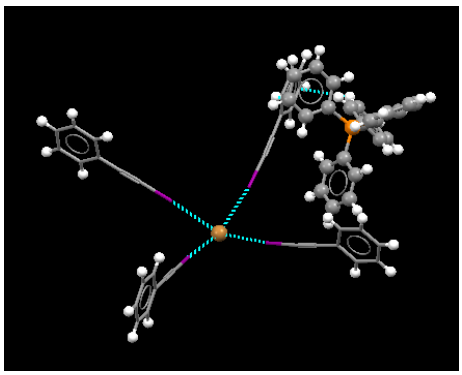

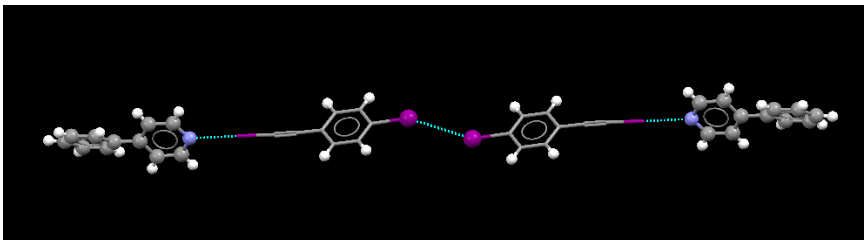

Figure 3-11 Examples of iodo ethynyl group acting as a halogen-bond donor (top) with Br^- ion (bottom) with nitrogen and iodine acceptor groups

In order to combine two iodo-ethynyl fragments, we used Schiff-base approach on a 1,2-diaminocyclohexane backbone. This molecule may form a chelate or due to the flexible nature of the bonds, the molecule may also act as a "bridge" between two anions. (Figure 3-12)

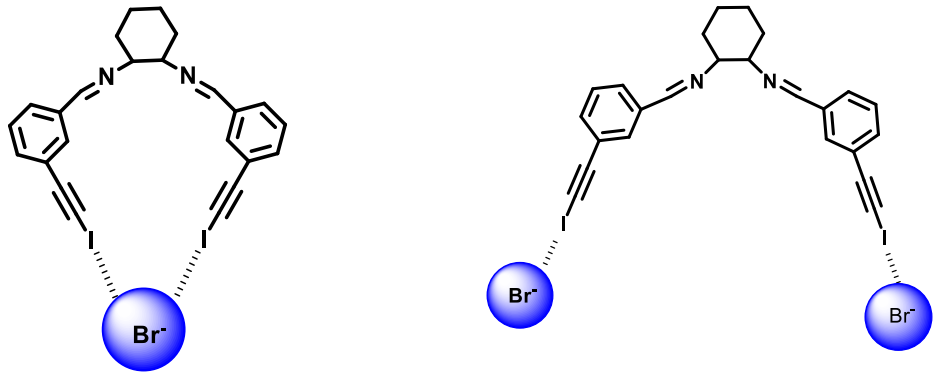

Figure 3-12 Two possible arrangements of L1 **with bromide anions**

3.3.2 Choice of the reaction

Huber and co-workers established that Ritter-type solvolysis of benzhydryl bromide is an ideal benchmark reaction to study catalytic activity based on halide abstraction (Figure 3-13).[9] In this reaction, acetonitrile is used both as a solvent and as a nucleophile and the intermediate nitrilium ion reacts with the traces of water in the solvent to form N-benzhydryl acetamide.

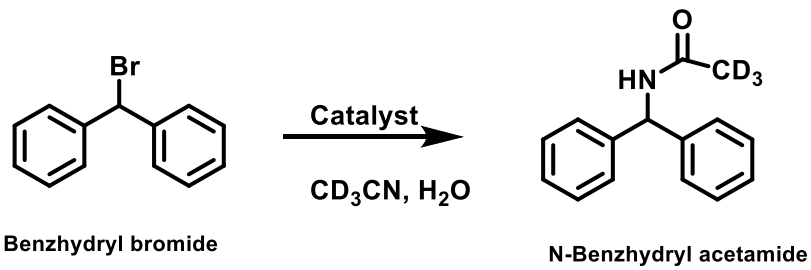

Figure 3-13 Ritter-type solvolysis of benzhydryl bromide

Since there are no additional reagents required, side reactions are not observed and this provides an ideal environment to study halogen-bond based catalysis. However, during the reaction, weakening of the C-Br bond can take place as a result of a C-I---Br halogen bond and in an extreme situation this may lead to a heterolytic cleavage. An additional driving force may arise by the insolubility of the halogen-bond complex formed between the halogen-bond donor and the halide anion (Figure 3.14). Therefore, there is a possibility that the halogen-bond donor (catalyst) might not be available for further substrate activity and thus stoichiometric amounts of catalyst might be required.

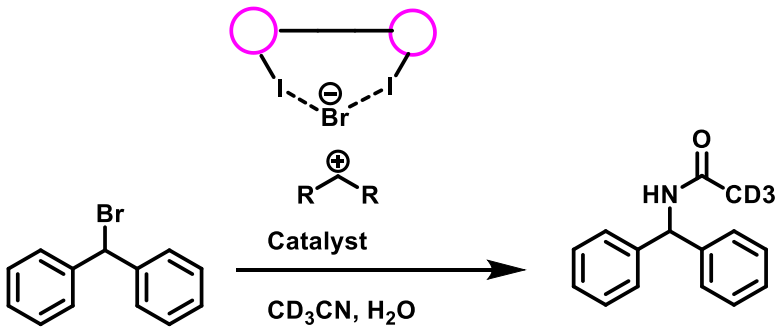

Figure 3-14 Halide abstraction and complex formation with the catalyst during the reaction

3.3.3 Analysis of the catalytic activity

Product formation was determined using ^{1}HNMR spectroscopy by measuring the ratio of the product peak (literature value appears around 6.15-6.30 ppm) to the peak of the starting

material, (singlet at 6.45 ppm), however based on the coordination with activating agent or H^+ position of the peak can be varied,[14, 15] and in our experiment a new peak appeared around 5.77 ppm. No product was formed without any catalyst even after 96 hrs (Figure 3-15).

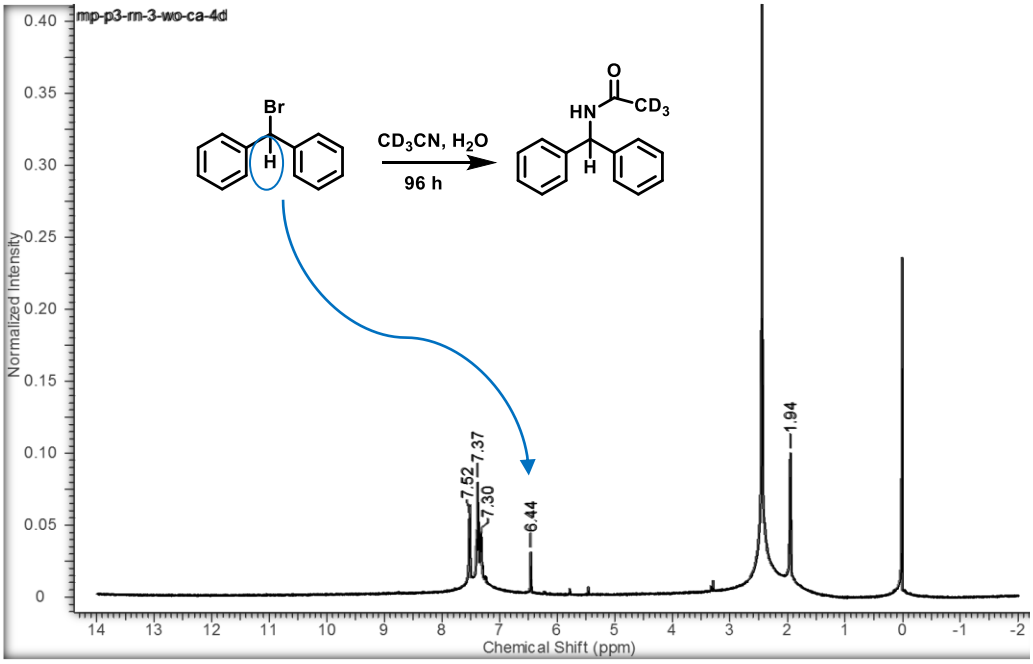

Figure 3-15 ^{1}HNMR spectrum of the reaction without any catalyst after 96 hrs

According to the ^{1}H NMR spectra the addition of **L1** (100% loading) resulted in 90 % conversion of starting material to the product after 96 hrs. No side products or decomposition products of **L1** were appeared in the NMR spectra. When 10 % of **L1** was added, the product conversion was 33 % and with 20% addition this was increased to 63 % conversion. This observation confirms the stoichiometric effect of the catalyst during the reaction progress.

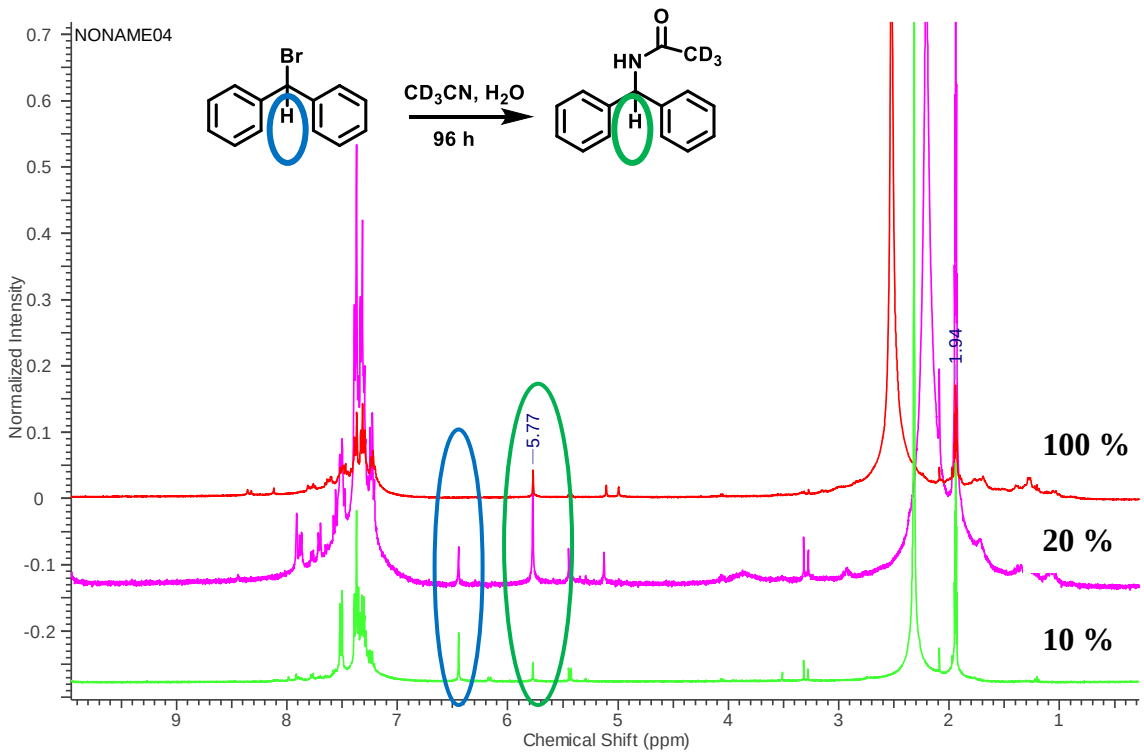

Figure 3-16 Reaction progress with different catalytic loading

Analysis of the catalytic activity in different time intervals showed that activity reached its maximum after 96 hrs (Table 3-1 and Figure 3-17). Therefore the optimum conditions for the catalytic system are; stoichiometric amount of catalyst loading and 96 hr reaction time.

Table 3-1 Reaction progress over the time with changes of the catalytic amount

Amount of L1	**^{1}HNMR yields**		
	24 h	**48 h**	**96 h**
10 %	21.6 %	32.5 %	33 %
20 %	25.6 %	38.3 %	63 %
100 %	33 %	66 %	90 %

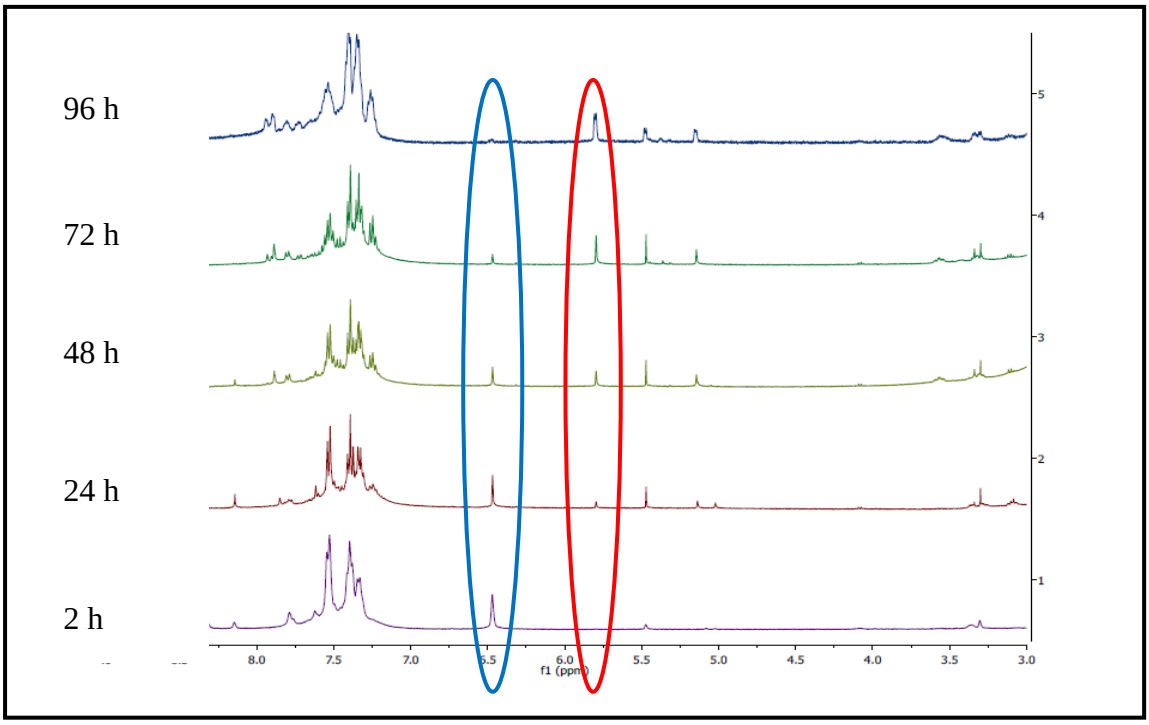

Figure 3-17 Reaction progress of L1 **with change of time; with 100 % loading, blue circles represents the changes of the starting material and the red circle shows the product formation**

During the reaction progress, we noticed a precipitate formation and we suspect that halogen-bond donor might not be available for further reactivity. This assumption was further supported by the disappearance of ^{1}HNMR peaks in the product spectrum and analysis of the precipitate confirmed the presence of the peaks associated with the catalyst (Figure 3-18).

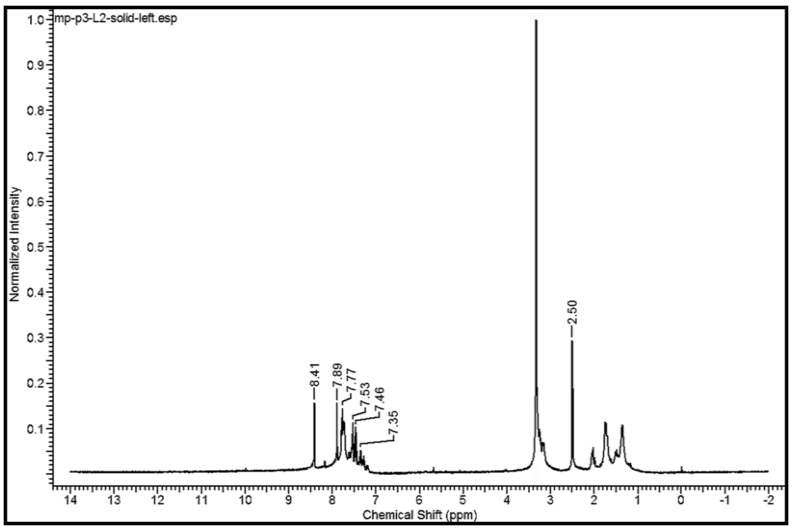

Figure 3-18 ^{1}HNMR spectrum of the precipitate, formed during the reaction

These results were confirmed by the repetitive experiments. Comparative experiments with non-iodinated and with an un halogen-bond donor respectively were carried out to confirm that source of the catalytic activity is halogen bonding. In using **L1-phenyl** as a catalyst after 96 hrs with loading a stoichiometric amount we found < 5% product formation and appearance of additional peaks in the ^{1}HNMR spectrum (Figure 3.19). Similar observation was seen with **L1-Chloro.** The appearance of additional peaks suggests that both **L1-phenyl** and **L1-chloro** decompose during the reaction and have no effect to the catalytic activity (Figure 3-19).

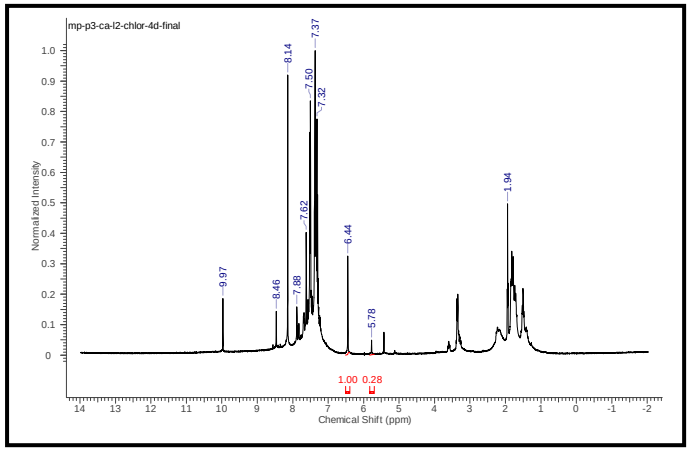

Figure 3-19 Appearance of additional peaks in the NMR spectrum of L1-Chloro **after the reaction**

In theory if acetonitrile get hydrolyzed in the presence of **L1,** it could generate acetamide and over the time it could react with benzhydryl bromide. This hypothesis was ruled out by analyzing **L1** in acetonitrile for several days; acetamide was not detected. Since we used a Schiff base approach to synthesize catalyst molecules we could not use acids as a control to rule out any hidden acid catalysis in the reaction (imine bonds are susceptible for hydrolysis). But in a previous study Huber and his co-workers has used 5 % of HOTf for Ritter-type solvolysis of benzhydryl bromide and confirmed that there is a very little effect (< 25 % yield) of acid and catalytic activity can be atributed to halogen bonding. In the same study they confirmed that the HBr generated during the reaction is not active in an autocatalytic way.[14] Consequently we can state that the results obtained with **L1** are strongly indicative of a halogen-bond donor as a catalyst.

3.4 Conclusion

In this study, we introduced a iodo ethynyl based halogen-bond donor molecule as a catalyst and successfully used it in a bench mark Ritter-type solvolysis reaction. Control studies effectively ruled out the hidden catalysis based on the presence of other functional groups and confirmed the catalytic activity is based on halogen bonding. The optimum conditions for the catalytic system were; a stoichiometric amount for 96 hrs. Through this study we were able to add another proof to the limited pool of halogen based catalysts and in future we will analyze the activity and modify our catalyst for different reactions to obtain better results.

3.5 References

1. H. Pellissier, *Tetrahedron*, 2007, **63**, 9267-9331; I. R. Shaikh, *J. Catal.*, 2014, **2014**, 35.
2. O. V. Shishkin, R. I. Zubatyuk, S. V. Shishkina, V. V. Dyakonenko and V. V. Medviediev, *PCCP*, 2014, **16**, 6773-6786.
3. D. W. C. MacMillan, *Nature*, 2008, **455**, 304-308; C. Palumbo and M. Guidotti, *ScienceOpen Research*, 2014, **0**, 1-14.
4. A. Moyano, in *Stereoselective Organocatalysis*, John Wiley & Sons, Inc., 2013, DOI: 10.1002/9781118604755.ch02, pp. 11-80.
5. A. Wittkopp and P. R. Schreiner, *Chem. Eur.J.*, 2003, **9**, 407-414.
6. S. E. Reisman, A. G. Doyle and E. N. Jacobsen, *J. Am. Chem. Soc.*, 2008, **130**, 7198-7199.
7. A. Mukherjee, S. Tothadi and G. R. Desiraju, *Acc. Chem. Res.*, 2014, **47**, 2514-2524.
8. G. Cavallo, P. Metrangolo, R. Milani, T. Pilati, A. Priimagi, G. Resnati and G. Terraneo, *Chem. Rev.*, 2016, **116**, 2478-2601.
9. D. Bulfield and S. M. Huber, *Chem. Eur. J.*, 2016, **22**, 14434-14450.
10. P. Metrangolo, J. S. Murray, T. Pilati, P. Politzer, G. Resnati and G. Terraneo, *CrystEngComm*, 2011, **13**, 6593-6596.
11. S. Beckendorf, S. Asmus, C. Mück-Lichtenfeld and O. García Mancheño, *Chem. Eur. J.*, 2013, **19**, 1581-1585.
12. O. Coulembier, F. Meyer and P. Dubois, *Polymer Chemistry*, 2010, **1**, 434-437; M. A. P. Angelika Bruckmann, Carsten Bolm, *Synlett.*, 2008, **6**, 900-902.
13. S. H. Jungbauer and S. M. Huber, *J. Am. Chem. Soc.*, 2015, **137**, 12110-12120; S. H. Jungbauer, S. M. Walter, S. Schindler, L. Rout, F. Kniep and S. M. Huber, *Chem.*

Commun., 2014, **50**, 6281-6284; F. Kniep, S. H. Jungbauer, Q. Zhang, S. M. Walter, S. Schindler, I. Schnapperelle, E. Herdtweck and S. M. Huber, *Angew. Chem. Int. Ed.*, 2013, **52**, 7028-7032.

14. F. Kniep, S. M. Walter, E. Herdtweck and S. M. Huber, *Chem. Eur. J.*, 2012, **18**, 1306-1310.

15. S. M. Walter, F. Kniep, E. Herdtweck and S. M. Huber, *Angew. Chem. Int. Ed.*, 2011, **50**, 7187-7191.

Chapter 4 - Usage of structural mimics in exploring structural landscapes of poorly soluble molecular solids: An insight for future API-co-crystallization

4.1 Introduction

4.1.1 Importance of co-crystallization

Pharmaceuticals generally comprise of an active pharmaceutical ingredient (API), a formulation containing an inactive material as a carrier system, and a package for market performance and appeal.[1]Crystalline API's are strongly preferred due to the ease of isolation, and physio-chemical stability that the crystalline solid state affords.[2] However, designing new active pharmaceutical ingredients (API) in their crystalline forms is often challenging due to poor solubility[2] of API as it limits adsorption and bioavailability *in vivo*.[3] Many drug candidates do not reach the market due to poor solubility and therefore this is a key parameter that needs to be addressed at several stages of drug discovery and formulation.[4] According to the Biopharmaceutical classification system (BCS) APIs can be divided into four main classes:[5] Class 1, drug candidates that have good solubility and good permeability; Class II, drugs that have good membrane permeability but poor solubility; Class III, molecules with high solubility but poor permeability. Class IV drugs are poorly soluble as well as poorly permeable through the membrane (Figure 4-1). Class III and class IV drugs often fail to reach the final stage of drug discovery due to poor optimum properties.[5]

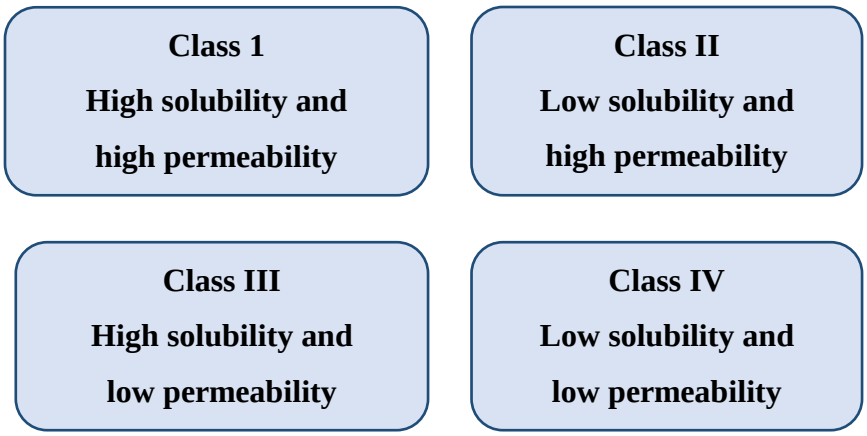

Figure 4-1 BCS classification of API's

Crystalline forms of API's are primarily limited to salts, polymorphs and solvates, however crystal engineering affords another prototype for the development of a fourth class of APIs called pharmaceutical co-crystals.[2] In 2016, the FDA released their guidance on co-crystal classification which indicates that co-crystals, along with salts and polymorphs, are likely to play important roles in future discussions and developments of new APIs.[6] "Co-crystals are considered as crystalline materials composed of two or more molecules in the same crystal lattice"[7] and in the definition of pharmaceutical co-crystals[8] one component in the crystal lattice is the therapeutic agent (Figure 4-2). Co-crystals are formed through non-covalent interactions which does not involve any breaking or making covalent bonds, [9] and this technique can therefore be used to fine-tune physical properties of API through precise control over molecular assembly without affecting the therapeutic activity.[10]

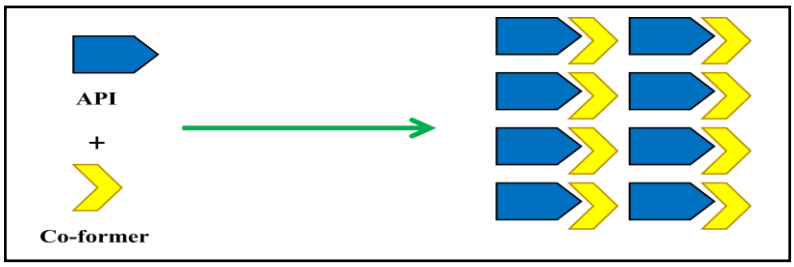

Figure 4-2 Co-crystal formation between an API and a co-former via non-covalent interactions

A typical co-crystal screen is often carried out via liquid-assisted grinding[11] followed by an analysis of the resulting solid using infra-red,[12] Raman spectroscopy[13] or X-ray powder diffraction.[13] Although these methods can determine if a new solid form has been obtained, a more detailed picture of how the two components interact with one another requires that the crystal structure of the new solid be solved. Unfortunately, effective crystal growth of co-crystals composed of a poorly soluble API and a more soluble co-former can be very challenging due to the tendency of precipitation of the less soluble substance as a homogenous solid, thus leaving the co-former behind in solution. Consequently, it can be very difficult to obtain enough information about the structural landscape that surrounds a particular target, which will hamper the development of robust and practical guidelines for co-crystal synthesis of high-value compounds.

4.1.2 Importance of structural mimics

In order to overcome the problems outlined in 4.1.1, we decided to explore the use of 'structural mimics' as a way of extracting key information which allows us to indirectly construct the structural landscape of a molecule of interest. A suitable 'structural mimic' should carry the same primary functional groups as the target which provides the ability to form the same primary intermolecular interactions as those displayed by the target. In addition, the mimic would not need to carry chemical functionalities that caused the molecule to be so poorly soluble since those fragments are unlikely to play key role in co-crystal formation (although they are of course critical for its biological activity). The dominant structural features of the pure drug also need to be preserved in the crystal structure of the mimic itself in order for it to be considered as an appropriate 'structural mimic'. Non–covalent interactions formed by mimic molecule can then be easily compared to the actual drug by preserving the main functional groups in both

molecules. In crystal engineering it has been shown that functional groups of different molecules behave comparably when similar environmental conditions are provided.[14] Therefore we may use the concept of "structural mimics" to map out binding preferences and to modulate physical properties of poorly soluble API's.

4.1.3 Choice of API for the study

Erlotinib sold as a hydrochloride salt under the brand name Tarceva,[15] was selected as the target molecule in this study. Erlotinib is used to treat non-small cell lung cancer, pancreatic cancer and several other types of cancer and is known as a tyrosine kinase inhibitor.[15] Erlotinib hydrochloride has its maximum aqueous solubility (≈ 0.4 mg/ml) at a pH of approximately 2 but as this drug is administered in an acidic form it is not an ideal drug candidate for cancer patients with gastrointestinal issues.[16] There are nine entries in the CSD of erlotinib related structures, seven of them are salts or hydrates, and there is only one genuine co-crystal (with urea as the co-former).[17] Interestingly, according to Desiraju and co-workers the native drug has a tendency to convert to its monohydrate during co-crystallizations which adds an element of uncertainty to the preparation of new solid forms of erlotinib.[17] Therefore we decided to synthesize a structural mimic of erlotinib in order to make co-crystals thereof that could offer more information about the structural landscape of the native substance itself.

Erlotinib has two heterocyclic nitrogen atoms that can act as hydrogen-bond acceptors, and one N-H and one ethynyl proton both of which can act as hydrogen-bond donors, (Figure 4-3) As these functional groups are likely to play important roles in the primary intermolecular interactions in the native drug, we wanted to preserve these four recognition sites (and their relative orientation) in the mimic. The remaining alkyl groups (which lower the aqueous

solubility) were discarded as they were not thought to be important drivers for co-crystal formation.

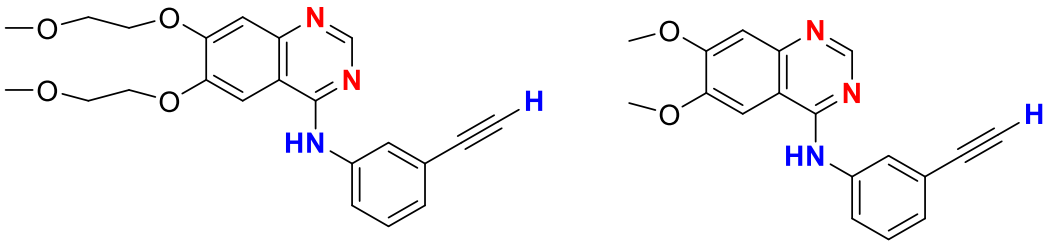

Figure 4-3 Potential acceptor (red) and donor moieties (blue) in erlotinib (left), and of its structural mimic (right)

4.1.4 Goals of the study

Goals of this study are,

1) To synthesize a structural mimic to erlotinib
2) To carry co-crystallization experiments of the mimic with water soluble dicarboxylic acids
3) To analyse the crystal structures of the mimic to identify main interactions
4) To examine the aqueous solubilty of new solid forms to correlate molecular properties of co-former to dial-in physical properties of co-crystals
5) To correlate the structural behaviour of the mimic with the actual drug molecule

4.2 Experimental

4-Chloro-6, 7-dimethoxyquinazoline and 3-ethynylaniline was purchased directly from Alfa Aesar and used without further purification. Other reagents and co-formers were purchased from available commercial sources and utilized without further purification. Melting points were measured using Fisher-Johns melting point apparatus. ^{1}H NMR was reported using a Varian Unity plus 400 MHz spectrophotometer in $CDCl_3$. IR Spectroscopy was carried out on a Nicolet 380 FT-IR. PXRD was taken on Rigaku miniflex 600 and UV measurements were taken on Shimadzu UV-1650 PC.

4.2.1 Synthesis of N-(3-ethynylphenyl)-6-7-dimethoxyquinazolin-4-amine(A1)[18, 19]

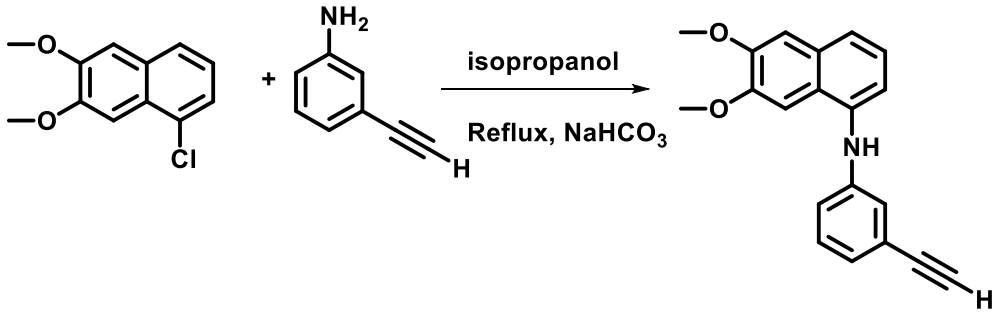

4-Chloro-6,7-dimethoxyquinazoline (200 mg, 0.89 mmol) and 3-ethynylaniline (0.13 g, 1.6 mmol) were mixed and refluxed in 25 ml of 2-propanol for 1h. Resulting white solid was filtered and dissolved in 50 ml of methanol. Solution was basified with sat. $NaHCO_3$ and extracted in to chloroform. A slightly brownish solid was obtained after concentration. (70% yield). M.p: 275-280^{o}C. (Lit. 290-292^{o}C)[19] (^{1}HNMR, DMSO-*d6* δ H) 8.68(s 1H) 7.80 (s 1H) 7.29 (t 1H) 7.26 (t 1H) 7.22 (s 1H) 6.97 (s 1H) 5.29 (s 1H) 3.96 (d 6 H) 3.07 (s 1H)

4.2.2 Molecular electrostatic potential calculations

Molecular electrostatic potential surfaces for erlotinib and **A1** were obtained via density functional theory (B3LYP) using 6-31G* basis set in vacuum. All calculations were carried out using the Spartan'08 software.

4.2.3 Synthesis of co-crystals and salts of A1

A1 (10 mg) and the co-former (succinic acid, adipic acid, suberic acid, sebacic acid and dodecanedioic acid respectively) were mixed in 2:1 ratio and ground on a spotting plate with the help of a drop of methanol. The ground mixture was then analyzed via IR spectroscopy for initial screening. Co-crystal formation was demonstrated by the appearance of two broad bands indicative of O-H...N hydrogen bonds at around 1850-2450 cm^{-1} [20], and of significant shifts of the carbonyl stretch of di-acids around 1650-1700 $cm^{-}1$. Four of the five experiments produced a co-crystal, only the combination with sebacic acid failed to produce the targeted multi component solid. We subsequently attempted to grow crystals suitable for single-crystal X-ray diffraction of all five ground mixtures. Suitable crystals were obtained for the four co-crystals but only homomeric solids (recrystallizations) were produced in the combination of **A1** and sebasic acid. Since the erlotinib is administered as the hydrochloride salt, to understand the behavior of our mimic in the salt form, the hydrochloride salt of the **A1** was also synthesized and analyzed via X-ray crystallography.

4.2.3.1 Synthesis of N-(3-ethynylphenyl)-6-7-dimethoxyquinazolin-4-aminechloride A1H^{+}:Cl^{-}

4-Chloro-6,7-dimethoxyquinazoline (100 mg, 0.44 mmol) and 3-ethynylaniline (0.063 g, 0.80 mmol) were mixed and refluxed in 12.5 ml of 2-propanol for 1h. The resulting white solid

was filtered and recrystallized in water: methanol (1:1) mixture. (M.p: 255-260^{o}C) (Lit: 269-270^{o}C)[18]

4.2.3.2 Synthesis of di-N-(3-ethynylphenyl)-6-7-dimethoxyquinazolin-4-aminesuccinic acid (A)$_2$:SUC)

A1 (10 mg) was mixed with 2 mg of succinic acid and dissolved in 4 mL of methylenechloride and ethyl acetate mixture in a 2 dram borosilicate vial at room temperature. The mixture was allowed to slow evaporate and colorless block crystals were obtained within one week.

4.2.3.3 Synthesis N-(3-ethynylphenyl)-6-7-dimethoxyquinazolin-4-amineadipate (A1H)$_2^+$:ADP$^-$:ADP.MeOH)

Adipic acid (2.4 mg) was mixed with 10 mg of **A1** and dissolved in 2 ml of methanol in a 2-dram borosilicate vial. After letting the solution to slow evaporate colorless block crystals were obtained within two weeks.

4.2.3.4 Synthesis of di-N-(3-ethynylphenyl)-6-7-dimethoxyquinazolin-4-aminesuberic acid (A1$_2$:SUB)

To **A1**(10 mg), 2.8mg of suberic acid was added and dissolved in methanol in a 2 dram borosilicate vial at room temperature. After slow evaporation of the solvent block colorless crystals were obtained within one week

4.2.3.5 Synthesis of di- N-(3-ethynylphenyl)-6-7-dimethoxyquinazolin-4-aminedodecanedioic acid (A1$_2$:DOD)

To **A1** (10 mg), 3.7 mg of dodecanedioic acid was added and dissolved in methylenechloride in a 2-dram borosilicate vial at room temperature. After slow evaporation of the solvent block colorless crystals were obtained within one week.

Table 4-1 Melting points of the crystals and solvents used in crystallization experiments

Co-crystal/salt	Melting point (^{0}C)	Solvents used
$A1H^+:Cl^-$	255-260	Methanol/Water
$(A1)_2$: SUC	210-215	Methylenechloride/Ethylacetate
$(A1H)_2^+$: ADP^-:ADP.MeOH	175-180	Methanol
$(A1)_2$: SUB	190-195	Methanol
$(A1)_2$: DOD	185-190	Methylenechloride

4.2.4 Solubility studies

4.2.4.1 Large scale synthesis of co-crystals

Large scale synthesis of co-crystals for solubility studies were done via solvothermal method.[21] Supersaturation of **A1** and succinic acid was done by refluxing a mixture of succinic acid (90 mg, 0.82 mmol) and **A1** (0.50 g, 1.63 mmol) in 30 ml of methanol for 20 min. Immediate cooling to 0^{o}C resulted in a solid formation. The solid was filtered and dried. Co-crystals of **A1** and dodecanedioic acid and suberic acid were prepared by following the same procedure. Solids were analyzed via IR spectroscopy and PXRD to confirm the formation of co-crystals and the homogeneity of the crystals.

4.2.4.2 Solubility measurement of A1

Equilibrium solubility of **A1** was determined via a gravimetric method. A saturated solution of **A1** was prepared by dissolving 0.12 g of A1 in 10 mL of distilled water at room temperature. The vial was sealed and sonicated for 5 min to break any lump and stirred in a water bath. After stirring for 12 hrs at room temperature, the remaining solid was filtered and dried. Solubility was measured by the difference of initial and final weight of **A1**. The

experiment was carried out for 24 h, 48 h and 72 h to obtain the equilibrium solubility. After determining the optimum time period for the equilibrium solubility, a stock solution of **A1** was subjected to serial dilutions and their corresponding absorbance was recorded at 223 nm and plotted against concentration of **A1**. The equation of the line was used to determine the unknown concentrations of **A1** during co-crystallization experiments

4.2.4.3 Solubility measurement of co-crystals

A suspension of the co-crystal (0.5g) was dissolved in 10 ml of distilled water in a sealed vial and placed in a water bath to maintain a constant temperature. After stirring for 48 hrs, the remaining solid was filtered off. Absorbance of the resulting solution was measured at 223 nm using UV-Visible spectroscopy and required dilutions were carried out to obtain a suitable absorbance value. The absorbance values (y values) were used to calculate the corresponding concentrations (x) from the equation of line (y=mx+c) of the calibration curves. The calculated concentrations were multiplied by the dilution factor to obtain the actual concentration and thus the solubility of the co-crystals.

4.3 Results and discussion

4.3.1 Electrostatic potential value comparison of erlotinib and A1

It has been reported that electrostatic potential calculations on molecules with multiple acceptors and donors provide pathways for predicting binding preference in co-crystallization experiments,[22, 23] and in order to find and compare the binding preference of erlotinib and **A1** electrostatic potential values were calculated. Based on the electrostatic potential calculation, the sterically unhindered pyrimidyl nitrogen atom in both **A1** and erlotinib showed the highest negative electrostatic potential value and since the difference between calculated electrostatic potential values on other acceptor sites on **A1** and erlotinib are greater than 38 kJ/mol, the

sterically unhindered nitrogen atom can be considered as the best site for molecular recognition events.[23] Similarly, among the donor moieties the amine NH group in both **A1** and erlotinib showed the highest positive potential value and was regarded as the best site as a donor group. These results confirm that even with the changes in the length of the side chain in **A1**, the calculated electrostatic potential values are comparable with the erlotinib. (Figure 4-4)

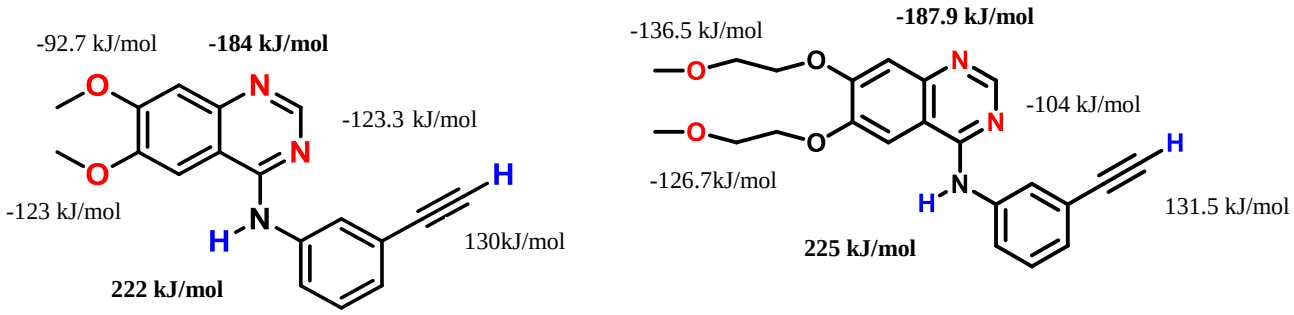

Figure 4-4 Calculated molecular electrostatic potential values on acceptor (red) and donor (blue) atoms on A1 (right) and erlotinib (left)

4.3.2 IR and PXRD data analysis of co-crystals

Analysis of **A1** with di-acids was initially carried out through IR spectroscopy. IR spectroscopy provides very reliable predictions for non-covalent interactions comparing the changes in the spectrum of co-crystals with the spectrums of the co-formers. Since we used carboxylic acids as donors, changes of the main functional groups are used to indicate positive results for co-crystal formation. With **A1** carboxylic acids could form O-H---N hydrogen-bond interaction and C=O----H-N interaction. The O-H---N hydrogen-bond interaction is mainly identified through a characteristic double hump which appeared in the 1800 cm^{-1}-2300 cm^{-1} region. N-H interaction with the carbonyl oxygen group can be easily identified through changes of the carbonyl stretch which usually appears in the 1650-1700 cm^{-1} region. Figure 4-5 shows one example of an IR spectrum of N-H---O interactions through double humps and shifts of the

carbonyl stretch due to C=O---H-N bond formation. Based In this study positive results were observed with succinic acid, adipic acid, suberic acid and dodecanedioic acid, but not with sebacic acid.

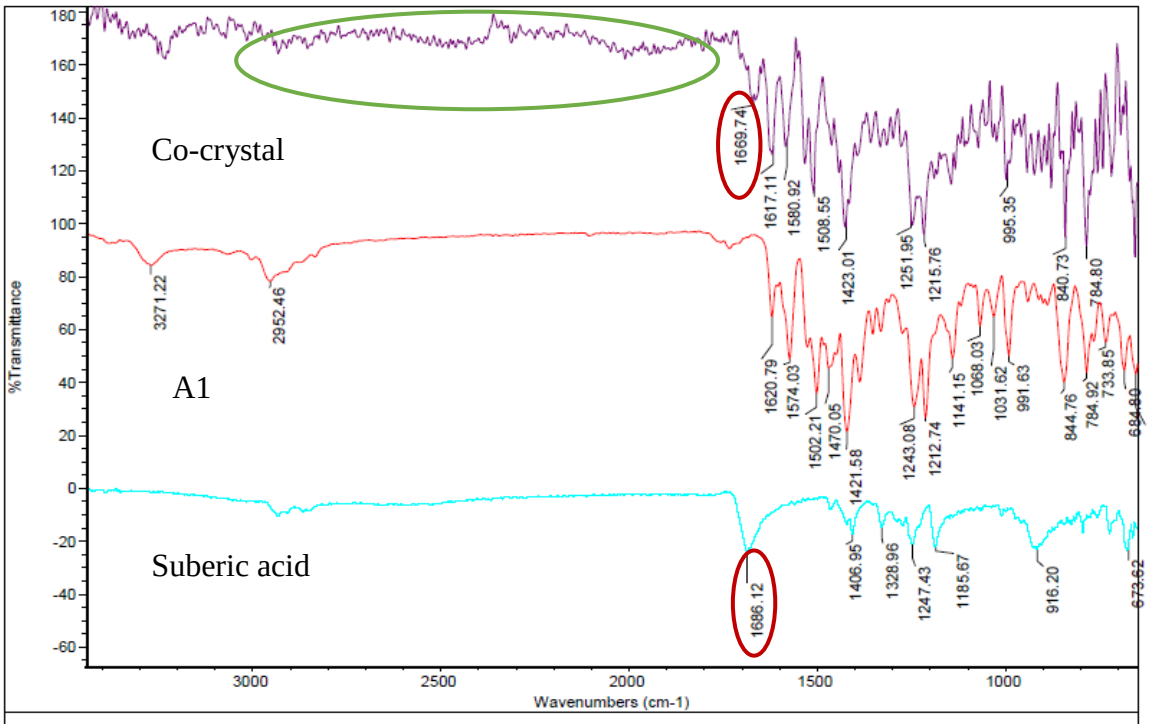

Figure 4-5 Positive results showing co-crystal formation through double humps (green circle) and carbonyl peak shift (red circle) on the IR spectrum

IR analysis was again used in initial screening of large scale co-crystal synthesis through the solvothermal method. In this method, the IR spectrum of the resulting solid was compared with the IR spectrum of the crystalline form of the co-crystal. Figure 4-6 shows two overlaid d IR spectrums of **(A1)$_2$:SUC.**

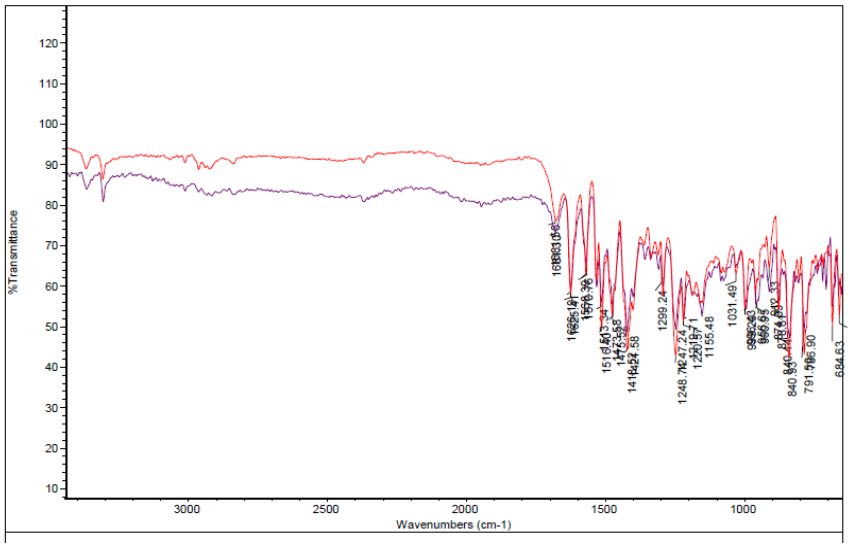

Figure 4-6 Comparison of the IR spectrums of the co-crystal of succinic acid (purple) and the solid obtained through solvothermal method (red).

Even though IR analysis is helpful for the initial screening of co-crystal formation; it does not provide any evidence of homogeneity of the co-crystal solids which is essential when carrying out the solubility experiments. In order to clarify the co-crystal formation through solvothermal methods a PXRD analysis was carried out. Having an excess of the highly soluble acid will provide inaccurate data in solubility studies. PXRD of the analyzed co-crystals (generated through Mercury software) was compared with the PXRD data of the co-crystal solids obtained through the solvothermal method. Having a matching spectrum, without any other extra peaks confirms the homogeneity of the co-crystal solids. Figure 4-7 shows a comparison of the stimulated and experimental powder pattern of **(A1)$_2$:DOD**.

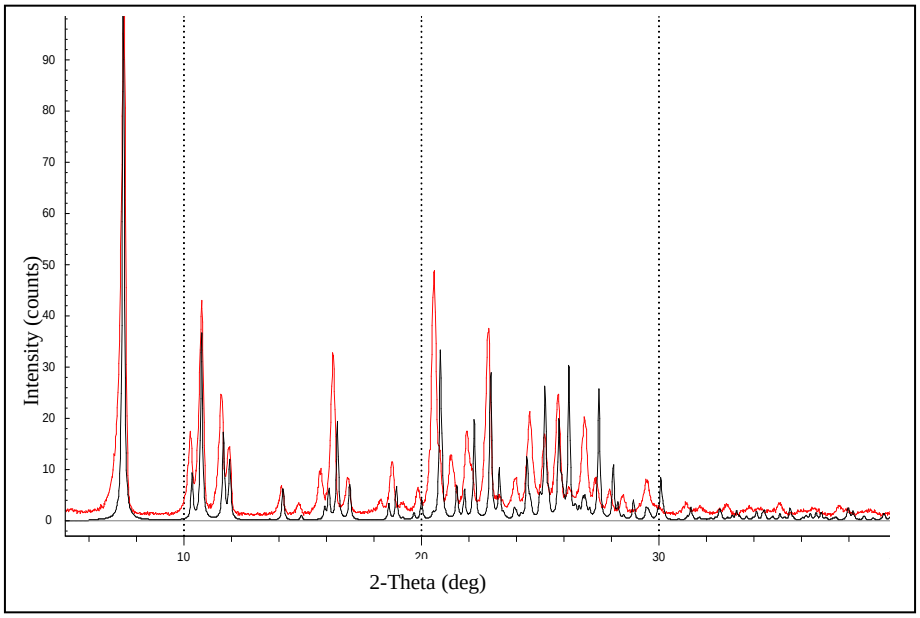

Figure 4-7 Stimulated (black) and experimental (Red) (solvothermal) powder pattern of $(A1)_2$:DOD

4.3.3 Structural outcomes of A1 with co-formers

4.3.3.1 Crystal structure of hydrochloride salts of erlotinib and A1

Since erlotinib is given in the form of hydrochloride salt we initially compared the crystal structure of the hydrochloride salt of the mimic with that of the structure of the chloride salt of erlotinib. In both cases, the proton is transferred to the less sterically hindered pyrimidine nitrogen atom (which has the largest negative electrostatic potential). (Figure 4-8) The primary hydrogen bonds in both structures are N-H (amine)---Cl^- and N-H^+(pym)---Cl^- hydrogen bonds and in both cases the supramolecular outcome is a hydrogen bonded 1-D architecture. The hydrogen bond distances and bond angles are very similar in both structures. Bond distance and angle of N-H^+---Cl^- is 3.066(2) Å and 169(2)^o for erlotinib and 3.0681(17) Å and 165^o for **A1** respectively. Similarly erlotinib and **A1** had N-H---Cl^- bond distance and angle of 3.277(2) Å and 167(2)^o, 3.2121(17)Å and 160^o, respectively. Considering these main structural similarities, we conclude that **A1** is an appropriate structural mimic of the native drug, despite the fact that

adjacent molecules within each structure are related by translation and two-fold screw axis, respectively.

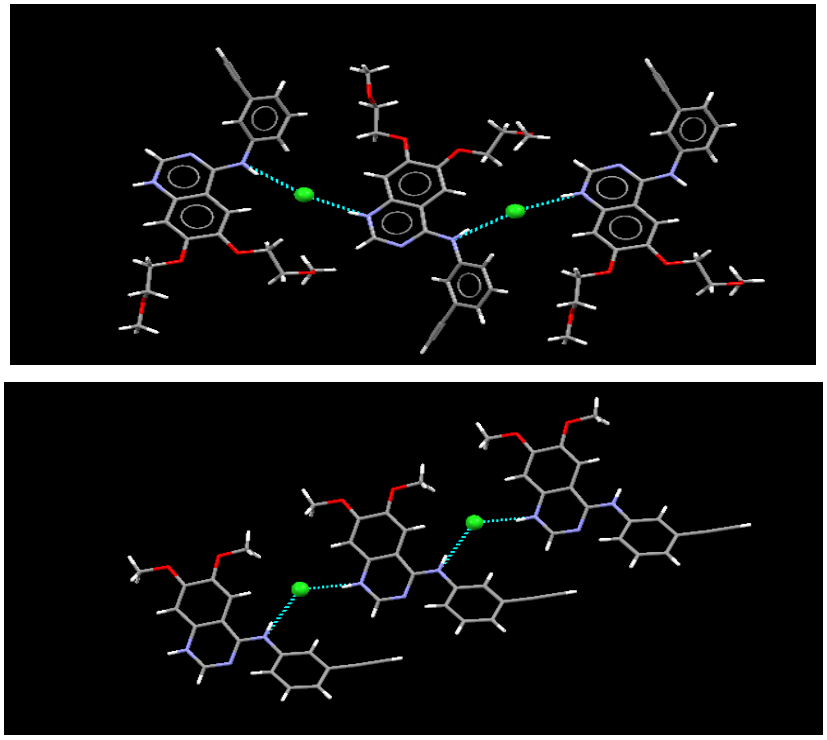

Figure 4-8 Primary interactions in the crystal structure of erlotinib hydrochloride (top) and in the crystal structure of $A1H^{+}:Cl^{-}$ (bottom)

4.3.3.2 Crystal structure of $(A1)_2$*:SUC*

The co-crystal of **A1** and succinic acid was obtained in a 2:1 ratio. The unhindered pyrimidyl N atom formed an N---H-O hydrogen-bond interaction with a O----N bond distance of 2.618(2) Å and 174(3)^{o} O-H---N bond angle. The secondary amine N-H formed an N-H---O short interaction with the carbonyl oxygen atom with N---O bond distance of 3.170(3) Å and N-H---O bond angle of 158.5(19)^{o} extending the structure into a 1-D chain (Figure 4-9. These chains were further extended to a 2-D network via π-π interactions between aromatic rings and the ethynyl (HC≡C–) group of two adjacent A1 molecules (Figure 4-10).

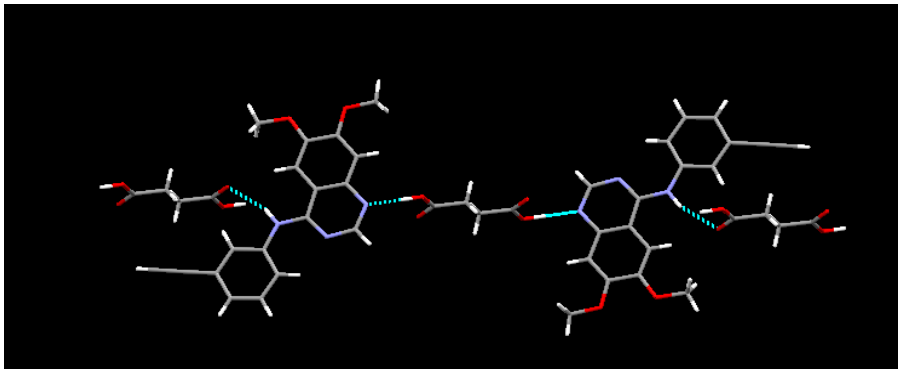

Figure 4-9 Primary O-H—N hydrogen-bond interaction and N-H---O short contacts in $(A1)_2$: SUC **crystal structure**

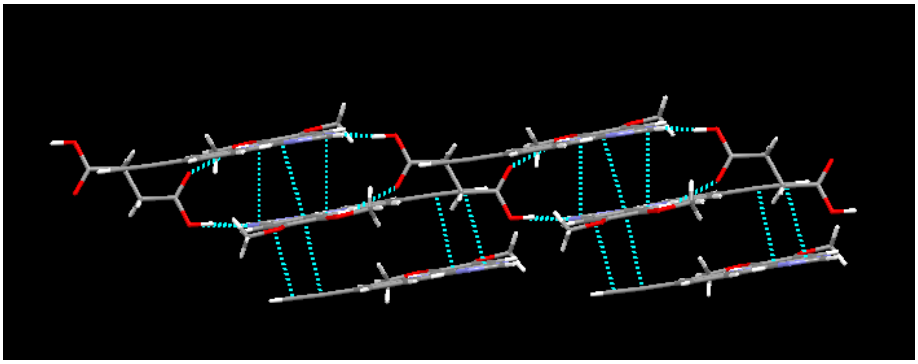

Figure 4-10 Extended 2-D network of $(A1)_2$: Succinic acid governed by π-π interactions between aromatic rings and the ethynyl (HC≡C–) group

4.3.3.3 Crystal structure of $(A1)_2$:SUB

The crystal structure showed a 1:2 stoichiometry between suberic acid and **A1** (Figure 4-11). Similar to the $(A1)_2$:SUC co-crystal, the sterically unhindered pyrimidyl N atom formed O-H---N interactions d(O---N) 2.584(3)Å and (O-H---N) angle 174(3)°. The amine N-H group formed a N-H---O interaction with d(N---O) 2.804(3) Å and N-H---O angle 168(2)°. This arrangement leads to an extended 1-D architecture with repeating nodes of $R^4_4(20)$ tetramer (Figure 4-11 and 4-12).

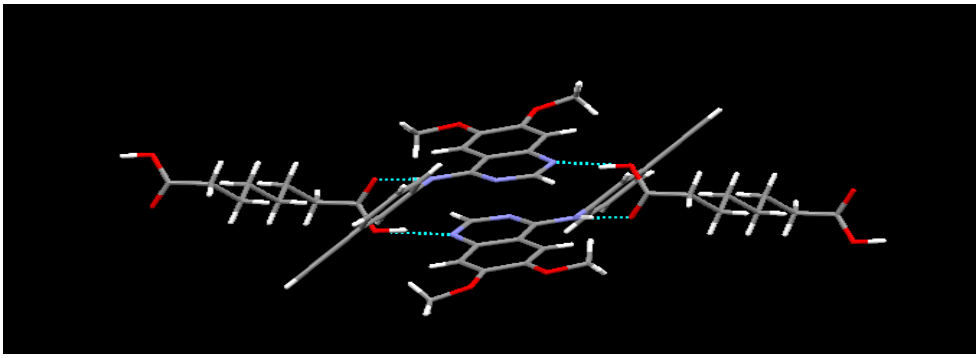

Figure 4-11 O-H---N and N-H---O hydrogen- bond interaction between A1 **and suberic acid which leads to a tetramer formation**

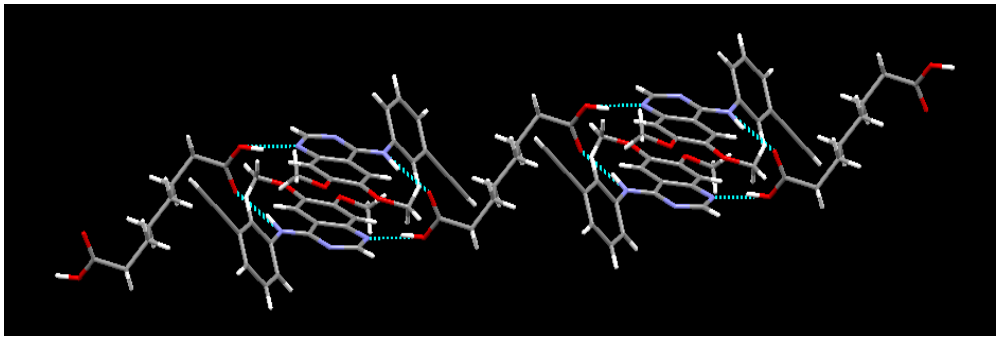

Figure 4-12 Extended 1-D network of $(A1)_2$:SUB **with repeating tetramer nodes.**

4.3.3.4 Crystal structure of $(A1)_2$:DOD

The crystal structure with dodecanedioic acid showed a 1:2 stoichiometry with the acid and **A1** molecule. With close similarity to the crystal structure of **$(EM)_2$:SUB,** an $R^4_4(20)$ tetramer was formed between the pyrimidyl N, the carboxylic acid group the and amine N-H moiety.The O-H----N hydrogen bond was formed with O---N distance of 2.592(3) Å and O-H----N angle of 177(4)^o and N-H---O interaction with N----O distance of 2.999(3) Å and N-H---O angle of 160(3)^o and these interactions give rise to infinite 1-D chains (Figure 4-13). Adjacent 1-D chains were interconnected via C-H---π and π-π interactions (Figure 4-14). Again, the best hydrogen-bond acceptor on **A1** was the preferred binding site for the carboxylic acid O-H moiety.

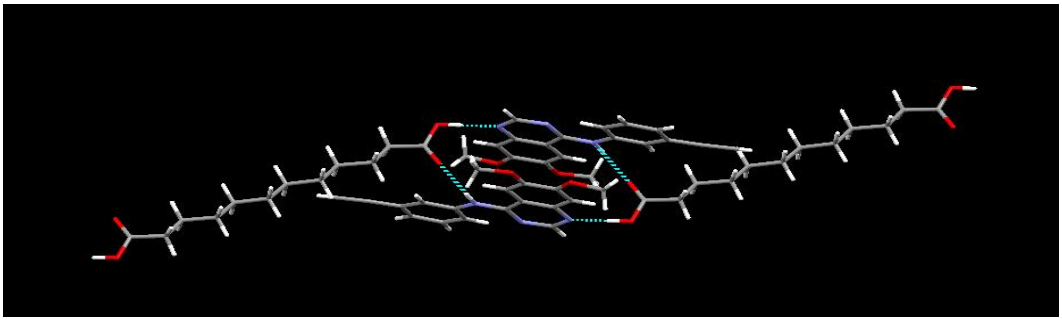

Figure 4-13 Hydrogen bonds formed by dodecanedioic acid with sterically unhindered N and amine NH moiety in the $(A1)_2$:DOD **co-crystal**

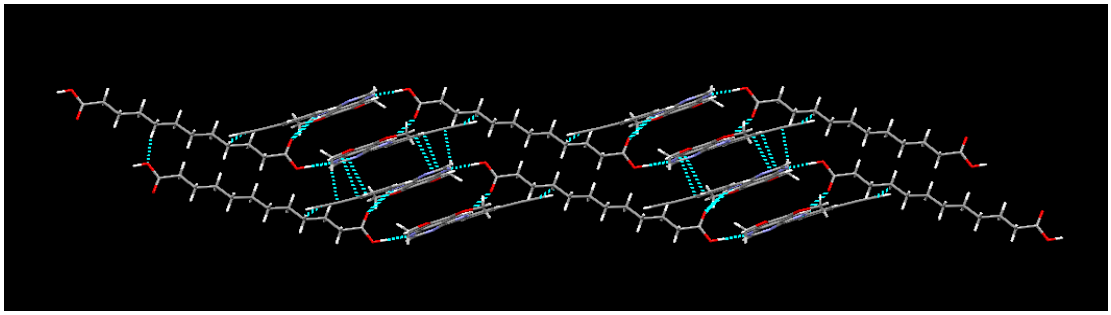

Figure 4-14 Extended 2-D network governed by C-H---Π and Π-Π interactions in $(A1)_2$:DOD **crystal structure**

4.3.3.5 Crystal packing of $(A1H^+)_2$:ADP^-:ADP.MeOH

The crystal structure of **A1** with adipic acid was different compared to the previous three co-crystal structures. We observed proton transfer to the unhindered pyrimidyl N forming $N\text{-}H^+$---$^-O\text{-}C$ ionic interaction. In the asymmetric unit, we observed the presence of two conformations of **A1** (anti) (A) and syn (B) arrangement with respect to the position of amine NH group (due to the rotation of N-(3-ethynyl) moiety) (Figure 4-15).

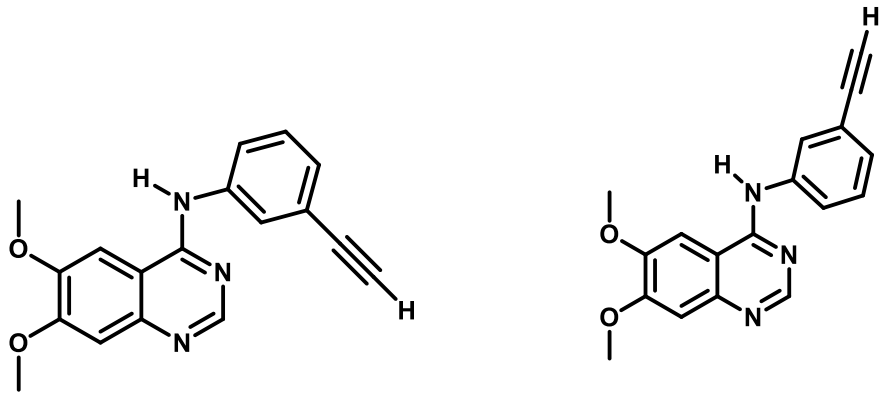

A B

Figure 4-15 Two conformations of A1 **(A: anti , B: syn) formed due the flexibility of N-(3-ethynyl) moiety**

In the crystal structure, adipate anion showed a difference in forming hydrogen-bond interactions. One carboxyl end of the acid formed N-H^+----$^-$O-C interactions with **A1** molecule (syn) which extended 1-D along the b axis. (N---O bond length 2.717(4)Å and N-H---O angle 175(4)^o). The carbonyl oxygen group from adipate anion forms another C=O---H-O hydrogen-bond interaction with a free adipic acid creating a 2-D network (O---O bond distance 2.592(4) Å and O-H---O angle 170(5)^o). From the other carboxylate end, the carbonyl oxygen atom forms a C=O---H-O interaction (O---O bond distance 2.770(4) Å and O-H---O angle 148(4)^o) with solvent methanol and a C=O---N-H interaction (N---O bond length 2.908(4) Å and N-H---O angle 164(3)^o) with NH amine group of **A1** (syn). Also the N-H^+ pyrimidyl group of **A1** (anti) formed a N-H^+----$^-$O-C interaction with N---O bond length 2.599(4) Å and N-H---O angle of 164(3)^o. The N-H amine group in **A1** (anti) formed a N-H---O interaction to free adipic acid with N---O bond length of 2.863(4) Å and N-H---O angle of 159(3)^o (Figure 4-16).

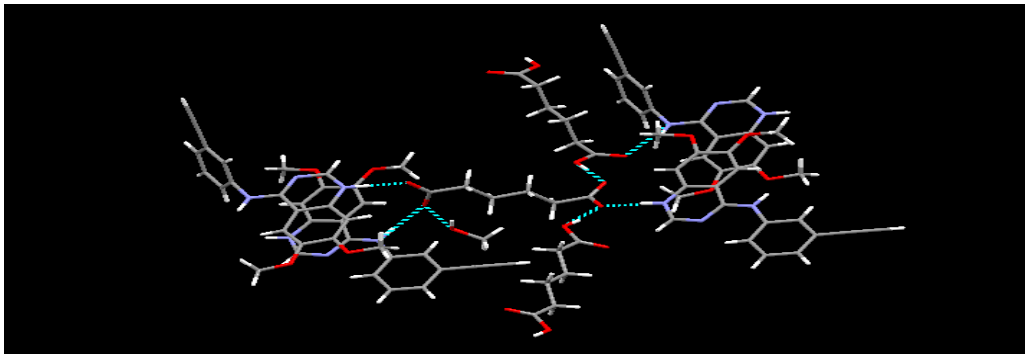

Figure 4-16 Difference in hydrogen-bond interactions with respect to the conformation of A1 **and ADP/ADP$^-$ acids.**

4.3.4 Solubility studies of A1 and co-crystals

The solubility of **A1** and its respective co-crystals were measured using an undersaturated solution. Equilibrium solubility of **A1** was measured in different time intervals to obtain the maximum solubility (12 h, 24 h, 48 h, and 72 h). Based on the solubility data maximum solubility was obtained after 48 h of stirring in a water bath at room temperature (Table 4-2).

Table 4-2 Concentration of A1 **as a function of time**

Time	Solubility (mg/mL)
12 h	0.11
24 h	0.12
48 h	0.19
72 h	0.17

Data obtained after 48 hrs is used for the standard calibration curve which was determined using UV-Vis spectrometry at 223 nm to determine unknown concentrations of **A1** (Figure 4-17).

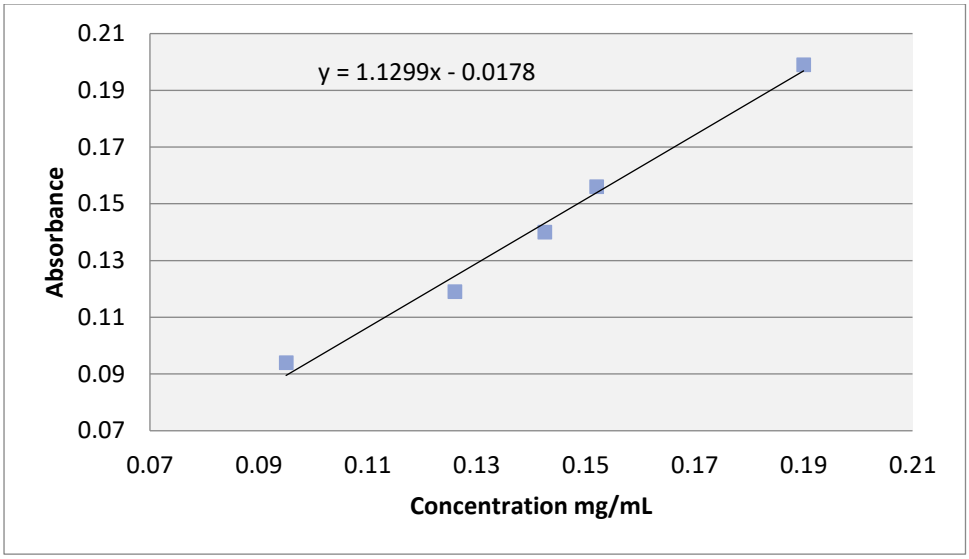

Figure 4-17 Absorbance vs the concentration of A1

After obtaining the equation of line using the calibration curve, data was used to calculate the concentrations (solubility) of co-crystals. Since the dissolution reached eqilibrium after 48 hrs, solubility measurements of co-crystals also were carried out for 48 hrs. Table 4-3 shows the solubility data of co-crystals and Figure 4-18 shows the bar graph which highlights the changes of solubility with respect to type of the co-former used.

Table 4-3 Solubility data of A1 and its co-crystals after 48 h

Compound	Solubility (mg/mL)
A1	0.19
$(A1)_2$:SUC	3.60
$(A1H^+)_2$:ADP-:ADP.MeOH	2.15
$(A1)_2$:SUB	1.05
$(A1)_2$:DOD	1.27

.

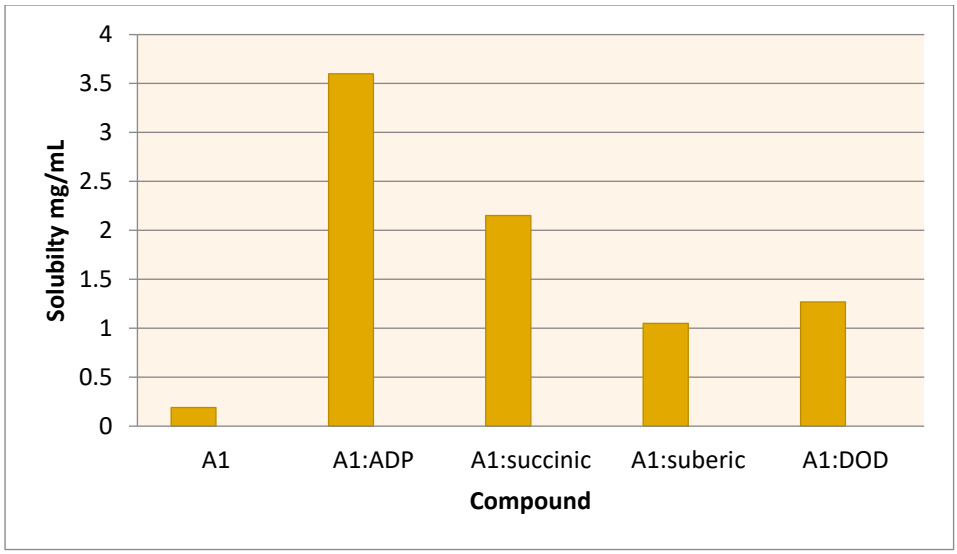

Figure 4-18 Aqueous equilibrium solubility of A1 and the co-crystals of A1

Based on the solubility data it indicates that the solubility of the co-crystals of **A1** is increased with compared to the solubility of **A1**. $(A1)_2$:SUC showed 20 fold increases in the solubility and $(A1)_2$:SUB and dodecanedioic co-crystals showed ~ ten fold increase in the solubility. However even though $(A1H^+)_2$:ADP-:ADP.MeOH showed the highest solubility we were not too surprised by the data since we expect to have increase of solubility of salts/solvates. This data might be subjected to change with the changes of solvent molecules in the crystal structure of $(A1H^+)_2$:ADP^-:ADP.MeOH. However, solubility data of co-crystals are more reliable since the structural outcomes are not subjected to change in the presence of similar experimental conditions. Our results indicate the potential of co-crystallization as a tool for modifying the solubility of an organic molecular solid.

4.3.5 Correlation between and melting point of co-crystals and the melting point of the co-former

The melting point is considered as an important physical property in pharmaceutical industry. Generally, the solubility equation is used in pharmacy to determine the aqueous

solubility of solutes. The melting point and partition co-efficients of solutes are the main two factors taken in to account in the equation. For single component systems it is straightforward to make predictions whereas in literature very little information is found in correlating melting points of co-crystals with co-formers used. With this in mind the thermal behavior of the co-crystals with relation to the corresponding diacids were measured to observe any correlation between the melting points and co-formers. The data showed that the melting points of the three co-crystals are directly related to the melting points of the corresponding dicarboxylic acid. The highest melting co-crystal contains the dicarboxylic acid with the highest melting point and the lowest melting point was observed with lowest melting dicarboxylic acid. (Melting point of the **A1**:adipate salt showed no relation to the melting point of the acid or **A1**) (Figure 4-19). Therefore, these data suggests that by modulating the properties of the components in a co-crystal solid we can easily regulate the properties of molecular solids.

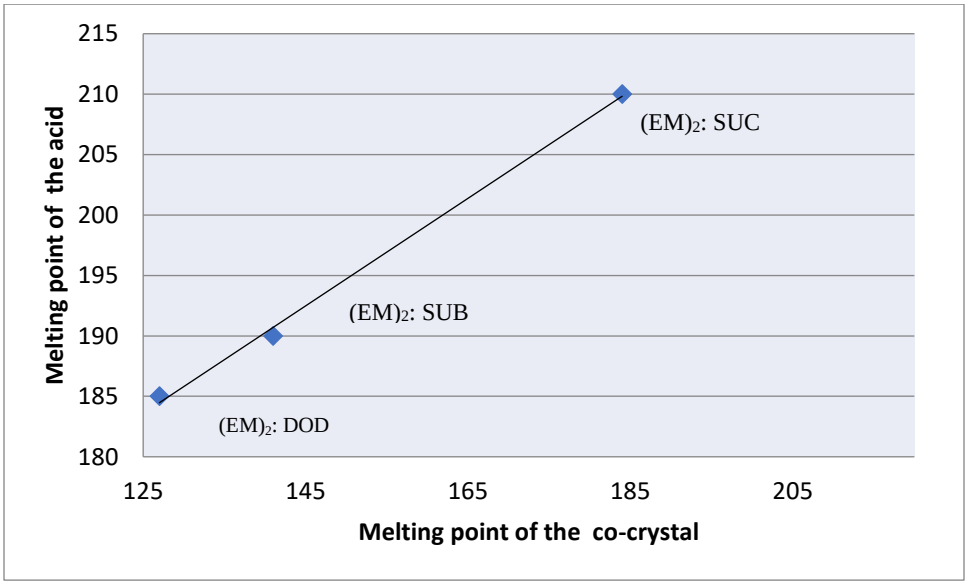

Figure 4-19 Melting points of co-crystals (Y) vs the melting points of corresponding di acids (X)

4.4 Conclusion

In this study, we use the concept of structural mimics to indirectly examine the structural landscape of poorly soluble solids. A structural mimic to erlotinib (**A1**) was synthesized maintaining all the binding sites which are important in constructing structural landscapes. Initial electrostatic potential calculations of the mimic and the erlotinib showed that the sterically unhindered pyrimidyl nitrogen and the amine N-H moiety in both molecules have the highest potential to participate in non-covalent interactions. This observation revealed that even with the structural changes we made to the mimic it was able to maintain the binding potentials of both acceptors and donors and has very good structural similarity to the actual drug erlotinib. Out of five crystallization experiments with highly soluble, even-chain dicarboxylic acids, three produced co-crystals whereas sebacic acid did not and adipic acid formed an $(A1H)_2^+$: adipate co-crystal salt. The intermolecular interactions observed in the series of co-crystals showed consistency and in all the structures, the best acceptor site (the pyrimidyl nitrogen atom with the largest negative electrostatic potential) formed hydrogen bonds with the –O-H group of the acid (the best donor site). By analyzing the CSD database for erlotinib nine hits were found and with the comparison of the structural outcomes of the mimic it was evident that the main interactions present in the actual drug and the mimic can be related (Figure 4-20).

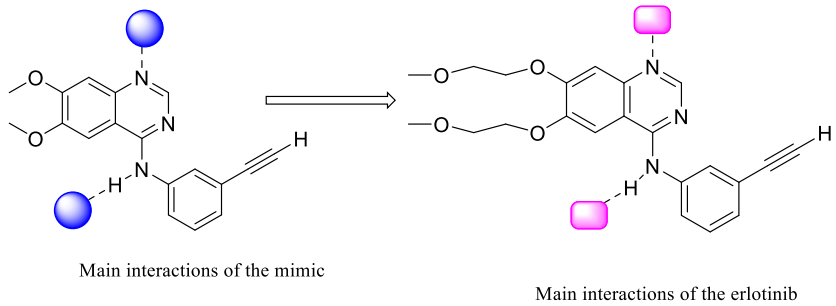

Figure 4-20 Comparisons of the structural outcomes of the mimic (EM) and erlotinib

Solubility and thermal analysis showed that with the systematic changes of co-crystallization agent it is possible to make predictable changes to physical properties. This study is a good example which shows that usage of structural mimics will provide benefits in exploring structural landscapes of poorly soluble APIs and can be used to dial-in physical properties.

4.5 References

1. Sabine Vogler, Nina Zimmermann, Claudia Habl, *GABI Journal*, 2013, **2**, 178-187.
2. O. Almarsson and M. J. Zaworotko, *Chem. Commun.*, 2004, 1889-1896.
3. R. Sanghvi, R. Narazaki, S. G. Machatha and S. H. Yalkowsky, *AAPS PharmSciTech*, 2008, **9**, 366-376; G. L. Amidon, H. Lennernäs, V. P. Shah and J. R. Crison, *Pharm. Res.* 1995, **12**, 413-420.
4. E. Merisko-Liversidge, G. G. Liversidge and E. R. Cooper, *European Journal of Pharmaceutical Sciences*, 2003, **18**, 113-120; B. Sajeev Kumar, R. Saraswathi, K. Venkates Kumar, S. K. Jha, D. P. Venkates and S. A. Dhanaraj, *Drug Delivery*, 2014, **21**, 173-184; M. Otsuka, Y. Maeno, T. Fukami, M. Inoue, T. Tagami and T. Ozeki, *European Journal of Pharmaceutics and Biopharmaceutics*, 2016, **108**, 25-31; S. V. Patel and S. Patel, *Eur. J. Pharm. Sci.*, 2015, **77**, 161-169.
5. A. K. Nair, O. Anand, N. Chun, D. P. Conner, M. U. Mehta, D. T. Nhu, J. E. Polli, L. X. Yu and B. M. Davit, *The AAPS Journal*, 2012, **14**, 664-666.
6. *FDA classification,*2013.
7. A. D. Bond, *CrystEngComm*, 2007, **9**, 833-834.
8. P. Vishweshwar, J. A. McMahon, J. A. Bis and M. J. Zaworotko, *J. Pharm. Sci.*, 2006, **95**, 499-516.

9. A. Moghimi, H. R. Khavasi, F. Dashtestani, D. Kordestani, E. Behboodi and B. Maddah, *J. Struct. Chem.*, 2013, **54**, 990-995.

10. J. W. Steed, *Trends in Pharmacol. Sci.*, 2013, **34**, 185-193.

11. D. Hasa, G. Schneider Rauber, D. Voinovich and W. Jones, *Angew. Chem. Int. Ed.*, 2015, **54**, 7371-7375.

12. A. Mukherjee, S. Tothadi, S. Chakraborty, S. Ganguly and G. R. Desiraju, *CrystEngComm*, 2013, **15**, 4640-4654.

13. M. A. Elbagerma, H. G. M. Edwards, T. Munshi, M. D. Hargreaves, P. Matousek and I. J. Scowen, *Cryst. Growth Des.*, 2010, **10**, 2360-2371.

14. C. B. Aakeröy and D. J. Salmon, *CrystEngComm*, 2005, **7**, 439-448; C. B. Aakeröy, S. Forbes and J. Desper, *CrystEngComm*, 2014, **16**, 5870-5877.

15. T. L. Petty, *J.Clin.Oncol.*, 2003, **1**, 34.

16. M. Scheffler, Di Gion, P. ,Doroshyenko,O.,Wolf,J. and Fuhr,U., *Clin.Pharmacokinet*, 2011, **50**, 371.

17. P. Sanphui, L. Rajput, S. P. Gopi and G. R. Desiraju, *Acta Crystallogr. Sec. B*, 2016, **72**, 291-300.

18. K.-C. P. Kuen-Feng Chen, Jung-Chen Su,Yi-Chieh Chou,Chun-Yu-Liu,Hui-Ju-Chen,Jui-Wen Huang,InKi Kim,Chun-Wai Shiau, *bioorg.Med.Chem.*, 2012, **20**, 6144.

19. R.C.Schnur, L.D.Arnold, *Quinazoline derivatives*, Google patents.

20. C. B. Aakeroy, S. Panikkattu, P. D. Chopade and J. Desper, *CrystEngComm*, 2013, **15**, 3125-3136.

21. L. Duan, S. Jia and L. Zhao, *Eur. J. Inorg. Chem.*, 2010, **2010**, 1957-1962.

22. C. B. Aakeröy, T. K. Wijethunga and J. Desper, *New J. Chem.*, 2015, **39**, 822-828; C. B. Aakeröy and K. Epa, *Top. Curr. Chem.*, 2014, **351**, 125-147.

23. M. D. Perera, J. Desper, A. S. Sinha and C. B. Aakeroy, *CrystEngComm*, 2016, **18**, 8631-8636.

Chapter 5 - Energetic co-crystals of 5,7-dinitrobenzotriazole with enhanced chemical stability

5.1 Introduction

5.1.1 Background

Developing energetic materials with higher performance and decreased sensitivity is a demanding area in both military and commercial applications.[1] Apart from traditional nitro-containing materials like TNT, RDX,[2] and HMX[3], studies of heterocyclic compounds as energetic materials have expanded due to their high positive heats of formation and environmental compatibility.[4] Among these heterocyclic compounds, nitro-substituted imidazole,[5] triazole,[6] tetrazole[7] and pyrazole[8] have shown promise as potential energetic materials and are currently under development.[9] [5, 10] However, when an electron withdrawing nitro group is attached, a heterocyclic N-H proton can become very acidic which may cause problems with respect to long-term storage and handling. (Figure 5-1) One approach to obtain a better energetic material is to design a completely new molecule without any acidic protons, or a salt. However, optimizing the explosive properties like high power, low sensitivity and low reactivity in a finite time scale is challenging, and most of the time power and sensitivity appear to be contradictory in synthesis. [11]

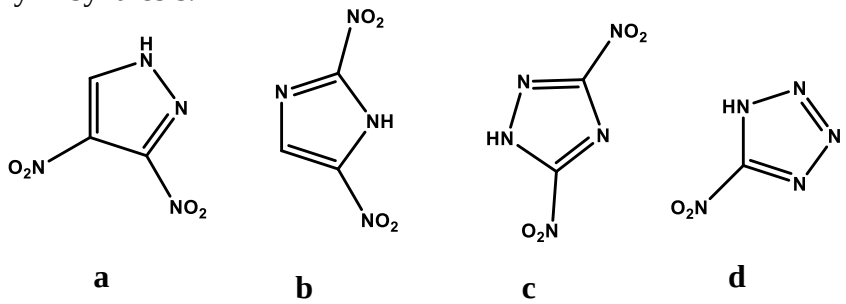

Figure 5-1 Commonly used nitro- containing heterocycles (a**) pyrazole (**b**) imidazole (**c**) triazole (**d**) tetrazole with acidic N-H protons**

An alternative approach is to use co-crystallization technology, where a known energetic material can be combined with another energetic or non-energetic material via non-covalent interactions.[12] Co-crystallization is a very beneficial technique for improving performance and other chemical and physical properties of energetic materials as it does not require new chemical synthesis. Co-crystals of TNT, HMX and CL-20 have shown the ability for fine tuning of their properties and performance through co-crystallization.[13] However, designing novel energetic co-crystals is still in its early stage and most of the reported examples are based on improving impact/friction sensitivity.[14] To date, there is only one example which shows that co-crystallization technology can be successfully used to improve chemical stability of energetic materials. In that study, acidic protons of EDNA were successfully suppressed by adding supramolecular protecting groups, and a higher chemical stability was obtained[15] (Figure 5-2).

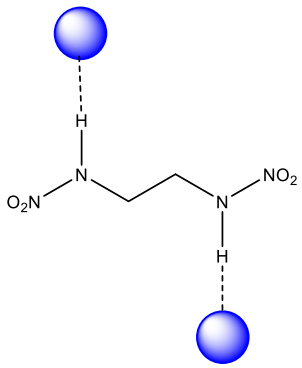

Figure 5-2 Addition of supramolecular protecting groups to the acidic protons of EDNA to suppress the chemical reactivity.[15]

5.1.2 5,7-Dinitrobenzotriazole as an energetic material

Among the heterocyclic nitrogen-rich energetic materials, 1, 2, 3-triazoles are promising candidates due to the presence of N-N, C-N bonds and ring strain.[16,17] In a recent study, Klapötke and co-workers investigated the explosive performance and sensitivity of 5,7-dinitrobenzotriazole (**DBT**), its salts and derivatives of **DBT**, and found them to be energetic

materials.[18] However, the N-H protons are acidic and limit their use as effective explosive materials. The crystal structure of **DBT** by itself shows[19] that the N-H protons form N-H---N hydrogen-bond interactions with one of the triazole nitrogen atoms in the heterocycle. However, this interaction is not strong enough to reduce the acidity of the molecule. Therefore, through co-crystallization technology, molecules which are capable of forming strong N-H---N or N-H---O interactions may be introduced to break (Figure 5-3) this weak self-interaction, and new molecules with altered performance, chemical and thermal stability and sensitivity can be synthesized.

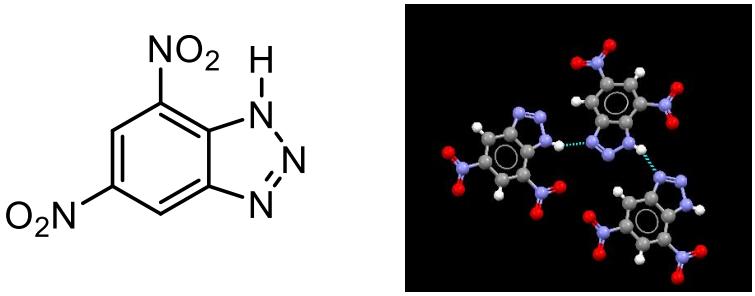

Figure 5-3 DBT molecule (left) and part of the crystal structure of DBT showing N-H---N hydrogen bonds (right)[19]

5.1.3 Goals of the study

In our study, we hope to answer the following questions;

- What are the intermolecular binding preferences of DBT with different nitrogen and oxygen containing acceptor molecules?
- Can we alter the performance and thermal stability of DBT by changing the acceptor molecule?
- Can we improve the chemical stability by suppressing the reactivity of acidic N-H proton in DBT?

In order to achieve our goals, fifteen acceptor molecules containing nitrogen and oxygen atoms as acceptors were selected as co-crystallizing agents (Figure 5-4).

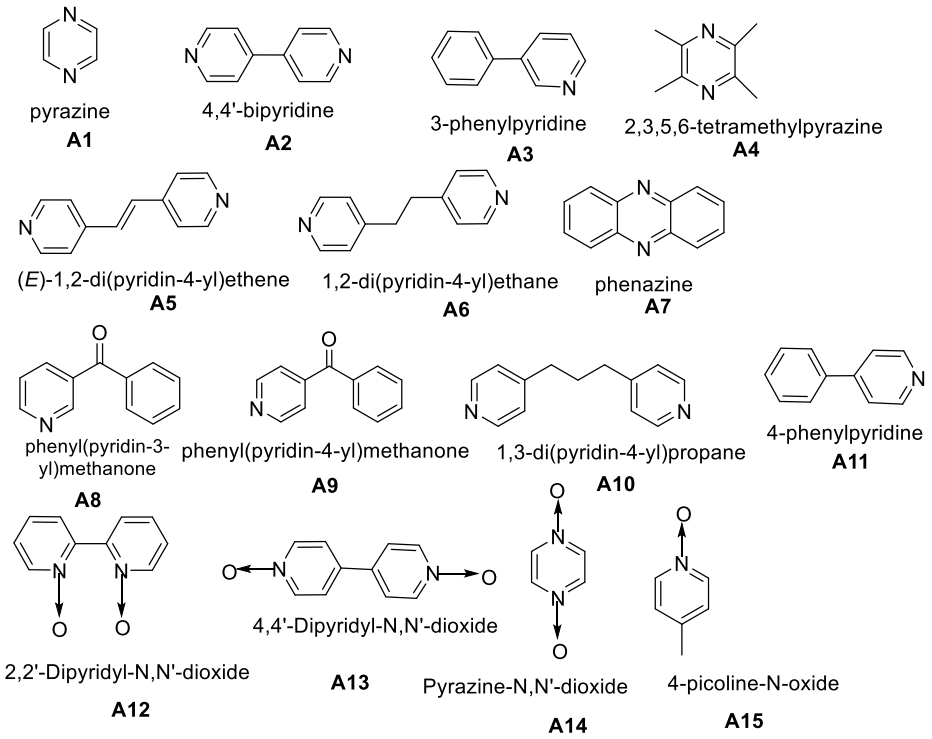

Figure 5-4 Nitrogen and oxygen containing acceptors used for the co-crystallization experiments

5.2 Experimental

Although we did not experience any problems in handling and synthesis, DBT is an energetic material and should be handled with extreme care. All the synthesis was performed inside a fume hood and used nonmetallic spatulas for measuring DBT. Kevlar gloves, lab coat and goggles were worn all the time. Synthesis was only performed on a small scale (~200 mg). Benzotriazole and co-formers were purchased via commercial sources and used without further purification. ^{1}H NMR spectra were recorded on a Varian Unity plus 400 MHz spectrophotometer in $CDCl_3$. IR spectra were recorded out on a Nicolet 380 FT-IR. Melting points were determined on a Fisher-Johns melting point apparatus. Decomposition points were measured on a DSC Q20 and electrostatic potential calculations were carried out using Spartan 08' software.

5.2.1 Synthesis of 5,7-dinitrobenzotriazole[18, 19]

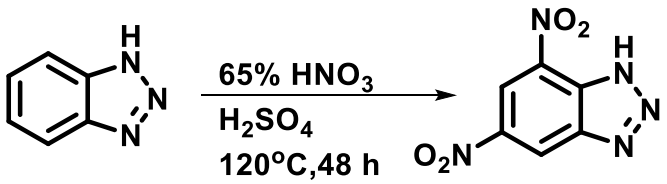

^{1}H-Benzotriazole (100 mg, 0.830 mmol) was dissolved in 96% sulfuric acid (1.22 ml) at 0^{o}C and 65 % nitric acid (1.27 ml) was then added drop wise. The mixture was stirred vigorously for 15 min at 0^{o}C and heated to 120^{o}C for 48 h. The solution was cooled and poured into 5 ml of crushed ice. The precipitate was filtered and washed with cold water. A colorless solid was obtained in 40% yield. (M.p196^{o}C Dec.point 291^{0}C, reported M.p193^{o}C[19] Dec.point 291^{o}C) ^{1}HNMR (δH,400 MHZ, DMSO-d_6,) δ 8.99 (s 1 H,) 9.55 (s 1H) 9.03 (s 1H).

5.2.2 Synthesis of co-crystals

For initial co-crystal screening, acceptors which contain symmetric and asymmetric pyridyl nitrogen groups and N-oxides were used. (Figure 5-4) DBT and the co-formers were mixed according to the stoichiometric ratio and dissolved in a minimum amount of solvent and subjected to slow evaporation. Once suitable X-ray quality crystals were obtained IR analysis and DSC analysis were done to confirm co-crystal formation. IR confirmation was done by analyzing the presence of peaks from both co-formers and the peak shifting with respect to the spectrum of acceptor and donor molecules. Once the formation of co-crystal was confirmed, crystals were submitted for X-ray crystallography. Out of fifteen experiments, four experiments produced X-ray quality crystals (Table 5-1).

Table 5-1 Synthesis of DBT co-crystals

Co-crystal	Abbreviation	Mole ratio	Solvent and method
DBT:Phenazine	$(DBT)_2$:A7	2:1	Ethylacetate/methanol Slow evaporation
DBT:4,4-Dipyridyl	$(DBT)_2$:A2	2:1	Methanol/THF Slow evaporation
DBT:1,2(Dipyridin-4-yl)ethylene	$(DBT)_2^-$:$A5^+$	2:1	Methanol Slow evaporation
DBT:4-Phenylpyridine	DBT:A11	1:1	Methanol Slow evaporation

5.2.3 Impact sensitivity studies[20]

Impact sensitivities of DBT, $(DBT)_2$:A7 and $(DBT)_2$:A11 were measured using impact drop testing. Tests were performed in an apparatus designed to accommodate small amounts of material and was calibrated against tetranitromethane (H_{50}=38 cm). Approximately 0.1 mg of each sample was measured in to an aluminum DSC pan and a freefalling 5 lb weight was used to strike the sample from different heights (Figure 5-5). Values were measured in centimeters and the H_{50} value was recorded (the height at which the material has a 50% chance of detonation).[21] This can only be used for relative comparison only.

Figure 5-5 Apparatus with 5 lb weight used to measure impact sensitivity of samples

5.3 Results and discussion

5.3.1 Analysis of co-crystals through IR spectroscopy

DBT contains two triazole nitrogen atoms which are capable of forming hydrogen bonds with suitable donors like carboxylic acid or phenols and one N-H moiety which is capable of acting as a hydrogen bond donor in the presence of suitable acceptors. In this study, we focused on the triazole N-H group which leads to chemical instability. Therefore, with the acceptors we chose we would expect to get new N-H---N or N-H---O hydrogen- bond interactions. We did not perform any grinding experiment with the co-formers since DBT is an energetic material, but instead analyzed the solid/crystal formed after slow evaporation method through IR spectroscopy to confirm the co-crystal formation before submitting to X-ray crystallography. In the IR spectra, we mainly focused on a few prominent peaks of DBT. N-H bending appeared around 1641 cm^{-1} and two bands for $–NO_2$ stretching appeared at 1535 cm^{-1} and 1338 cm^{-1}. Since the N-H group and the NO_2 group can form hydrogen bonds we would expect to have changes in these peaks.[22] One example of a co-crystal which reveals significant shifting of N-H bending from 1641 cm^{-1}-1688 cm^{-1} is shown in Figure 5-6. Shifting of the N-H bending suggests hydrogen-bond

formation between the corresponding acceptor and donor sites, little change of the nitro group implies that there is no significant hydrogen- bond formation between the nitro group and N-H protons.

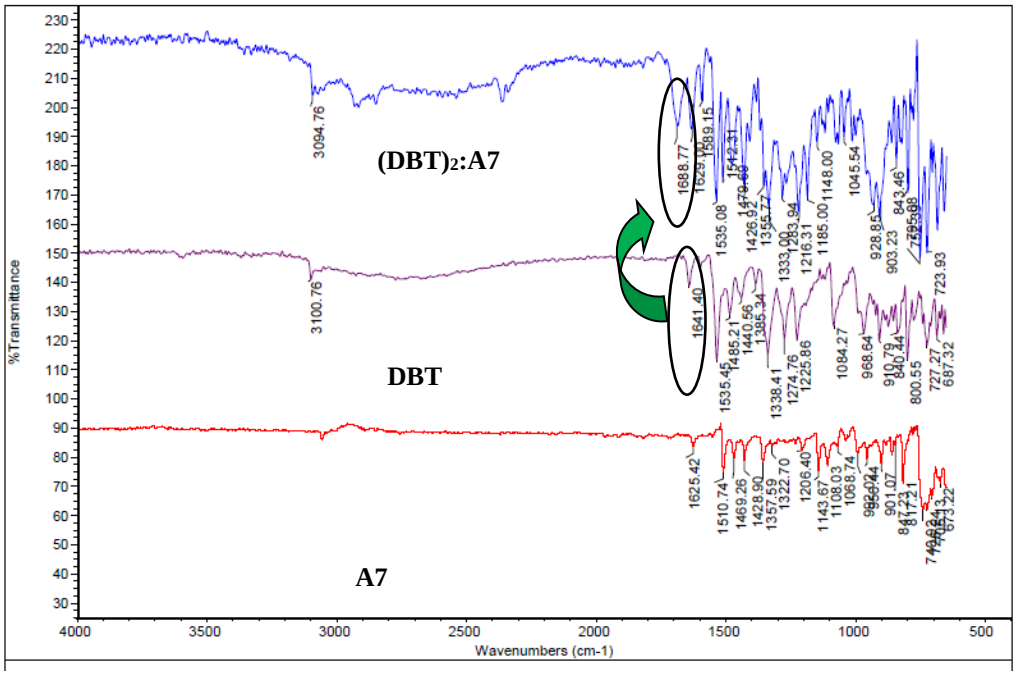

Figure 5-6 IR spectrum comparison of (DBT)$_2$:A7 with DBT and A7 (black circles indicate the shifting of N-H bending of DBT upon co-crystallization)

Based on the IR analysis all fifteen experiments resulted in co-crystal formation. Four of them yielded X-ray quality crystals (Table 5-2).

Table 5-2 IR modes of DBT and solids/crystals obtained after slow evaporation

Compound	-N-H bending (cm^{-1})	-NO_2 stretching (cm^{-1})	Co-crystal (Y/N)
DBT	1641	1535, 1338	-
DBT:A1	1633	1535,1341	Y
DBT:A2	1629	1527,1335	Y
DBT:A3	1636	1535,1341	Y

DBT:A4	1629	1537,1344	Y
DBT:A5	1611	1507,1326	Y
DBT:A6	1636	1535,1340	Y
DBT:A7	1635	1535,1341	Y
DBT:A8	1651	1531,1339	Y
DBT:A9	1649	1532,1339	Y
DBT:A10	1635	1535,1340	Y
DBT:A11	1634	1535,1341	Y
DBT:A12	1654	1537,1352	Y
DBT:A13	1632	1534,1339	Y
DBT:A14	1650	1535,1339	Y
DBT:A15	1628	1534,1338	Y

5.3.2 Structural analysis of the co-crystals

Even though IR spectroscopy provides evidence for co-crystal formation, it does not provide details about the binding preferences of molecules in the presence of different co-formers. However, by looking at the binding moieties of the molecule we can make predictions about the structural outcome using theoretical calculations. These structural predictions can then be validated through X-ray structural analysis.

5.3.2.1 Electrostatic potential calculations

In DBT the N-H group acts as a donor site and a triazole nitrogen atom and nitro group act as potential acceptor sites (Figure 5-7). Based on electrostatic potential calculations of DBT and the acceptor molecules (**A7**, **A2**, **A5** and **A11**) it is evident that the N-H moiety has a higher

binding preference for the acceptor sites of the co-formers than the acceptor sites of the DBT by itself, (Table 5-3) therefore self N-H---N interactions of DBT can be broken and new N-H---N hydrogen bonds can be formed with the new acceptors (Figure 5-8).

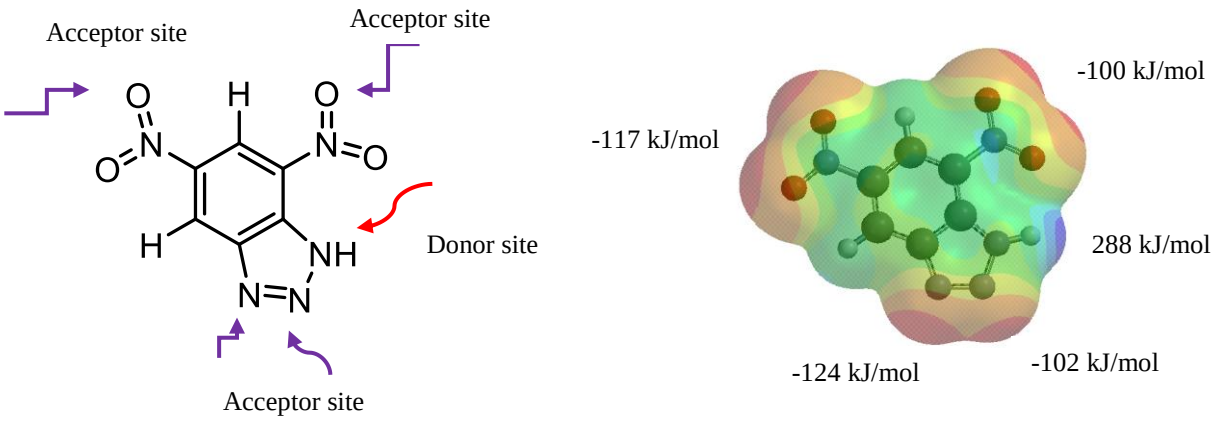

Figure 5-7 Potential acceptor/donor sites of DBT (left) and calculated electrostatic potential values (right)

Table 5-3 Electrostatic potential values of the acceptors

Acceptor	Calculated electrostatic potential values
A7	-152.3 kJ/mol
A2	-177.2 kJ/mol
A5	-185.6 kJ/mol
A11	-193.2 kJ/mol

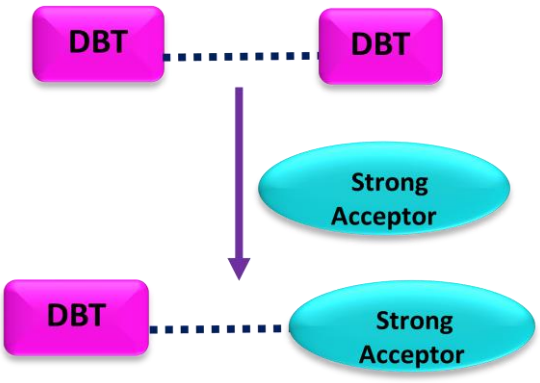

Figure 5-8 Breakage of self-interactions of DBT and inclusion of the new acceptor molecules

5.3.2.2 Weak interactions of the nitro group

Apart from the conventional strong hydrogen bonds such as N-H----N/O and O-H---N/O interactions, non-conventional weak interactions like C-H---O and C-H---π interactions also play an important role in determining crystal packing. After forming strong hydrogen bonds with **DBT** and the corresponding acceptor, the remaining weak acceptor sites of **DBT** (triazole nitrogen and nitro groups) also have a potential to form weak interactions. Having a better understanding of the weak interactions of the nitro group in crystal packing is also important in determining the structural properties of the explosive materials. By considering the position of the lone pairs of the oxygen atoms in the nitro group (Figure 5-9) there are three main modes of intermolecular interactions of nitro groups observed; symmetric bifurcated (a), asymmetric bifurcated (b) and mono coordinated (c) (Figure 5-10) however, the recognition behavior of the nitro group is considered as a function of both intrinsic properties of the nitro group and the nature of the hydrogen bond donor with which it reacts.[23]

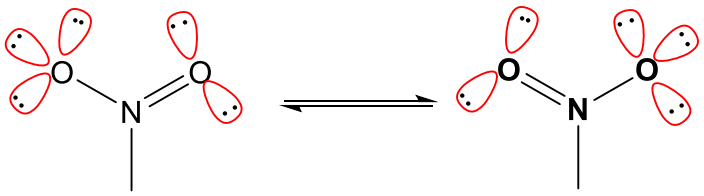

Figure 5-9 Position of the lone pairs of the oxygen atoms in the nitro group

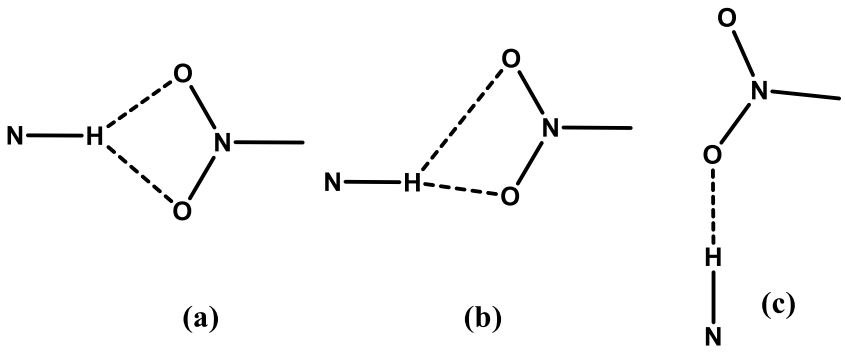

Figure 5-10 Three possible modes of interaction of the nitro group between N–H donor groups [23]

The availability of aromatic –C-H groups, nitro groups of DBT can form C-H---O weak interactions in either of the three modes, however based on the analysis of the full interaction maps of the nitro group with aromatic C-H groups using Mercury software several possible regions of C-H---O interactions were identified (Figure 5-11).

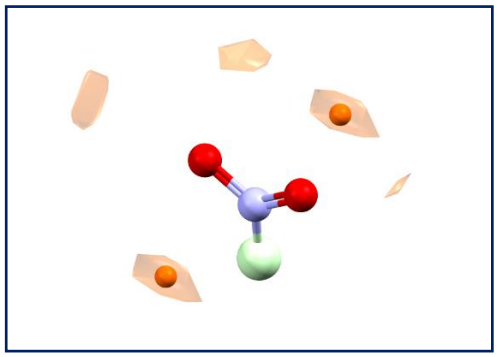

Figure 5-11 Full interaction map of the nitro group which highlights the interactions with aromatic –CH groups.

Based on the analysis, aromatic C-H groups show a higher tendency to interact with the nitrogen atoms from above and below the plane of nitro group. However, by considering the interactions of the oxygen moieties the following modes can be identified (Figure 5-12).

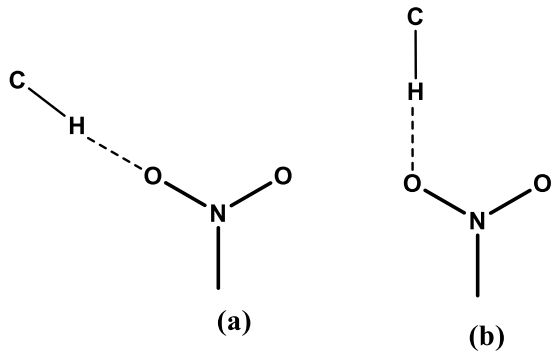

Figure 5-12 Modes of C-H----O interactions based on the full interaction maps calculation

5.3.2.3 Co-crystal of (DBT)$_2$:A7

The crystal structure of **(DBT)$_2$:A7** shows successful formation of N-H---N primary hydrogen- bond interactions with phenazine. As expected the N-H---N self- interaction in DBT is disrupted and a new interaction is formed. Since phenazine is a ditopic acceptor a trimer was formed (Figure 5-13).

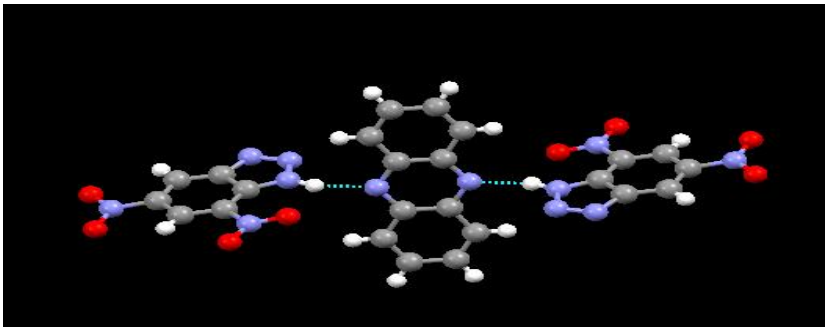

Figure 5-13 Part of the crystal structure of (DBT)$_2$:A7 which shows new N-H---N hydrogen-bond formation with the acidic proton

Phenazine molecules were packed orthogonal to DBT and two different types of C-H—O intereactions were observed. The triazole nitrogen of DBT formed two –C-H----N interactions

with the aromatic hydrogens of phenazine (*ca*.2.59Å) and DBT (*ca*.2.57Å) respectively. Both nitro groups of DBT participated in C-H---O weak interactions (3) with phenazine (*ca*.2.64Å) and DBT (*ca*.2.63 Å) and with the arrangement of the nitro group in close proximity two O----N interactions were observed with an average bond distance of *ca*.2.83Å (Figure 5-14).

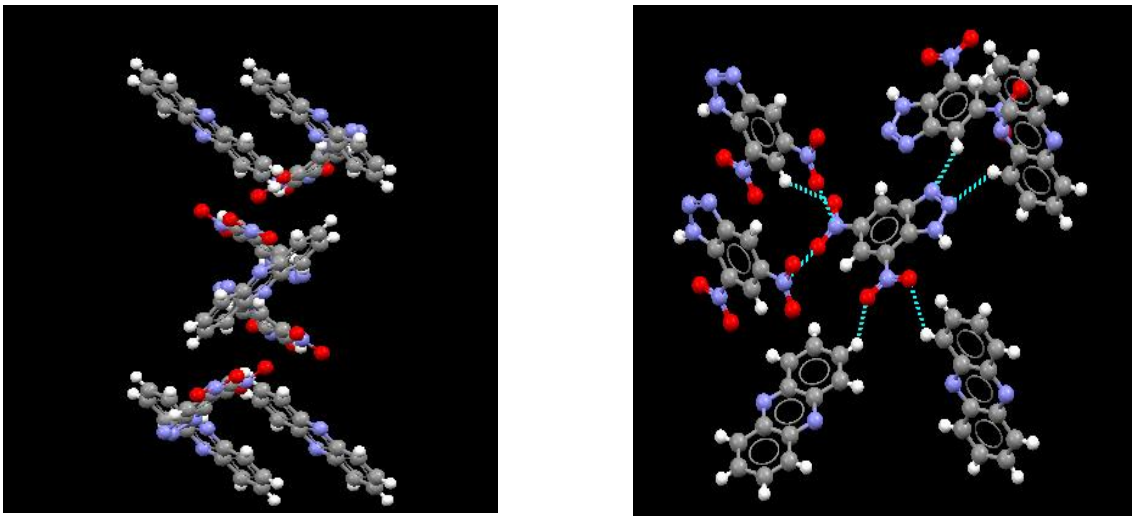

Figure 5-14 Phenazine molecules were packed orthogonal to DBT (left) and C-H---O and C-H---N weak interactions were dominant in the structure.

5.3.2.4 Co-crystals of $(DBT)_2$*: A2*

Similar to the crystal structure of **$(DBT)_2$:A7**, N-H---N hydrogen- bond formation was observed between **DBT** and **A2**. Since the A2 molecule is ditopic, a trimer was formed with two **DBT** molecules (Figure 5-15).

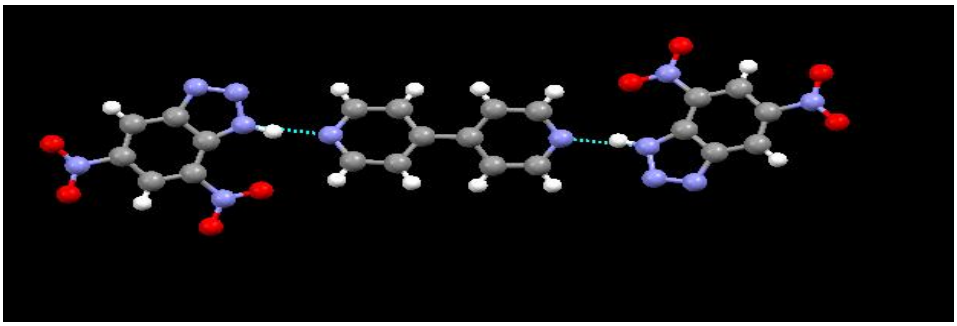

Figure 5-15 Successful N-H---N hydrogen bond formation with the acidic proton of DBT with A2

A network of weak C-H---O and C-H----N interactions were observed with the nitro and triazole groups respectively. The average bond distance of the C-H---O interaction is *ca*.2.51Å and that of the C-H----N interaction is *ca*.2.53Å. Nitro group formed six single point interactions with the aromatic hydrogens of **A2** and **DBT** and the triazole nitrogen formed two interactions (Figure 5-16).

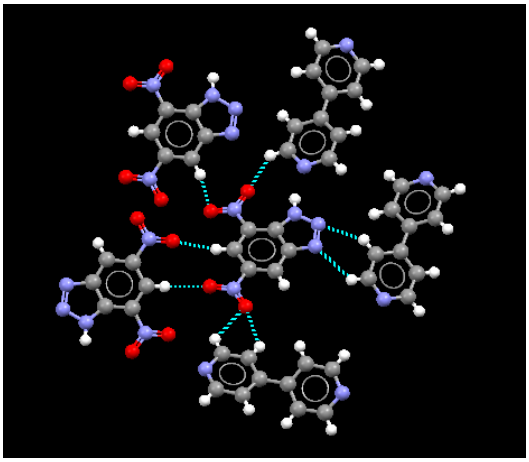

Figure 5-16 C-H----N interactions formed by triazole group and C-H---O interactions formed by nitro group

5.3.2.5 Co-crystal of DBT:A11

Structural consistency was maintained by forming a new N-H---N hydrogen bond with DBT and **A11**. However, **A11** is a monotopic acceptor and a dimer formation was observed (Figure 5-17).

The triazole nitrogen atoms formed two C-H---N short contacts with aromatic hydrogen atoms of A11 (*ca.*2.595Å) and the nitro group formed three C-H---O weak interactions with a bond distance of *ca.*2.604 Å (Figure 5-18).

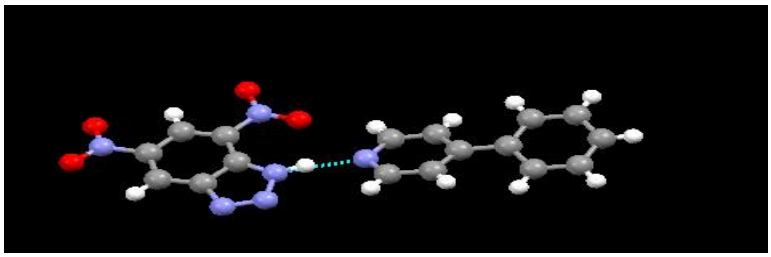

Figure 5-17 Dimer formation via N-H---N interaction with the monotopic A11 and DBT

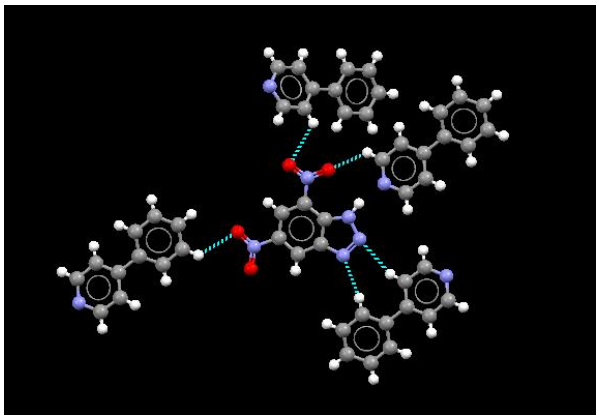

Figure 5-18 C-H----N short contacts of triazole moiety and C-H----O interactions of the nitro group

5.3.2.6 Crystal structure of $(DBT^{-})_2$*:* $A5^{+}$

Unlike previous structures, now we observed proton transfer from the **DBT** N-H group to the pyridyl moiety forming $N\text{-}H^{+}\text{---}N^{-}$ charge-assisted hydrogen bonds. The crystal arrangement showed a trimer formation with ditopic **A5** (Figure 5-19).

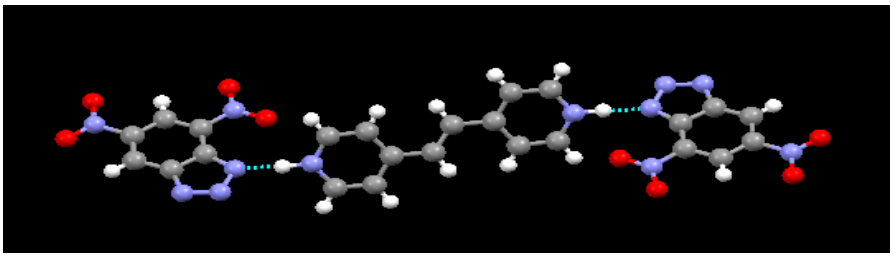

Figure 5-19 A proton transfer occurred from DBT to A5 and a N-H^{+}---N^{-} ionic interaction was formed

The C-H----O weak interactions formed by the nitro group were dominant with a average bond distance of 2.546 Å. Unlike previous structures the C-H---N short contacts of the triazole nitrogens were not observed (Figure 5-20).

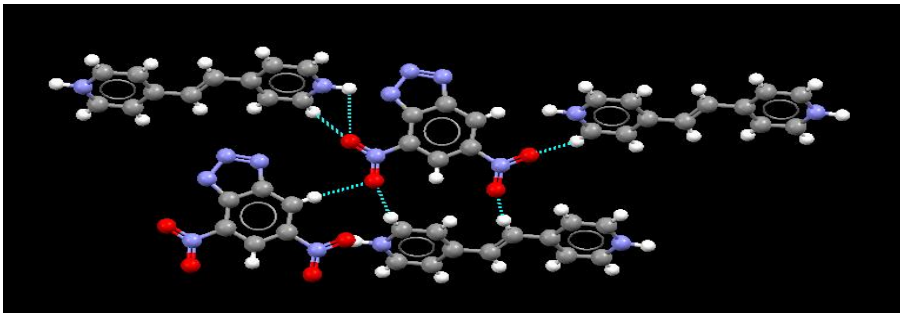

Figure 5-20 C-H----O interactions of the nitro groups in the crystal structure of $(DBT^{-})_2$: $A5^{+}$

Table 5-4 Hydrogen-bond parameters of co-crystals

Co-crystal		D-H (Å)	H----A(Å)	D----A(Å)	DH-A(º)
$(DBT)_2$:A7	N(3)-H(3)---N(19)	0.96 (2)	1.92 (2)	2.831 (3)	156 (3)
$(DBT)_2$:A2	N(18)-H(18)---N(40)	0.97 (9)	1.82 (7)	2.767 (5)	167 (6)
$(DBT^{+})_2$:$A5^{-}$	N(20)-H(20)---N(1)	1.052(19)	1.64 (2)	2.689 (2)	176 (3)
DBT:A11	N(3)-H(3)---N(16)	0.96 (2)	1.85 (3)	2.786 (2)	165 (2)

5.3.2.7 Analysis of the weak C-H---O interactions of the nitro group

By analyzing the structural outcomes of **DBT** with different co-formers it was evident that the acidic N-H protons of DBT prefer to form new hydrogen bonds with strong acceptors by avoiding self N-H---N hydrogen-bond formation. Nitro groups formed a network of C-H---O interactions in all four crystal structures with a average distance of < 2.65 Å, which is in line with the reported bond distances of the C-H---O interaction.[24] In all four crystal structures eighteen C-H---O interactions were observed and by considering the mode of the interaction, the following pattern was identified (Figure 5-21).

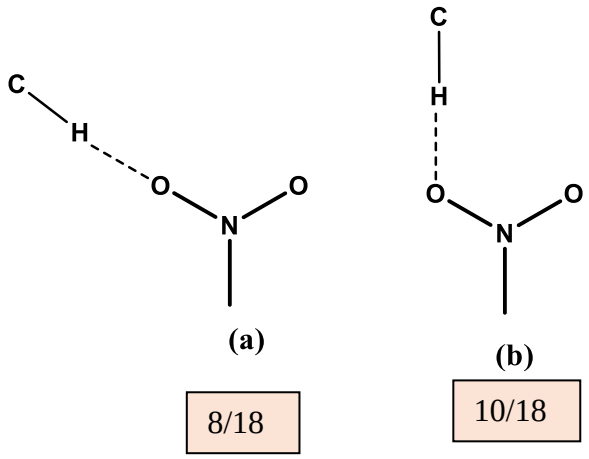

Figure 5-21 Distribution of the C-H----O interaction in the four crystal structures

Compared to the three possible modes of interactions of the nitro group (Figure 5-10) the C-H group prefers the mono-coordinated interaction, and among the two possible modes of C-H---O interactions (according to the full interaction maps calculation), there is an ~ equal distribution among the four crystal structures.

5.3.3 Explosive and thermal properties of DBT and its co-crystals

5.3.3.1 Analysis of the explosive properties

The explosive properties of new compounds were calculated based on the established procedures.[25] We observed a decrease in explosive properties of new co-crystals compared to the parent DBT molecule. Among the co-crystals **DBT:A11** has the lowest values for density, detonation pressure, detonation velocity and oxygen balance. **A11** is a monotopic acceptor molecule and there is only one energetic DBT molecule incorporated into the crystal unit, therefore a decrease of explosive properties can be expected (Table 5-5).

Table 5-5 Calculated explosive properties of DBT and its co-crystals

Compound	**Density (g/cm^3)**	**Detonation pressure (GPa)**	**Detonation Velocity(km/s)**	**Oxygen balance (%)**
DBT	1.645	22.8	7.3	-72.6
$(DBT)_2$:A7	1.606	15.7	6.1	-125.8
DBT:A11	1.509	12.5	5.5	-158.2
$(DBT^-)_2:A5^+$	1.607	16.7	5.1	-132.4
$(DBT)_2$:A2	1.653	18.0	6.5	-119.7

However, the overall decrease of explosive properties is mainly due to the incorporation of non-energetic materials into crystals. In all the co-crystals decreased oxygen balance was observed due to the incorporation of more carbon atoms in to the system through co-formers.

5.3.3.2 Analysis of the thermal properties

DBT and all the co-crystals melt before decomposition. Except for **DBT:A11,** melting points of the other co-crystals showed an increase compared to the melting point of **DBT**. This observation can be related to the presence of strong N-H---N hydrogen bonds and the amount of

weak interactions present in the crystals. **DBT:A11** showed the lowest melting point in this group and as **A11** is monotopic acceptor only one strong N-H—N bond was formed, also this molecular system has the least amount of intermolecular C-H---O interactions among the four co-crystals. However, decomposition temperature of all the co-crystals showed less than 30^{o} C decrease in value compared to the parent energetic material, but all the values were above 250^{o} C and we could consider that co-crystallization has not affected the thermal stability of these new compounds (Table 5-6).

Table 5-6 Thermal properties of DBT **and its co-crystals**

Compound	**Melting point (^{o}C)**	**Decomposition point (^{o}C)**
DBT	196	291
$(DBT)_2$:A7	221	285
DBT:A11	175	267
$(DBT^{+})_2$:$A5^{-}$	258	263
$(DBT)_2$:A2	255	262

5.3.3.3 Analysis of the Impact sensitivity

Impact sensitivity determines the material suitability as a primary and secondary explosive material and determines the safety for transporting and handling. Based on the experimental analysis **DBT** showed an H_{50} value of 132 cm and **$(DBT)_2$:A7** and **DBT:A11** showed a value higher than 144 cm (maximum limit of the apparatus). Obtaining a higher value than **DBT** in impact drop testing indicates a decrease of impact sensitivity. This observation is in contrast to some of the **DBT** derivatives and salts which showed an increase in sensitivity after modifications to the hydroxyl ammonium salt of **DBT** and diamino-5,7-dinitrobenzotriazole.

5.3.3.4 Corrosion test studies

To observe the effect of co-crystallization on reducing the chemical reactivity of **DBT,** a corrosion test was carried out on a copper strip. A small amount of sample (~ 1-3 mg) was placed on a copper strip and a drop of methanol was added. Observation was taken after 1 h. Based on the results, **DBT** showed a rapid onset of corrosion on the copper strip (Figure 5-22), while the co-crystals of **DBT** showed no reaction with the copper strip (Figure 5-23 and 5-24).

Figure 5-22 Corrosion test study of DBT **on a copper strip results for initial (left) and 1 h later (right)**

Figure 5-23 Corrosion test study of $(DBT)_2$:A7 **on a copper strip results for initial (left) and 1 h later (right)**

Figure 5-24 Corrosion test study of co-crystal DBT:A11 **on a copper strip results for initial (left) and 1 h later (right)**

5.4 Conclusions

In this study, we successfully suppressed the chemical reactivity and decreased the sensitivity of **DBT** by introducing co-formers in to the system through N-H---N hydrogen bond formation. (Figure 5-25) Out of fifteen positive co-crystals (through IR analysis) four crystals were analyzed and data confirmed the consistency of hydrogen bond formation with the nitrogen based acceptors. With ditopic acceptors more **DBT** molecules were incorporated and produced higher thermal and explosive properties compared to the monotopic acceptors which lead to a significant decrease in the explosive properties. Therefore, selecting mulitopic acceptors as co-

crystallization agents with **DBT** is more effective to obtain enhanced explosive and thermal properties.

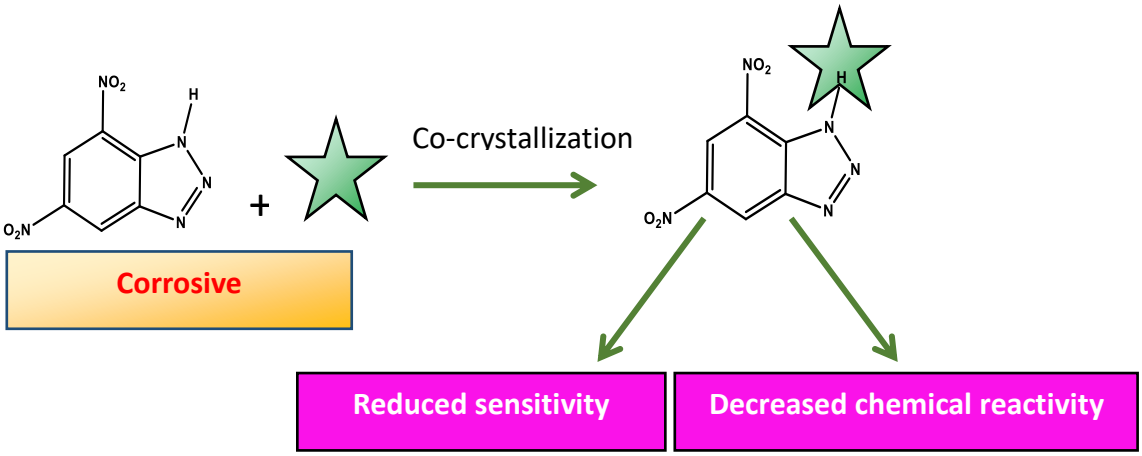

Figure 5-25 Outcome of the study

5.5 References

1. A. Portugal, J. Campos, P. Simões, L. Pedroso and I. Plaksin, in *Defense Industries: Science and Technology Related to Security: Impact of Conventional Munitions on Environment and Population*, eds. P. C. Branco, H. Schubert and J. Campos, Springer Netherlands, Dordrecht, 2004, 209-220; J. Zhang, L. A. Mitchell, D. A. Parrish and J. n. M. Shreeve, *J. Am. Chem. Soc.*, 2015, **137**, 10532-10535; A. A. Gidaspov, V. Bakharev, K. Y. Suponitsky, V. G. Nikitin and A. B. Sheremetev, *RSC Advances*, 2016, **6**, 104325-104329.
2. L. Mosca, S. Karimi Behzad and P. Anzenbacher, *J. Am. Chem. Soc.*, 2015, **137**, 7967-7969.
3. H. Abusaidi and H. R. Ghaieni, *J. Therm. Anal. Calorim.*, 2017, **127**, 2301-2306.
4. Z.-B. Zhang, T. Li, L. Yin, X. Yin and J.-G. Zhang, *RSC Advances*, 2016, **6**, 76075-76083; P. K. Swain, H. Singh and S. P. Tewari, *J. Mol. Liq.*, 2010, **151**, 87-96.

5. P. Yin, C. He and J. n. M. Shreeve, *Chem. Eur. J.*, 2016, **22**, 2108-2113.

6. Y. Tang, C. He, G. H. Imler, D. A. Parrish and J. n. M. Shreeve, *J. Mater.Chem. A*, 2016, **4**, 13923-13929.

7. F. Li, X. Cong, Z. Du, C. He, L. Zhao and L. Meng, *New J. Chem.*, 2012, **36**, 1953-1956.

8. P. Yin, C. He and J. M. Shreeve, *J. Mater. Chem. A*, 2016, **4**, 1514-1519.

9. C. Li, M. Zhang, Q. Chen, Y. Li, H. Gao, W. Fu and Z. Zhou, *Chem. Eur. J.*, 2017, **23**, 1490-1493.

10. D. Fischer, J. L. Gottfried, T. M. Klapötke, K. Karaghiosoff, J. Stierstorfer and T. G. Witkowski, *Angew. Chem. Int. Ed.*, 2016, **55**, 16132-16135.

11. P. Yin, D. A. Parrish and J. n. M. Shreeve, *Angew. Chem. Int. Ed.*, 2014, **53**, 12889-12892; R. Tsyshevsky, P. Pagoria, M. Zhang, A. Racoveanu, A. DeHope, D. Parrish and M. M. Kuklja, *J. Phys.l Chem. C*, 2015, **119**, 3509-3521.

12. Q. Zeng, Y. Ma, J. Li and C. Zhang, *CrystEngComm*, 2017, **19**, 2687-2694.

13. C. Zhang, X. Xue, Y. Cao, J. Zhou, A. Zhang, H. Li, Y. Zhou, R. Xu and T. Gao, *CrystEngComm*, 2014, **16**, 5905-5916; L. H. S. Y. G. S. C. L. M. Q. J. Xuehai, *J. Mol. Model.*, 2013, **19**, 4909-4917.

14. H.-R. Li, Y.-J. Shu, C. Song, L. Chen, R.-J. Xu and X.-H. Ju, *Chin. Chem. Lett.*, 2014, **25**, 783-786; K. B. Landenberger, O. Bolton and A. J. Matzger, *J. Am. Chem. Soc.*, 2015, **137**, 5074-5079; H. Xu, X. Duan, H. Li and C. Pei, *RSC Adv.*, 2015, **5**, 95764-95770; C. Zhang, Y. Cao, H. Li, Y. Zhou, J. Zhou, T. Gao, H. Zhang, Z. Yang and G. Jiang, *CrystEngComm*, 2013, **15**, 4003-4014.

15. C. B. Aakeröy, T. K. Wijethunga and J. Desper, *Chem. Eur. J.*, 2015, **21**, 11029-11037.

16. Q.-H. Lin, Y.-C. Li, Y.-Y. Li, Z. Wang, W. Liu, C. Qi and S.-P. Pang, *J. Mater. Chem.*, 2012, **22**, 666-674.

17. V. D. G. A. Sudheer Kumar, S. Subrahmanyam,and Akhila K. Sahoo, *Chem. Eur. J.* , 2013, **19**, 509 – 518.

18. T. M. Klapötke, C. Pflüger and M. W. Reintinger, *Eur. J. Inorg. Chem.*, 2016, **2016**, 138-147.

19. D. Ehlers, T. M. Klapötke and C. Pflüger, *Chem. Eur. J.l*, 2015, **21**, 16073-16082.

20. A. v. O. a. T. Lehmann, *Cent. Eur. J. Energ. Mater.*, 2016, **13**, 273-288.

21. W. K. Robert T. Paine, Theodore T. Borek,Gary L. Wood,Eugene A. Pruss,Eileen N. Duesler,and Michael A. Hiskey, *Inorg.chem*, 1999, **38**, 3738-3743.

22. Infrared Spectroscopy Absorption Table.

23. J. M. A. Robinson, D. Philp, K. D. M. Harris and B. M. Kariuki, *New J. Chem.*, 2000, **24**, 799-806.

24. T. Steiner, *J. Chem. Soc., Chem. Commun.*, 1994,; T. Steiner, *New J. Chem.*, 1998, **22**, 1099-1103.

25. B. Z. Yan, Ning Ning; Ma, Hai Xia; Song, Ji Rong; Zhao, Feng Qi; Hu, Rong Zhu *S. Afr. J. Chem.*, 2013, **66**.

Chapter 6 - Enhancing chemical stability of energetic derivative tetranitrobisimidazole through co-crystallization: A solution to hygroscopicity and acidity issues

6.1 Introduction

6.1.1 Background

One of the major problems associated with dense nitrogen containing heterocycles as energetic materials is the presence of acidic N-H protons which causes higher chemical reactivity and limits the long-term storage and handling. Hygroscopicity is often a consequence of having acidic N-H protons which limits the usage of energetic materials.[1] Hygroscopicity is the tendency of a material to absorb moisture, and the introduction of water into an explosive is highly undesirable.[2, 3] Introduction of water into a reactive material can reduce the sensitivity and alter the stability. For an example, ammonium dinitramide (ADN) is a relatively newly discovered energetic material and the smooth development of the propellants based on ADN is limited in the USA due to its severe hygroscopic properties. [2] Designing new energetic materials without acidic protons or making salts is the most common approach to reduce hygroscpoicity, however designing new molecules with desired performance, stability and acceptable sensitivity has not shown to be an easy task.[4 5] To the best of our knowledge co-crystallization technology has not been applied to hygroscopic energetic materials. Therefore there is an urgent requirement to determine if this technology can replace water molecules and improve stability and properties of hygroscopic energetic materials (Figure 6-1).

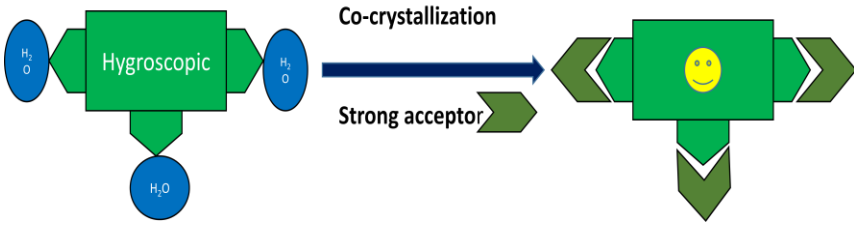

Figure 6-1 Replacement of water molecules of hygroscopic materials through co-crystallization

6.1.2 TNBI as an energetic material

4,4',5,5'-Tetranitro-2.2'biimidazole (**TNBI**) is an energetic material with high thermal stability and a positive oxygen balance, and is referred to as a potential RDX replacement.[6] However, there are four electron withdrawing nitro groups in the molecule which makes the N-H protons highly acidic (Figure 6-2). For this reason, **TNBI** is chemically reactive and can cause problems for long term storage and handling. Also **TNBI** is hygroscopic which makes it almost impossible to use as an energetic material.[7]

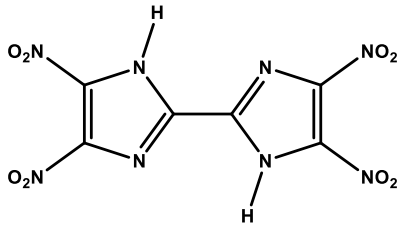

Figure 6-2 Structure of TNBI

The crystal structure of **TNBI** itself shows that two water molecules are incorporated in the lattice via N-H---O hydrogen bonds (Figure 6-3).[8] To eliminate water we need to introduce molecules which are capable of forming strong hydrogen bonds with N-H protons.

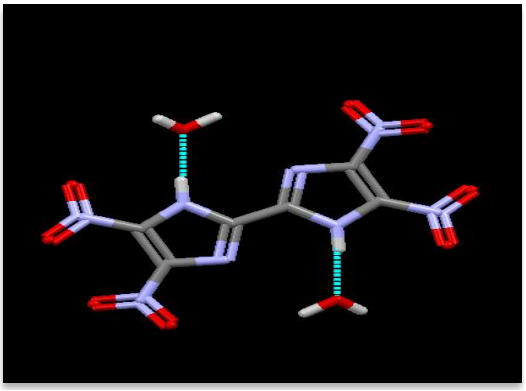

Figure 6-3 Part of the crystal structure of TNBI showing N-H---O hydrogen bond formation with the water molecules[8]

6.1.3 Goals of the study

In this study, we expect to answer the following questions,

1) Can we replace water molecules in TNBI with suitable co-formers?
2) Can we reduce the chemical reactivity and hygroscopicity of TNBI through co-crystallization?
3) Will the explosive and thermal properties of TNBI change by changing the co-former?

In order to find out the behavior of TNBI in co-crystallization experiments, fifteen different co-formers based on nitrogen and oxygen as acceptor moieties were selected (Figure 6-4).

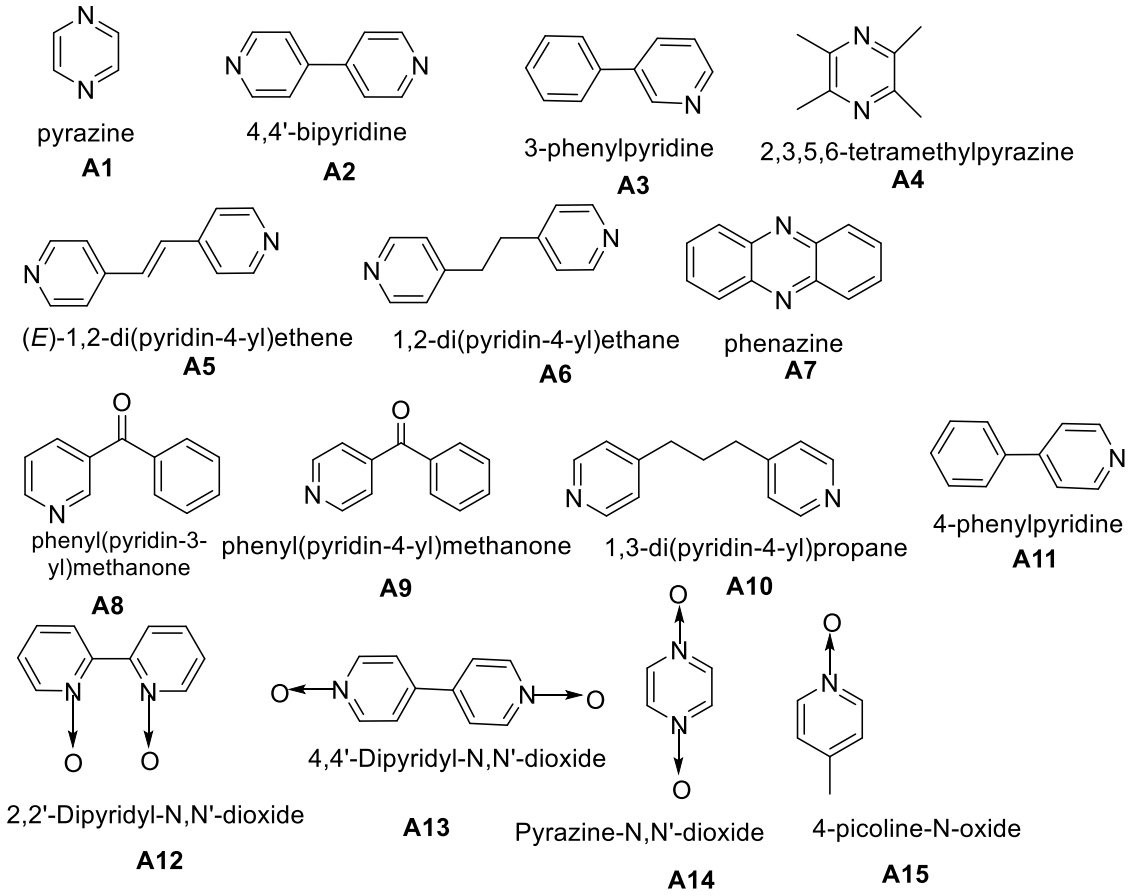

Figure 6-4 Acceptors used for the co-crystallization experiments with TNBI

6.2 Experimental

All the chemicals including co-formers were purchased via available commercial sources and used without further purification. ^{1}H NMR spectra were recorded on a Varian Unity plus 400 MHz spectrophotometer in $CDCl_3$. IR spectra were recorded on a Nicolet 380 FT-IR. Melting points were determined by Fisher-Johns melting point apparatus. Decomposition points were measured on a DSC Q 20 and thermo gravimetric studies were done on a TGA Q 50.**TNBI** is a potential explosive molecule. Even though no incident occurred during handling, synthesis was done in a small scale (~ 200 mg) and handled carefully. All the synthesis was performed inside a fume hood and used nonmetallic spatulas to measure **TNBI**. Kevlar gloves, lab coat and goggles were worn all the time.

6.2.1 Synthesis of 2, 2'- bisimidazole (BI)[6]

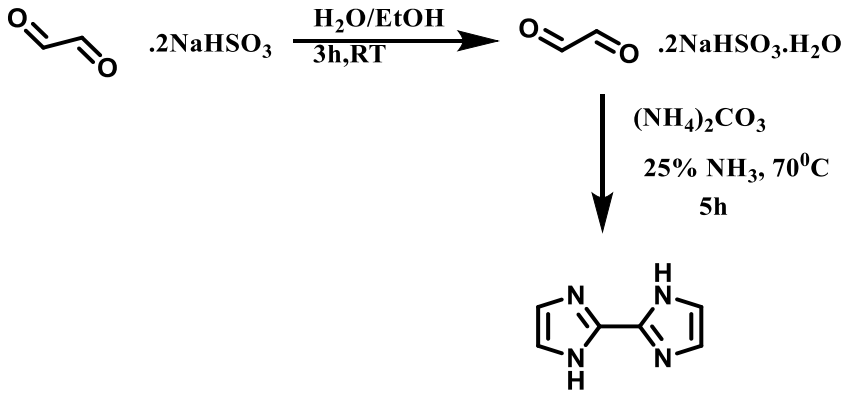

To a solution of sodium bisulfite (18.30 g, 175.5 mmol) in 90 ml of water, 50 ml of ethanol was added. Afterward 12.77 g (38 mmol) of 40 % glyoxal was added and the mixture was stirred for 1.5 h at ambient temperature. The white solid obtained was then filtered and washed with ethanol and diethyl ether. The solid was redissolved in aq. NH_3(138 ml, 25%) and ammonium carbonate (5 g). The mixture was refluxed for 4h and cooled to room temperature. After filtering and washing the resulted solid with ethanol and diethylether light yellow color BI (1 g) was obtained in high purity. (38%) M.p > 300^oC. Lit value >300^0C[9] (^1H NMR, DMSO-d_6, 7.06 (m, 4H), 12.55 (s, 2H)

6.2.2 Synthesis of 4,4',5,5'-tetranitro-2,2'-bisimidazole (TNBI)[6]

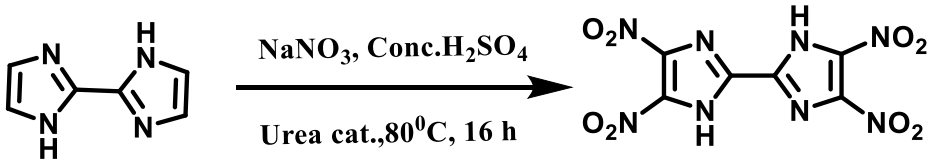

A suspension of sodiumnitrate (1.8 g 5.7 mmol) was prepared by adding 2 mg (0.030mmol) of urea in 3 ml of sulfuric acid at 0^oC. 2,2'-bisimidazole (0.50 g, 4.5 mmol) was added in small portions. Mixture was stirred at ambient temperature for 1 hour and heated to 85^oC-90^oC for 16 h. Suspension was then poured into ice water (20 ml) and the resulting

precipitate was filtered and washed with ice water to get a yellow color product in ~48% yield. Dec.point 289^{o}C. Lit. 287^{o}C[7]

6.2.3 Synthesis of co-crystals

Co-crystals were made with monotopic and ditopic acceptor molecules which contain oxygen and nitrogen as acceptor moieties. Co-formers were mixed according to the stoichiometry and dissolved in the minimum amount of solvent and subjected to slow evaporation to get suitable crystals. Among the co-formers, 4,4'-bipyridyl, *trans*-1,2-bis(4-pyridyl) ethylene, pyrazine and 1,2-bis(4-pyridyl)ethane showed rapid yellow color precipitation upon addition of the solvents and the resulting solids had very poor solubility in common solvents and not further analyzed. IR and DSC analysis were performed to confirm co-crystal formation. Out of fifteen experiments, four X-ray quality crystals were obtained (Table 6-1).

Table 6-1 Synthesized co-crystals of TNBI

Co-crystal	**Abbreviation**	**Mole ratio**	**Solvents**	**Decomposition ^{o}C**
TNBI:phenazine	TNBI:A7	1:1	Methanol	284
TNBI:tetramethylpyrazine	$TNBI^{-}:A4^{+}$	1:1	Methanol/THF	278
TNBI:2,2-dipyridyl-N,Ndioxide	TNBI:A12	1:1	THF/acetonitrile	201
TNBI:pyrazine-Noxide	$TNBI:(A14)_2$	1:2	THF/acetonitrile	215

6.2.4 Hygroscopicity studies

Hygroscopicity studies were carried out by placing the co-crystals in a 75% humidity chamber for three weeks. 75 % humidity was generated by using a saturated solution of NaCl. Crystals were analyzed over time through TGA to observe the effect of hygroscopicity (Figure 6-5).

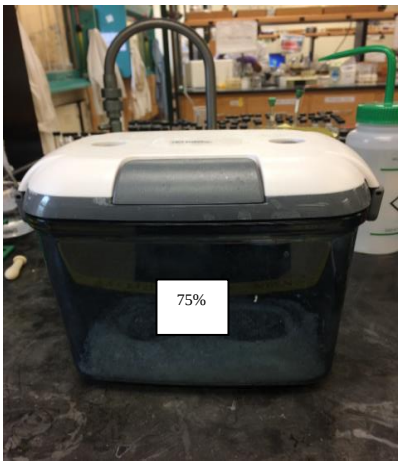

Figure 6-5 Humidity chamber used to analyze hygroscopicity of co-crystals

6.3 Results and discussion

6.3.1 Analysis of co-crystals

TNBI contains four nitro groups and two imidazole nitrogen atom which can act as acceptor moieties for potential donor molecules. Two N-H moieties are capable of acting as hydrogen-bond donors in the presence of suitable acceptors. In this study, we used different nitrogen and oxygen containing acceptors and with the presence of N-H donor groups in **TNBI** as we plan to replace water molecules and get new N-H----N or N-H----O hydrogen bonds (Figure 6.5). With the usage of strong acceptor moieties the nitro group does not have an opportunity to participate in primary hydrogen bonding; however it can form secondary O----N. C-H----O interactions.[10] Principal N-H bending and $–NO_2$ stretching peaks usually appear at 1580-1650 cm^{-1} and 1500-1550 cm^{-1} and 1290-1372 cm^{-1} respectively.[11] The IR spectrum of **TNBI** showed N-H bending at 1589 cm^{-1}, and $–NO_2$ stretches at 1529 $cm^{-1}$and 1317 cm^{-1}. Figure 6.5 shows one example of a positive co-crystal formation observed in IR spectroscopy. In this spectrum, we observe the shift of 1589 cm^{-1} to 1585 cm^{-1} and a shift of 1317 cm^{-1} to 1311

cm^{-1}. However these shifts were not prominent in most of the mixtures and we mainly relied on the DSC analysis for the confirmation of co-crystal formation (Table 6-2).

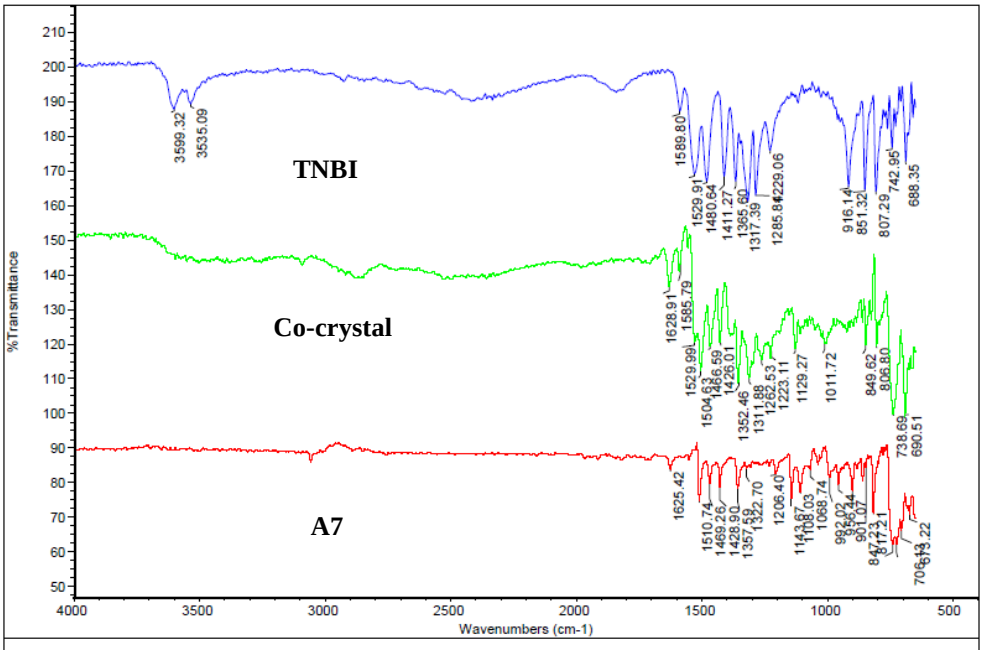

Figure 6-6 IR spectrum of a positive co-crystal which shows the presence of prominent peaks from both the co-formers

Table 6-2 Decomposition temperatures of TNBI **and its co-crystals**

Compound	**Decomposition temperature**
TNBI	289
TNBI:A7	284
TNBI:A12	201
TNBI:$(A14)_2$	215
$TNBI^-:A4^+$	278

6.3.2 Structural analysis of the co-crystals

TNBI is a ditopic donor and in the presence of ditopic oxygen or nitrogen based acceptor molecules it can lead to an infinite chain-like architecture through N-H---N or N-H---O hydrogen-bond formation (Figure 6-7). Even though the nitro groups may not participate in strong hydrogen-bond formation, the presence of four nitro groups can lead to a significant amount of weak interactions which is crucial to the overall crystal packing of the molecule and to obtain dense energetic materials.[12]

Figure 6-7 1-D array of TNBI can be formed with ditopic acceptor molecules

6.3.2.1 Structural analysis of TNBI:A7

N-H protons of **TNBI** successfully formed N-H---N hydrogen bonds with A7 by replacing water molecules. As expected 1-D infinite ladder type architecture was formed (Figure 6-8).

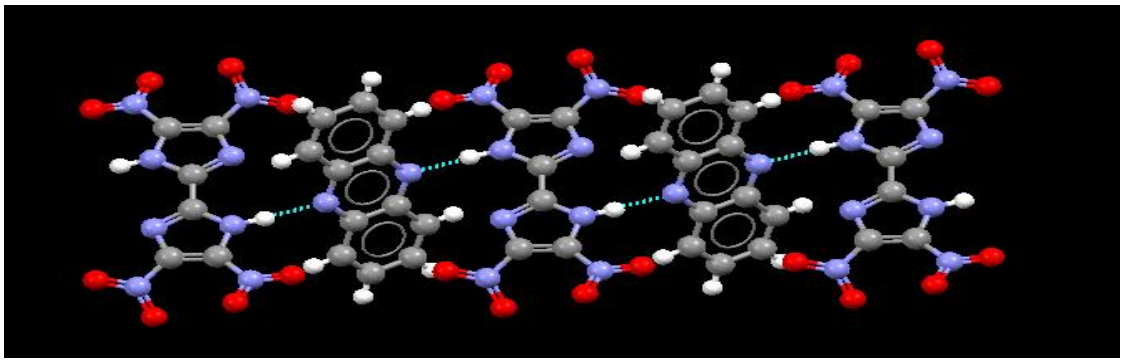

Figure 6-8 Part of the crystal structure of TNBI:A7**. Infinite 1-D architecture was formed through N-H----N interactions**

.

Each oxygen atom in the nitro group formed eight C-H----O weak interactions with a average distance of 2.610 Å (Figure 6-9). All the interactions were seen as single point interactions as

observed in our previous structures (Chapter 5). The nitro group also formed an O----N (π hole) interaction with a average distance of *ca* 3.03 Å and oxygen and nitrogen atoms were arranged orthogonal to each other. Even though this interaction is weaker than C-H---O interactions, O----N bonds played a significant role in overall crystal packing, by arranging **TNBI** in a layered architecture (Figure 6-10).

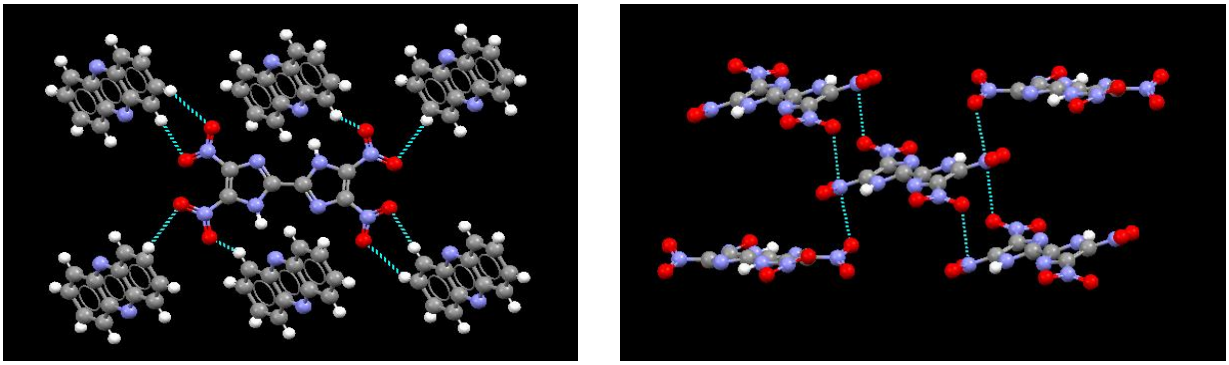

Figure 6-9 Part of the crystal structure of TNBI**: network of C-H----O interactions (left) and O----N (π-hole) interactions of nitro groups(right)**

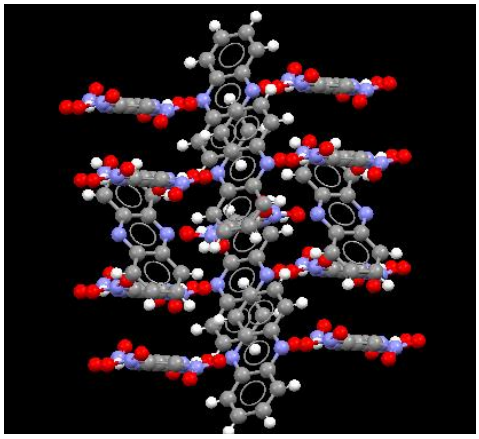

Figure 6-10Part of the crystal packing of TNBI:A7 **which shows the layered arrangement of** TNBI

6.3.2.2 Structural analysis of $TNBI^{-}:A4^{+}$

With **A4**, we observed a proton transfer from **TNBI** forming charge assisted $N\text{-}H^{+}\text{-----}N^{-}$ bnds. Since **A4** is a ditopic acceptor we would expect to have a proton transfer to both nitrogen

atoms in **A4** and to obtain an extended 1-D chain. However only a one nitrogen atom got protonated with the formation of a $R_2^2(7)$ motif (Figure 6-11). This observation was evident with a CSD analysis which shows 119 hits for tetramethylpyrazine that with relatively weak acids mostly one site of **A4** get protonated and other site remain intact.[13] (protonation of both nitrogen was observed with strong acids such as HCl and HBr)

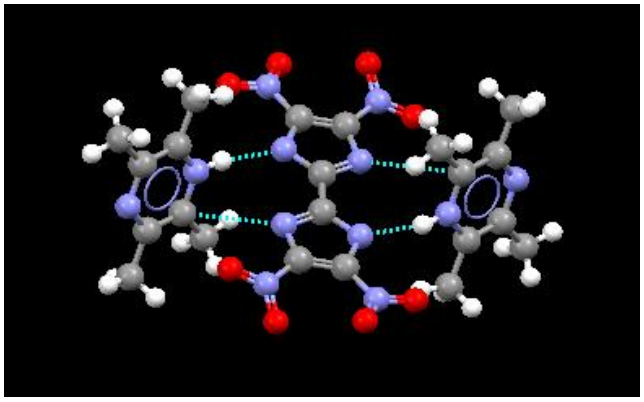

Figure 6-11 A proton transfer from TNBI **to** A4 **occurred with the formation of N-H$^+$-----N$^-$ interaction.**

With methyl C-H groups in close proximity, the nitro group formed a network of eight single point C-H----O interactions with an average bond distance of *ca.*2.61Å (Figure 6-12).

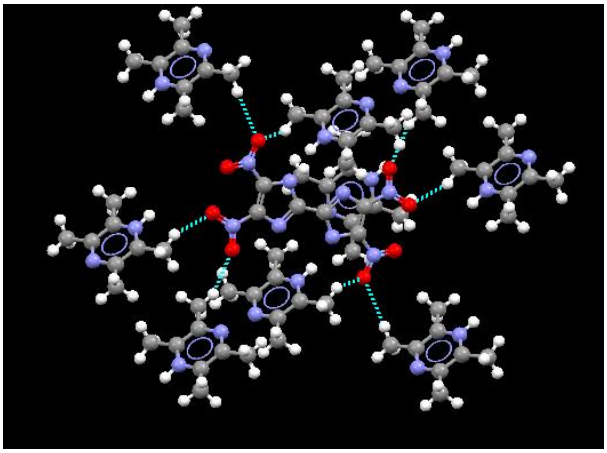

Figure 6-12 Short C-H---O interactions formed by the nitro group

6.3.2.3 Structural analysis of TNBI:A12

With the incorporation of an oxygen based acceptor molecule a similar structural behavior was observed as with nitrogen based acceptors. With ditopic **A12**, a 1-D infinite chain was observed with the formation of N-H---O hydrogen bonds with the replacement of water molecules. (Figure 6.13) Nitro groups formed seven C-H---O interactions with an average bond distance of *ca.*2.52Å and two types of O---N(π-hole) interactions were observed. Based on the close proximity of the oxygen atoms, nitro groups formed O-----N interactions (*ca.*2.953Å) with the neighboring nitro groups which were orthogonal to each other and another O----N interaction formed (2.955Å) with neighboring imidazole nitrogen which was perpendicular to the oxygen atom of the nitro group (Figure 6-14).

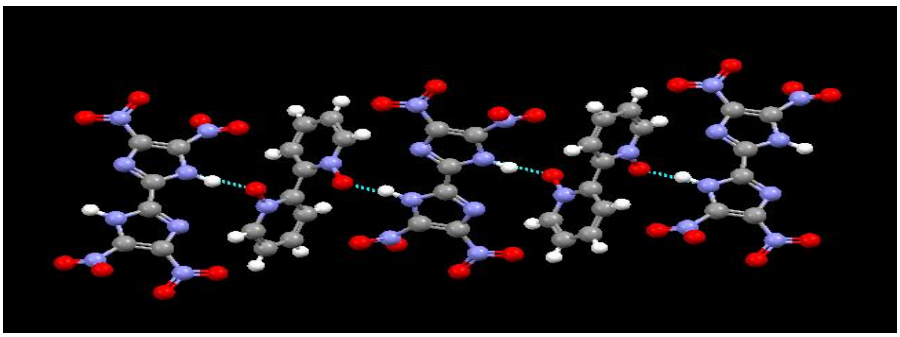

Figure 6-13 Part of the crystal structure of TNBI:A12 **with infinite 1-D chain with N-H---O hydrogen-bond formation**

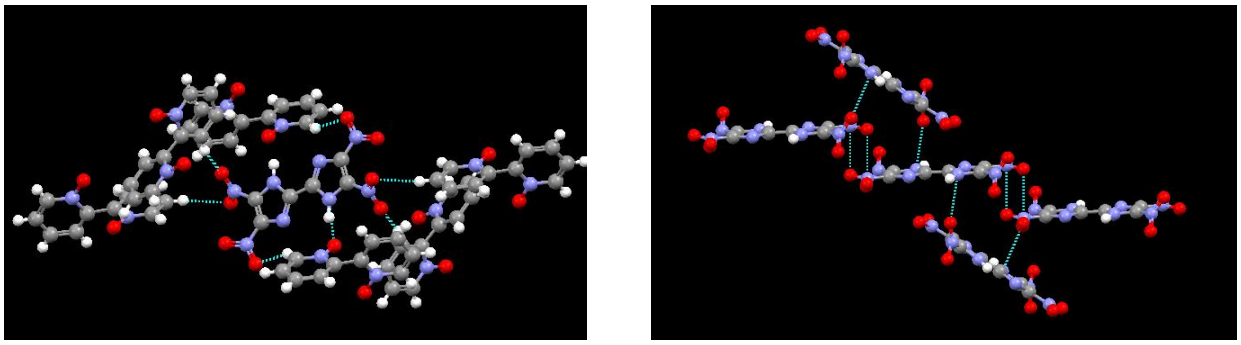

Figure 6-14 C-H---O interactions (left) O---N interactions (right) of nitro groups in TNBI:A12

6.3.2.3 Structural analysis of TNBI:(A14)$_2$

Even though we expected to have a linear 1-D chain with the formation of N-H---O hydrogen bonds, we observed trimer formation leading to a discrete architecture (Figure 6.15). The nitro group formed six single point C-H---O bonds (*ca.*2.579 Å) and a network of O----N interactions were observed with both nitrogen atoms of the nitro group (*ca.*2.831 Å) and the pyrazole nitrogen (*ca.*2.926Å) based on the orthogonal position of the oxygen atom (Figure 6-16).

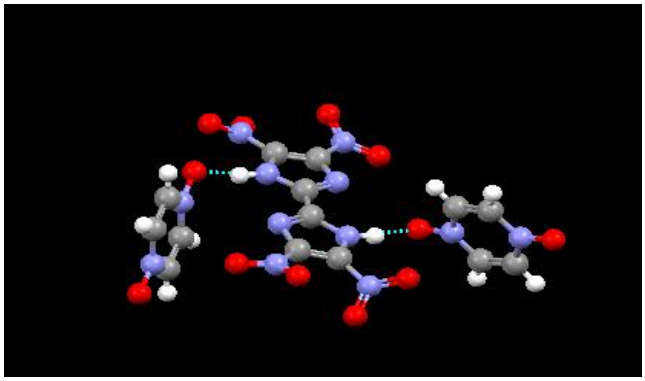

Figure 6-15 Discrete architecture of TNBI:(A14)$_2$ **with N-H---O hydrogen bond formation**

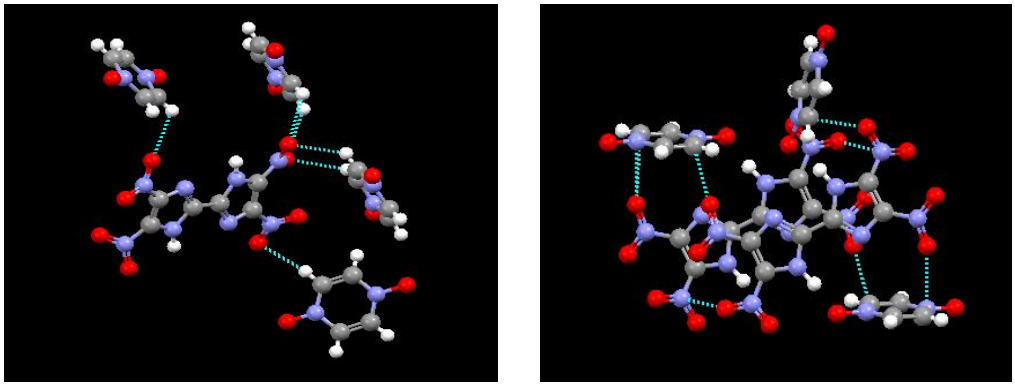

Figure 6-16 C-H---O and O----N interactions of nitro group of TNBI:(A14)$_2$

6.3.2.4 Analysis of the structural outcomes

It is evident that both nitrogen and oxygen based acceptors can form primary hydrogen bonds with the acidic N-H protons of **TNBI** and replace water molecules. However, the presence

of four nitro groups also has played a significant role in the overall crystal packing. In all crystal structures, C-H---O interaction were formed as single point interactions with < 2.65Å bond distance was in accordance with the reported bond distances of other C-H---O interaction of the nitro groups.[14] Out of 23 C-H---O bonds in all four crystals following distribution was observed (Figure 6-17).

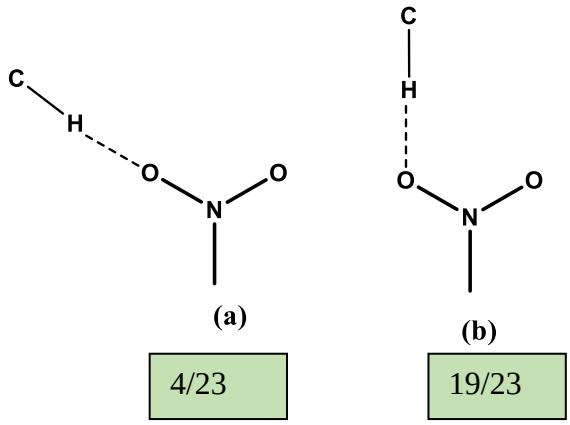

Figure 6-17 Distribution of the C-H----O interactions in TNBI co-crystals

We also observed several O----N interactions played an important role in arranging molecules in layered architectures. This type of interaction is referred to as a π-hole interaction.[15] A π-hole is considered as a positive electrostatic potential on unpopulated π^* orbitals which has the capability to interact with electron donor.[16] It is typically located perpendicular to the molecular framework of a π system (Figure 6-18).

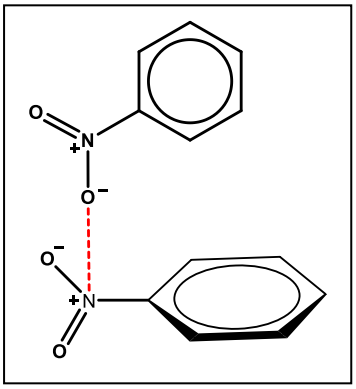

Figure 6-18 Schematic representation of O----N π-hole interactions between two nitro groups

A π-hole nitro interaction can be considered as mode (a) interaction (Figure 6-18) between an oxygen atom and a nitrogen atom of the nitro group. Presence of extensive π-hole interactions in the crystals explains the small amount of mode (a) C-H----O interactions observed in the crystals. When considering the O---N interaction with the nitro groups electron densities are considered to be located above and below the C-N bond.[15] By analyzing the electrostatic potential distribution of TNBI, electron deficient region was observed on the nitrogen atoms of the nitro group which is located above and below the molecular frame work (Figure 6-19).

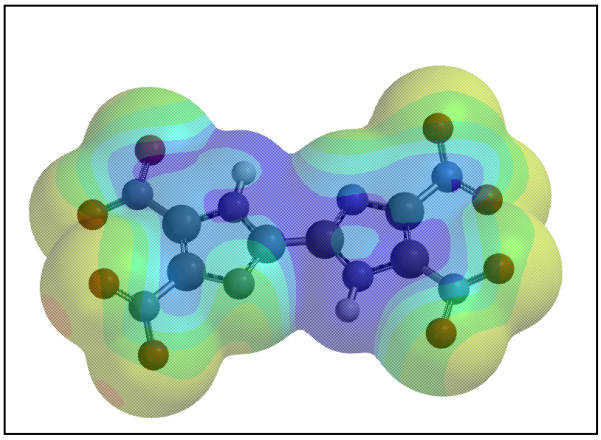

Figure 6-19 Electrostatic potential calculation of TNBI which shows the positive electrostatic potential on the nitrogen atom of the nitro group (blue)

In **TNBI:A7** ,**TNBI:(A14)$_2$** and **TNBI:A12** we observed π-hole interactions with the oxygen atoms of the nitro groups perpendicular to the plane of the **TNBI** molecule.

6.3.3 Calculation of the explosive properties

Densities of the crystals were obtained from the X-ray crystallographic data and explosive properties detonation velocity, detonation pressure and oxygen balance was calculated using established procedures (Table 6-3).[17]

Table 6-3 Explosive properties of TNBI and co-crystals

Compound	**Density g/cm^3**	**Detonation velocity m/s**	**Detonation pressure GPa**	**Oxygen balance%**
TNBI.2H$_2$O	1.789	8295.7	30.8	-22.85
TNBI:A7	1.709	6681.1	19.3	-106
TNBI:A12	1.679	6963.4	20.88	-85.86
TNBI(A14)$_2$	1.819	7924	28.36	-62.4
TNBI$^-$:A4$^+$	1.497	6066.3	14.72	-133.28
RDX	1.816	8753.2	34.6	-21.6

Co-crystallization of energetic materials with non-energetic materials results in decrease of explosive properties, however **TNBI:(A14)$_2$** showed a crystal density closer to RDX, and higher detonation velocity, detonation pressure and a good oxygen balance. **TNBI:A12** showed a good oxygen balance with a slight decrease of explosive properties. **TNBI:A7** also has a comparatively high density with a slight decrease of explosive properties. However, **TNBI$^-$:(A4)$^+$** had the lowest density compared and thus lower explosive properties. Tetramethyl pyrazine consist of extra covalent hydrogen atoms which usually have a lower mass density than oxygen and nitrogen atoms, which lead to a lower crystal density.[18]

6.3.4 Analysis of the thermal stability

Thermal stability of **TNBI** and new solid forms were measured using differential scanning calorimetry. Based on the data, the co-crystals of **TNBI** showed a slight decrease in decomposition temperature compared to **TNBI**. However, all the values were greater than 200^{o}C and can be considered as thermally stable (Figure 6-20).

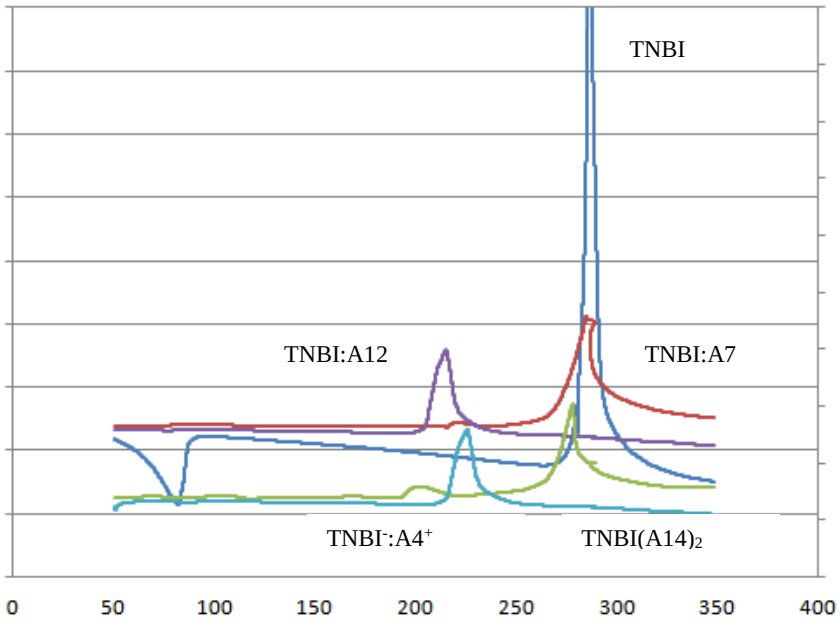

Figure 6-20 Analysis of the decomposition temperature of the TNBI **and its co-crystals**

6.3.5 Hygroscopicity test studies

Even though TNBI is considered as a potential replacement of RDX, its hygroscopic nature makes it unsuitable as an explosive. According to TGA data, **TNBI** shows a loss of weight in the range of 80-100 ^{o}C (Figure 6-21) and this suggests that water is absorbed through acidic hydrogen.[7]

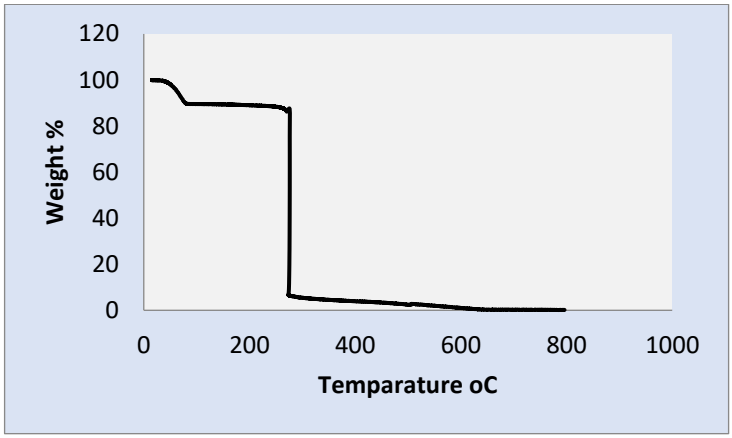

Figure 6-21 TGA analysis of TNBI showing a water loss at a region of 80-100ºC

We have demonstrated successful replacement of water with different co-formers and the acidic N-H protons are no longer available for further reactivity. Analysis of the co-crystals through TGA, did not show any weight loss in the 80-100ºC range confirming successful decrease in hygroscopicity. To further confirm the stability of co-crystals, they were placed in a 75% humidity chamber for one month and the analysis of TGA showed no difference to the initial data, suggesting that hydrogen bond formation between **TNBI** and co-formers is very stable. Figure 6-22 shows TGA analysis of **TNBI:(A14)2** which shows a flat region in the 80-100ºC range.

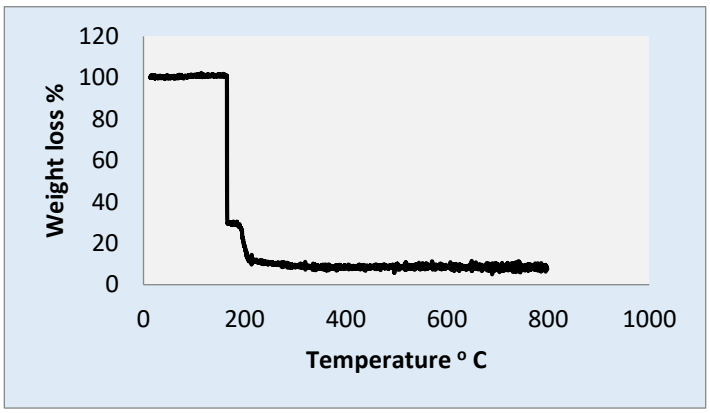

Figure 6-22 TGA analysis of TNBI:(A14)2 **which shows a flat region at 80-100ºC range**

6.3.6 Corrosion test studies

A small amount of sample was placed on a polished copper strip and a drop of methanol was added to aid corrosion. Observation was taken after one hour. Parent **TNBI** showed high corrosion on a copper strip due to the presence of acidic N-H protons (Figure 6-23). All the co-crystals of **TNBI** showed successful decrease in corrosion due to the unavailability of acidic proton for reactivity, through the formation of hydrogen bonds. Figure 6-24 showed one example of successful reduction of corrosion of a co-crystal.

Initial After 1 h

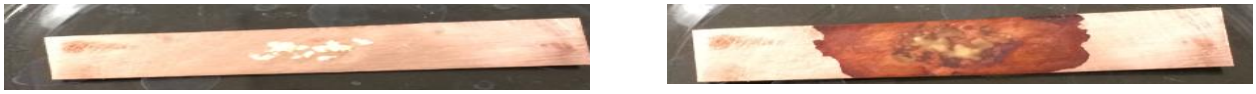

Figure 6-23 Corrosion test studies of TNBI

Figure 6-24 Corrosion test studies of TNBI:A12

6.4 Conclusion

The energetic material **TNBI** was successfully synthesized and subjected to co-crystallization experiments. Crystal data confirmed N-H---N and N-H----O hydrogen bond formation with both oxygen and nitrogen based acceptors with the replacement of water molecules (Figure 6-25). Hygroscopicity test analysis showed successful decrease in hygroscopicity; keeping the solids in a 75% humidity chamber for more than one month confirms the stability of new co-crystals. Corrosion studies on a copper strip further confirm the chemical inactivity and suggest these materials are safe for long term storage and handling. To the best of our knowledge this study is the first attempt taken to reduce hygroscopicity of

energetic materials through co-crystallization and can be successfully applied in future in designing new energetic materials.

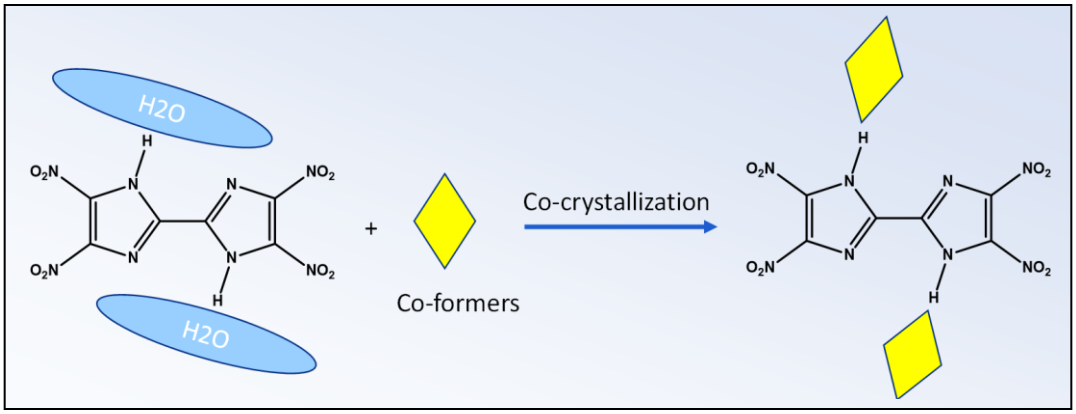

Figure 6-25 Successful reduction of hygroscopicity of TNBI by introducing stable co-formers

6.5 References

1. Y.-N. Li, B.-Z. Wang, Y.-J. Shu, L.-J. Zhai, S.-Y. Zhang, F.-Q. Bi and Y.-C. Li, *Chin. Chem. Lett.*, 2017, **28**, 117-120.
2. T. Gerseck, *Practical military ordnance identification*, GRC press, Taylor and Fransis group, 2014.
3. J. H. Jianhua Cui, Jiange Wang,and Rui Huang, *J. Chem. Eng. Data*, 2010, **55**, 3229-3234.
4. J. Zhang, S. Dharavath, L. A. Mitchell, D. A. Parrish and J. n. M. Shreeve, *J. Am. Chem. Soc.*, 2016, **138**, 7500-7503.
5. D. Fischer, J. L. Gottfried, T. M. Klapötke, K. Karaghiosoff, J. Stierstorfer and T. G. Witkowski, *Angew. Chem. Int. Ed.*, 2016, **55**, 16132-16135; H. Xue, Y. Gao, B. Twamley and J.M. Shreeve, *Chem. Mater.*, 2005, **17**, 191-198.

6. T. M. Klapotke, Preimesser,A and Stierstorfer,J, *Z.Anorg.Allg.chem*, 2012, **638**, 1278-1286.

7. S. K. Hee, And Kim J.S, *Bull.Korean.Chem.Soc*, 2013, **34**, 2503.

8. D. T. Cromer and C. B. Storm, *Acta Crystallogr. Sec. C*, 1990, **46**, 1957-1958.

9. and V. G. Randolph P.Thummel, and Baili Chen *J. Org.Chem.* , 1989, 3057-3061

10. A. Sikorski and D. Trzybiński, *J. Mol. Struct.*, 2013, **1049**, 90-98; S. Tsuzuki, K. Honda, T. Uchimaru and M. Mikami, *J.Chem. Phys.*, 2006, **125**, 124304.

11. Infrared Spectroscopy Absorption Table.

12. E. Gagnon, T. Maris, K. E. Maly and J. D. Wuest, *Tetrahedron*, 2007, **63**, 6603-6613.

13. A. Piecha-Bisiorek, G. Bator, W. Sawka-Dobrowolska, L. Sobczyk, M. Rok, W. Medycki and G. J. Schneider, *J. Phys. Chem. A*, 2014, **118**, 7159-7166; D.-M. Chen, F.-Y. Xia, M.-L. Hu, L. Li and Z.-M. Jin, *Acta Crystallogr. Sec. E*, 2005, **61**, o419-o420.

14. T. Steiner, *J. Chem. Soc., Chem. Commun.*, 1994, Steiner, *New J. Chem.*, 1998, **22**, 1099-1103.

15. A. Bauza, A. V. Sharko, G. A. Senchyk, E. B. Rusanov, A. Frontera and K. V. Domasevitch, *CrystEngComm*, 2017, **19**, 1933-1937.

16. A. Bauzá, T. J. Mooibroek and A. Frontera, *ChemPhysChem*, 2015, **16**, 2496-2517.

17. B. Z. Yan, Ning Ning; Ma, Hai Xia; Song, Ji Rong; Zhao, Feng Qi; Hu, Rong Zhu *S. Afr. J. Chem.*, 2013, **66**.

18. X. Wei, Y. Ma, X. Long and C. Zhang, *CrystEngComm*, 2015, **17**, 7150-7159.

Appendix A - ^{1}H NMR, ^{19}F NMR and PXRD data

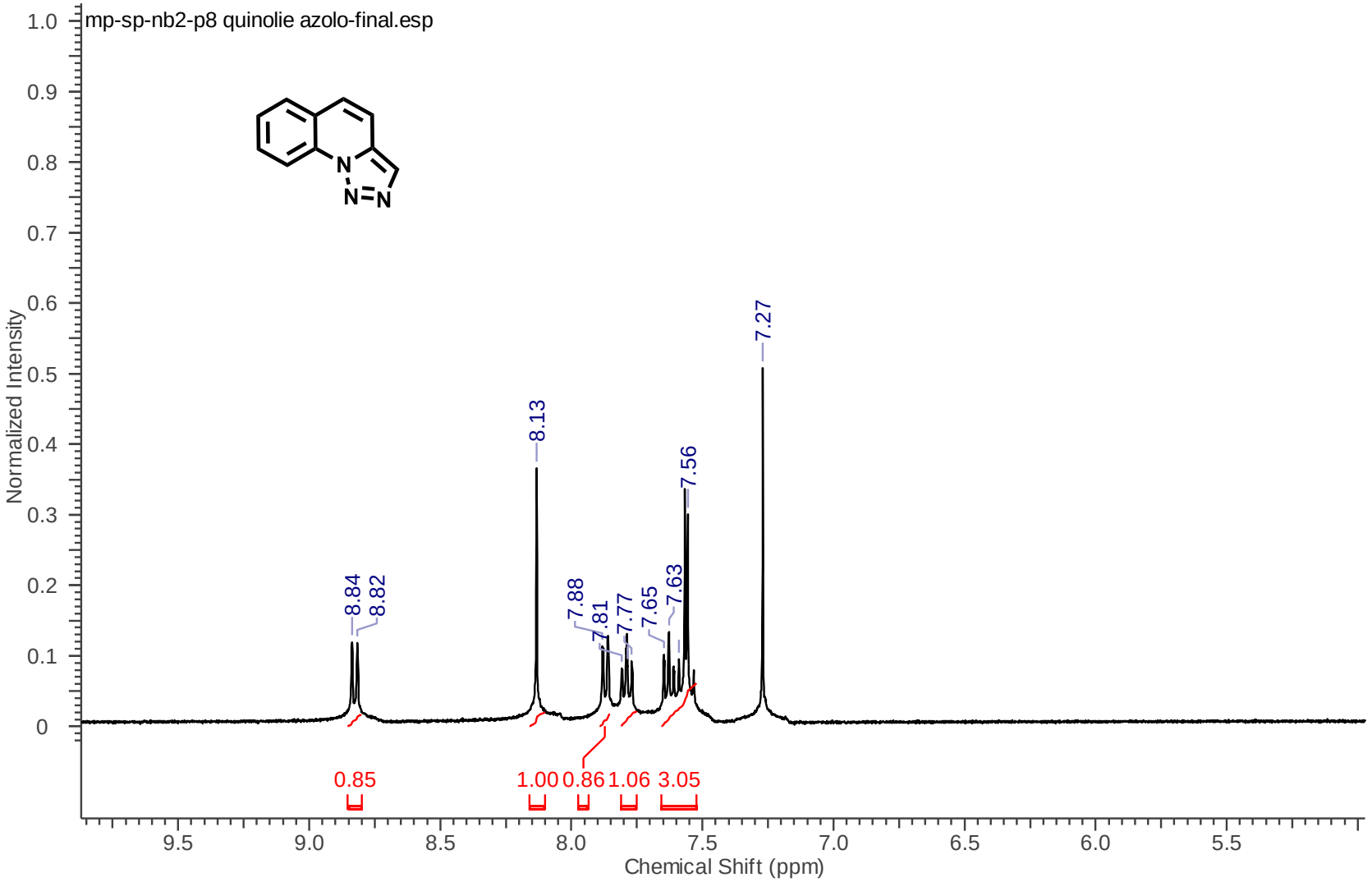

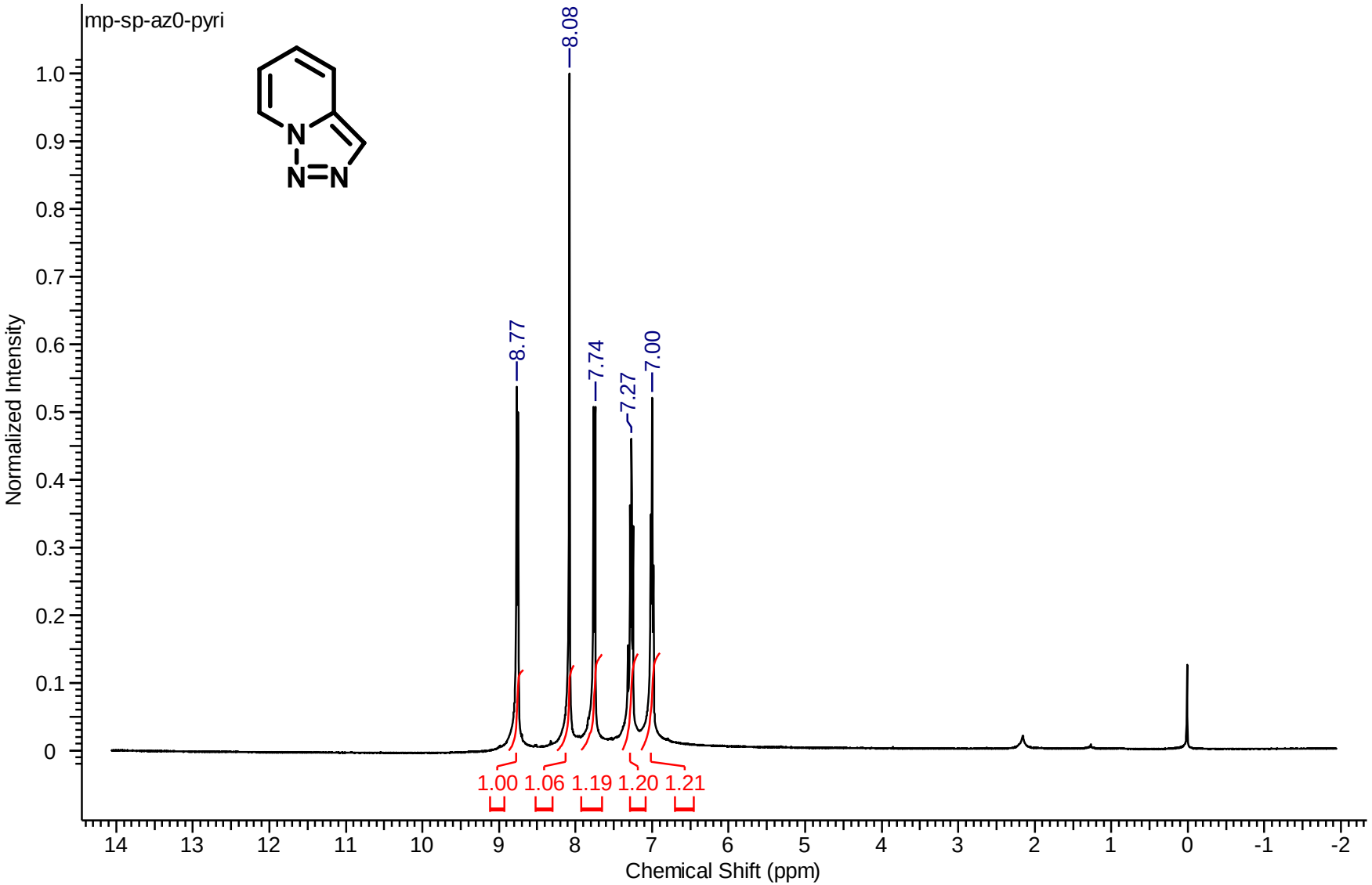
mp-sp-az0-pyri
8.08
8.77
7.74
7.27
7.00
1.00 1.06 1.19 1.20 1.21
Normalized Intensity
Chemical Shift (ppm)

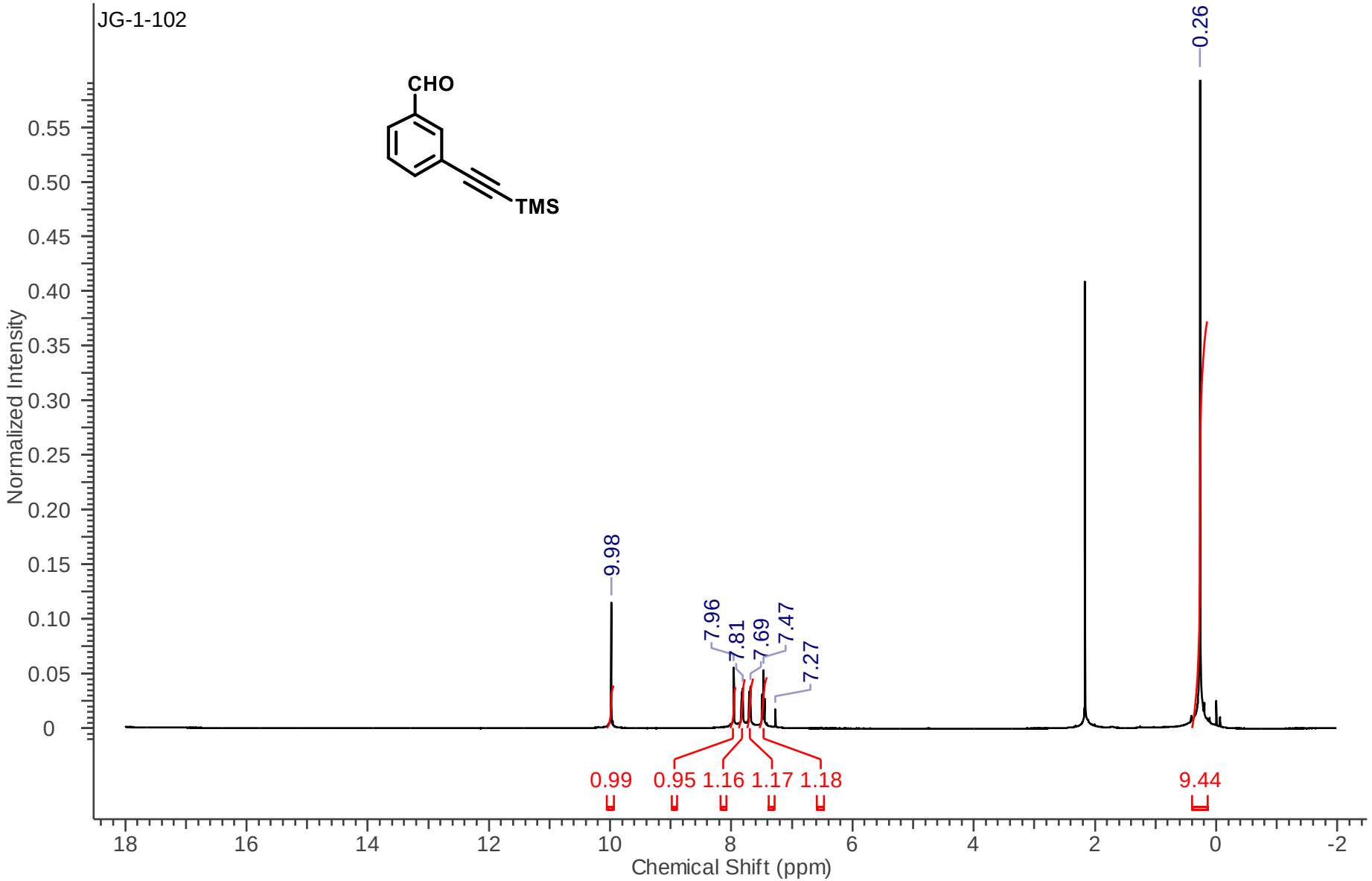
JG-1-102
CHO
TMS
Normalized Intensity
0.55
0.50
0.45
0.40
0.35
0.30
0.25
0.20
0.15
0.10
0.05
0
9.98
7.96
7.81
7.69
7.47
7.27
0.26
0.99
0.95
1.16
1.17
1.18
9.44
18
16
14
12
10
8
6
4
2
0
-2
Chemical Shift (ppm)

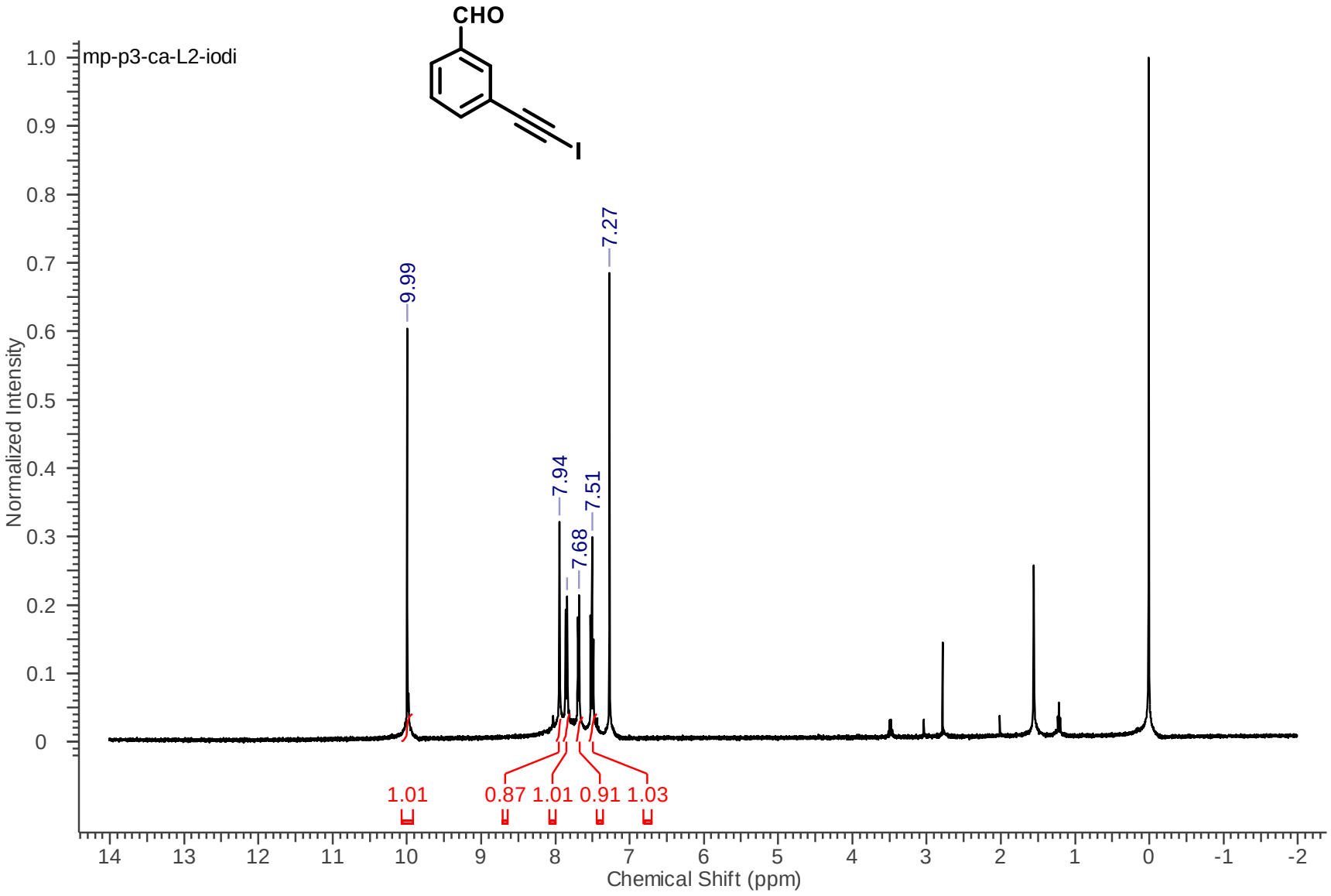
CHO
I
mp-p3-ca-L2-iodi
Normalized Intensity
Chemical Shift (ppm)
9.99
7.94
7.68
7.51
7.27
1.01
0.87
1.01
0.91
1.03

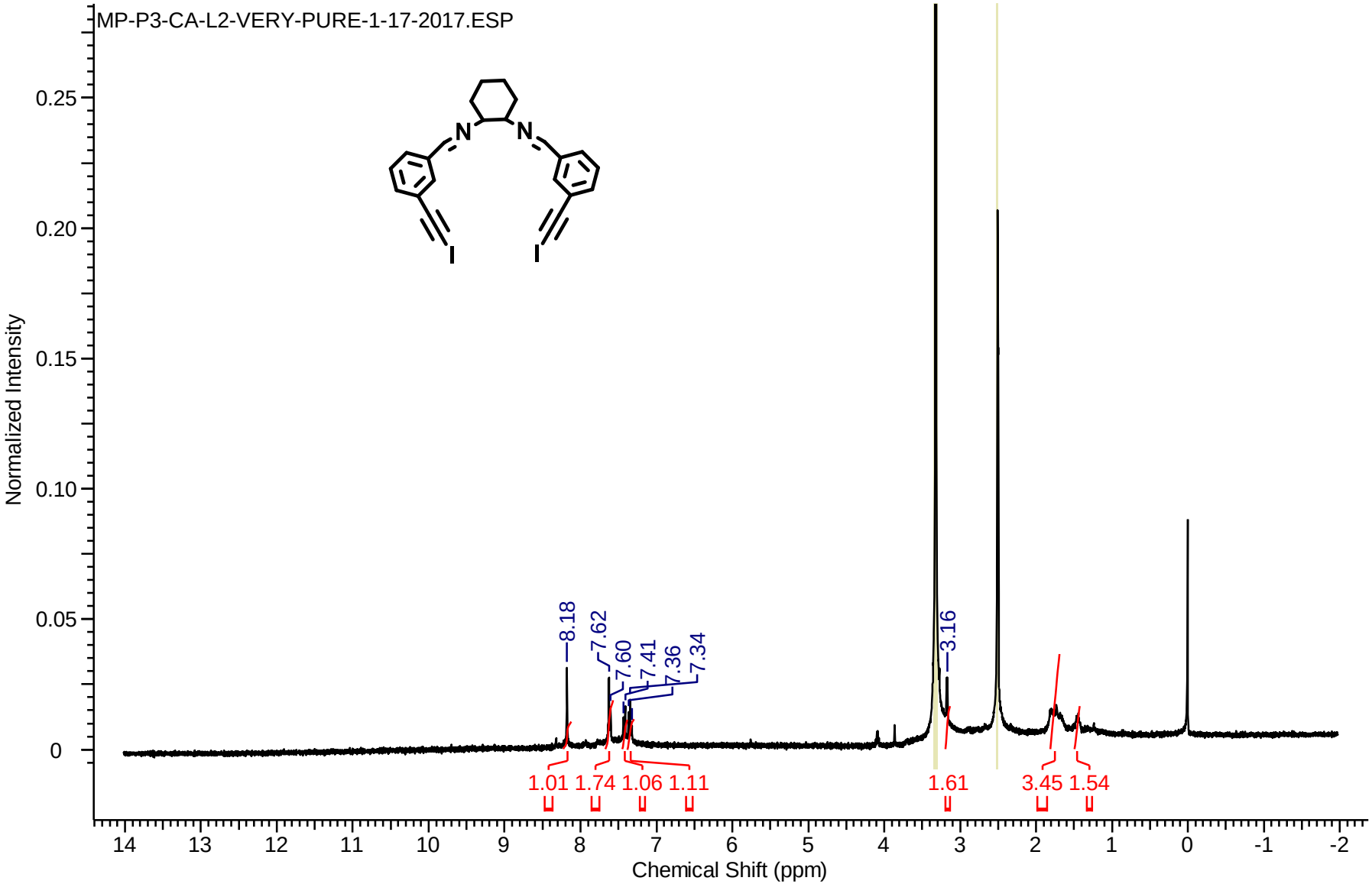
MP-P3-CA-L2-VERY-PURE-1-17-2017.ESP
N
N
I
I
Normalized Intensity
0.25
0.20
0.15
0.10
0.05
0
8.18
7.62
7.60
7.41
7.36
7.34
3.16
1.01
1.74
1.06
1.11
1.61
3.45
1.54
14
13
12
11
10
9
8
7
6
5
4
3
2
1
0
-1
-2
Chemical Shift (ppm)

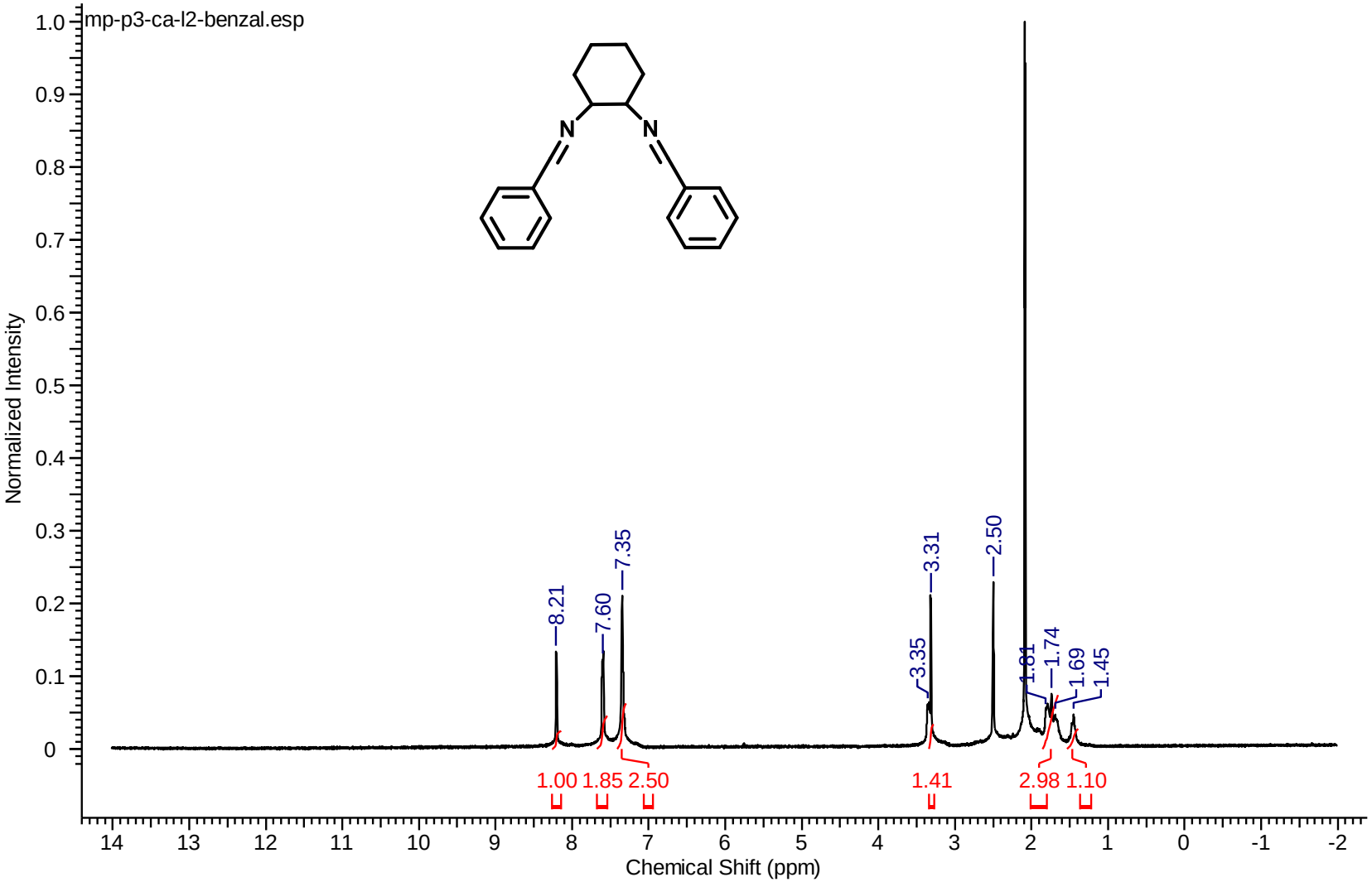
mp-p3-ca-l2-benzal.esp
N
N
Normalized Intensity
Chemical Shift (ppm)
8.21
7.60
7.35
3.35
3.31
2.50
1.81
1.74
1.69
1.45
1.00
1.85
2.50
1.41
2.98
1.10

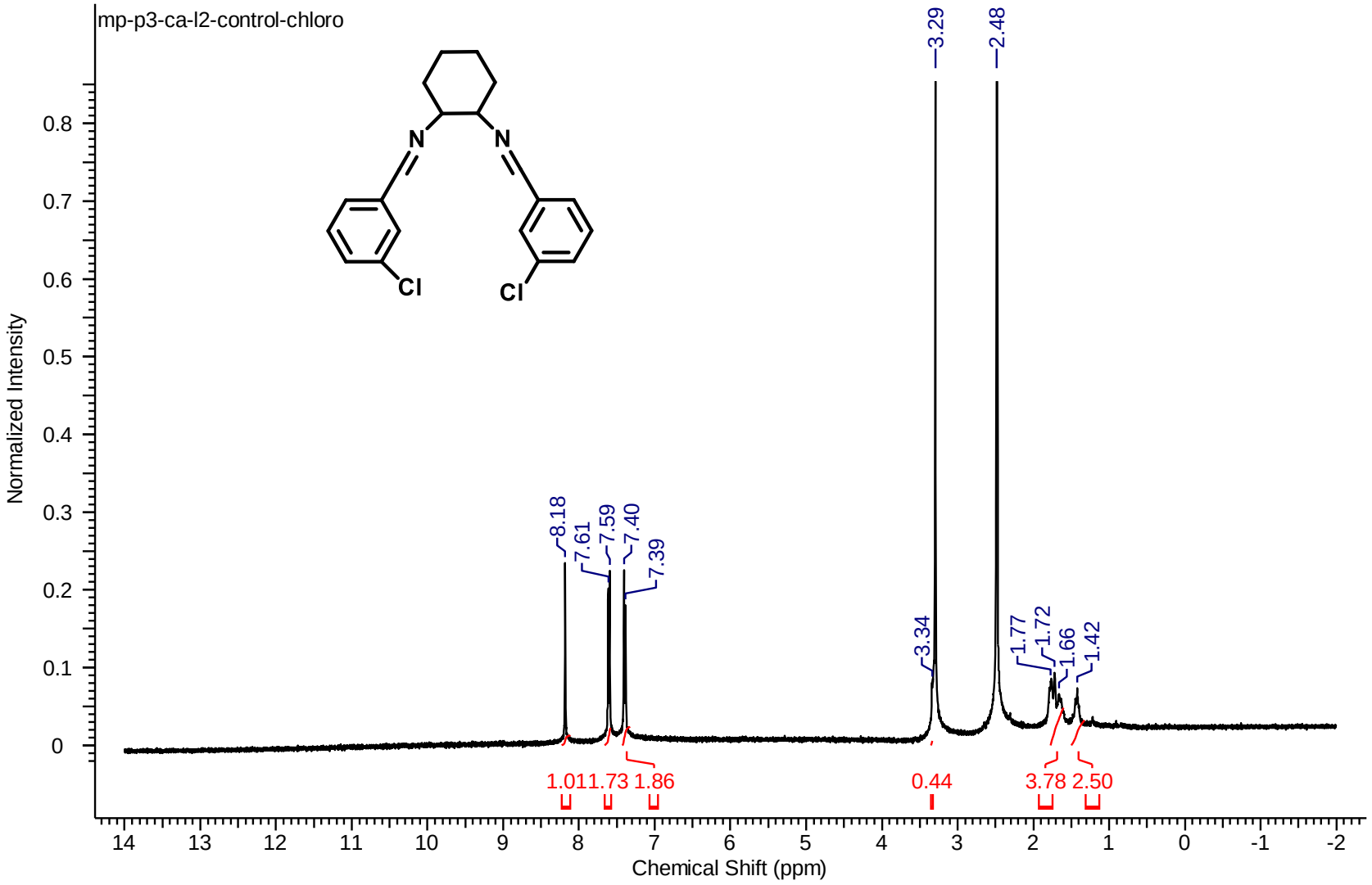
mp-p3-ca-l2-control-chloro
N
N
Cl
Cl
3.29
2.48
8.18
7.61
7.59
7.40
7.39
3.34
1.77
1.72
1.66
1.42
1.01
1.73
1.86
0.44
3.78
2.50
Normalized Intensity
Chemical Shift (ppm)

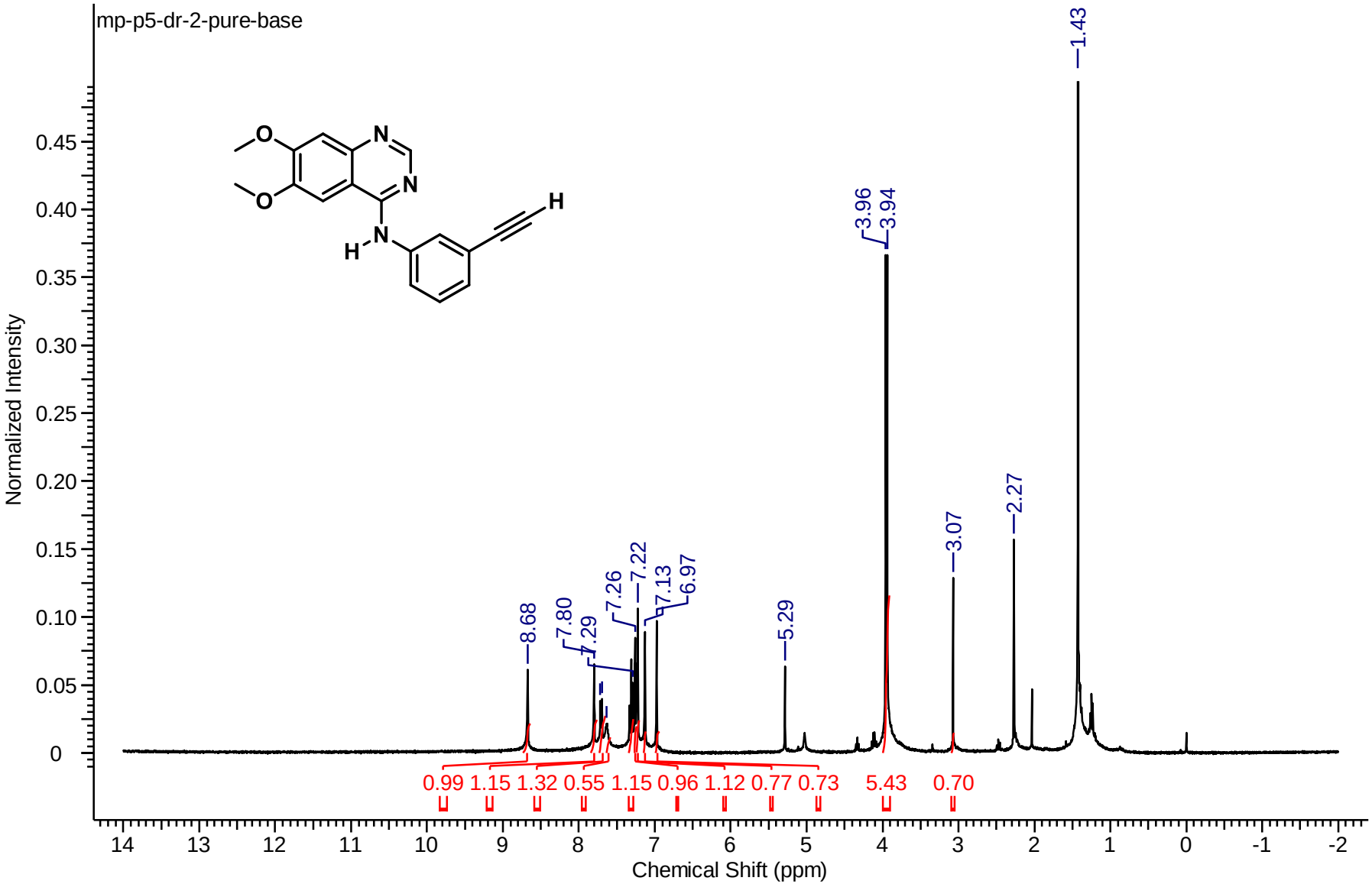
mp-p5-dr-2-pure-base
Normalized Intensity
Chemical Shift (ppm)
8.68
7.80
7.29
7.26
7.22
7.13
6.97
5.29
3.96
3.94
3.07
2.27
1.43
0.99 1.15 1.32 0.55 1.15 0.96 1.12 0.77 0.73 5.43 0.70

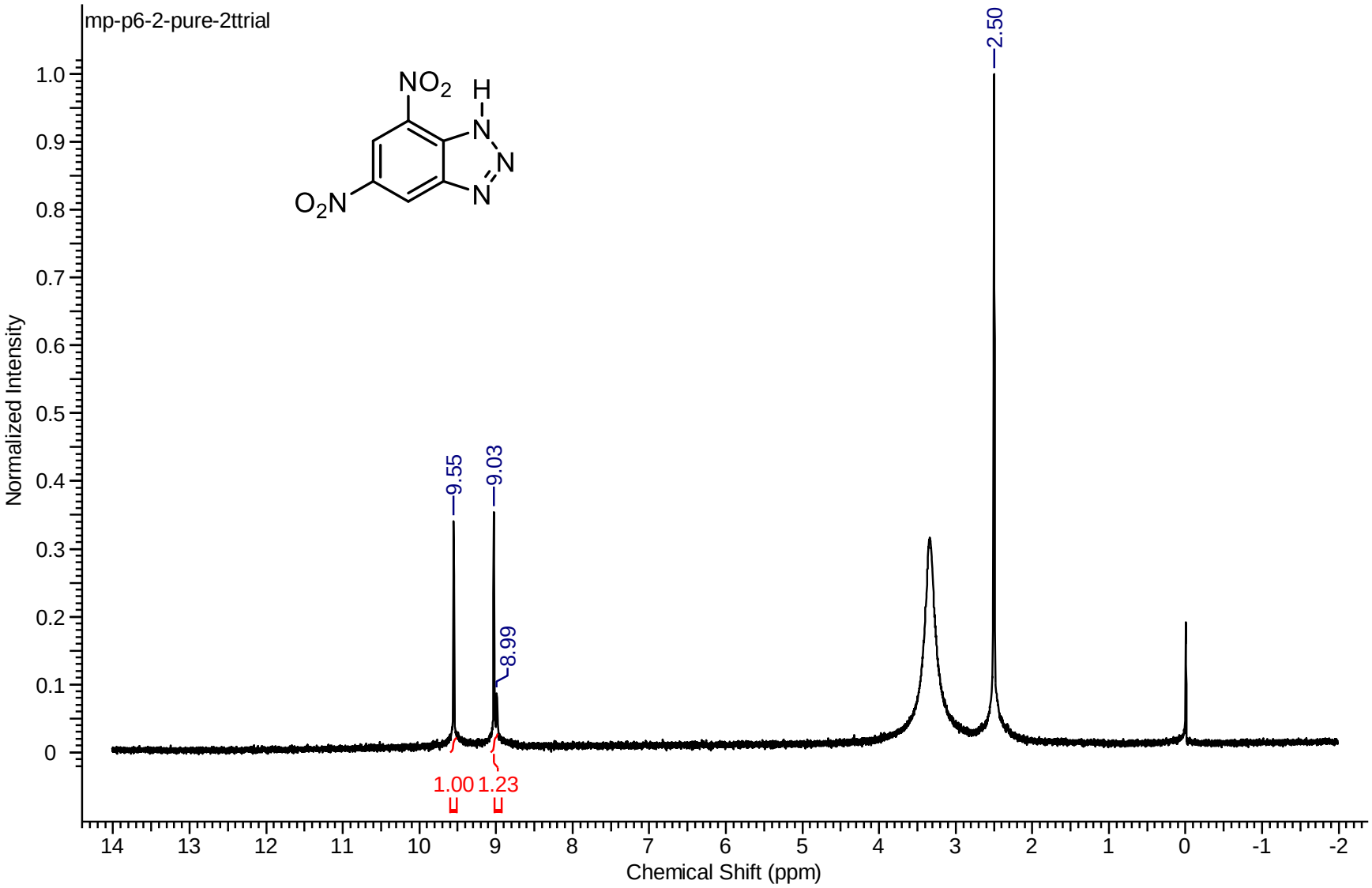
mp-p6-2-pure-2ttrial
NO2
H
N
N
N
O2N
2.50
9.55
9.03
8.99
1.00
1.23
Normalized Intensity
Chemical Shift (ppm)

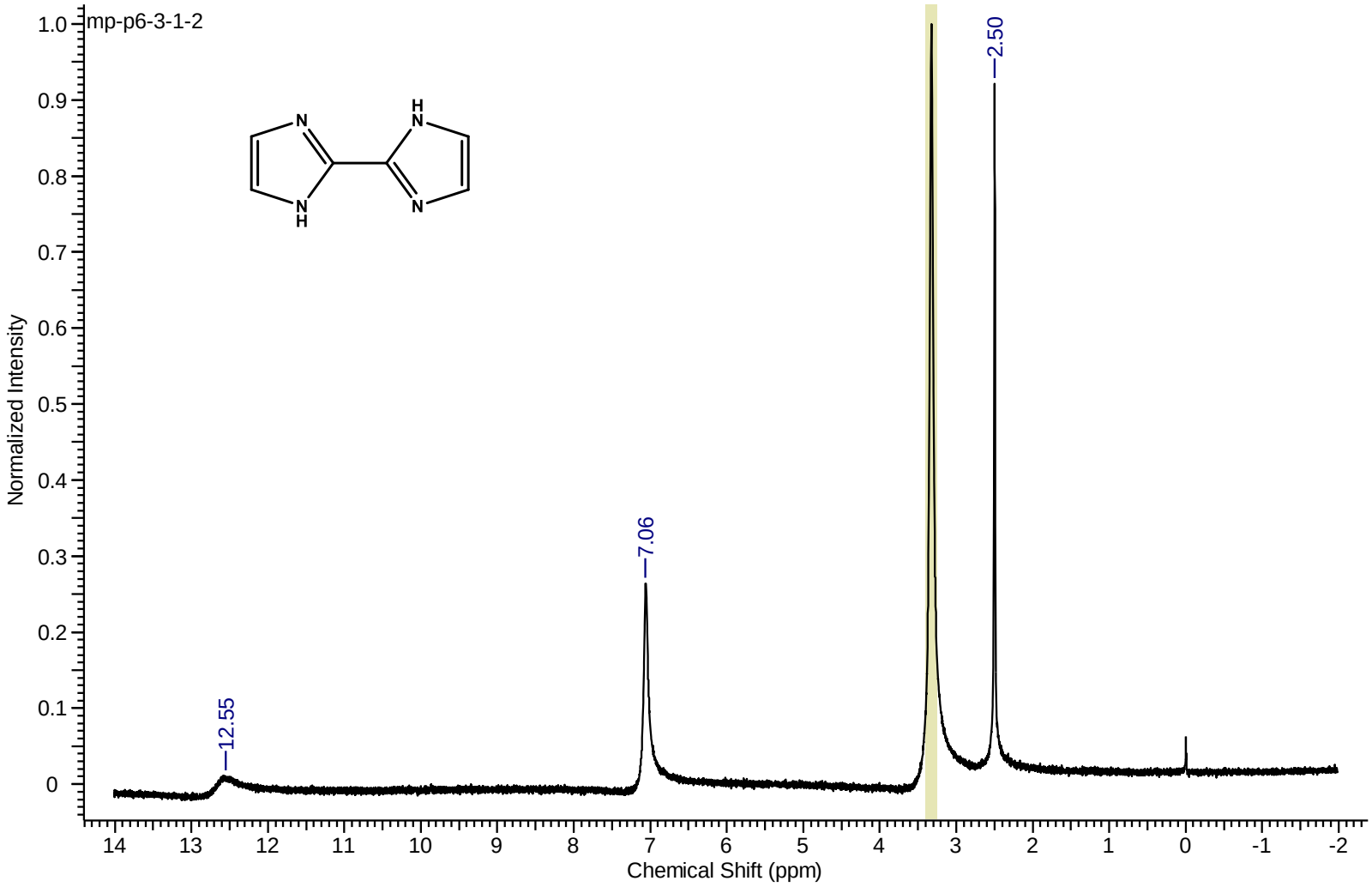
mp-p6-3-1-2
Normalized Intensity
Chemical Shift (ppm)
12.55
7.06
2.50

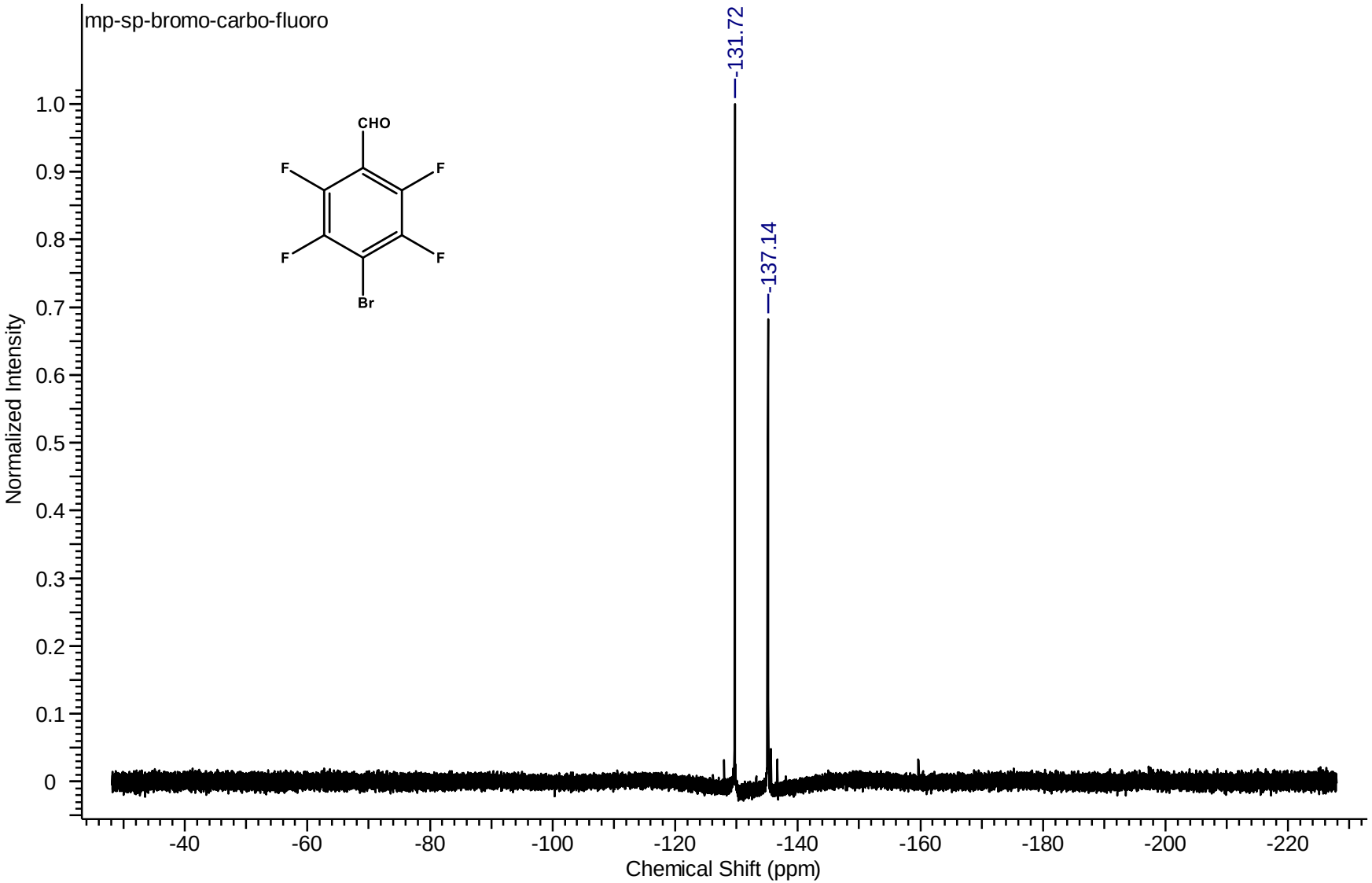
mp-sp-bromo-carbo-fluoro
-131.72
-137.14
CHO
F
F
F
F
Br
Normalized Intensity
1.0
0.9
0.8
0.7
0.6
0.5
0.4
0.3
0.2
0.1
0
-40
-60
-80
-100
-120
-140
-160
-180
-200
-220
Chemical Shift (ppm)

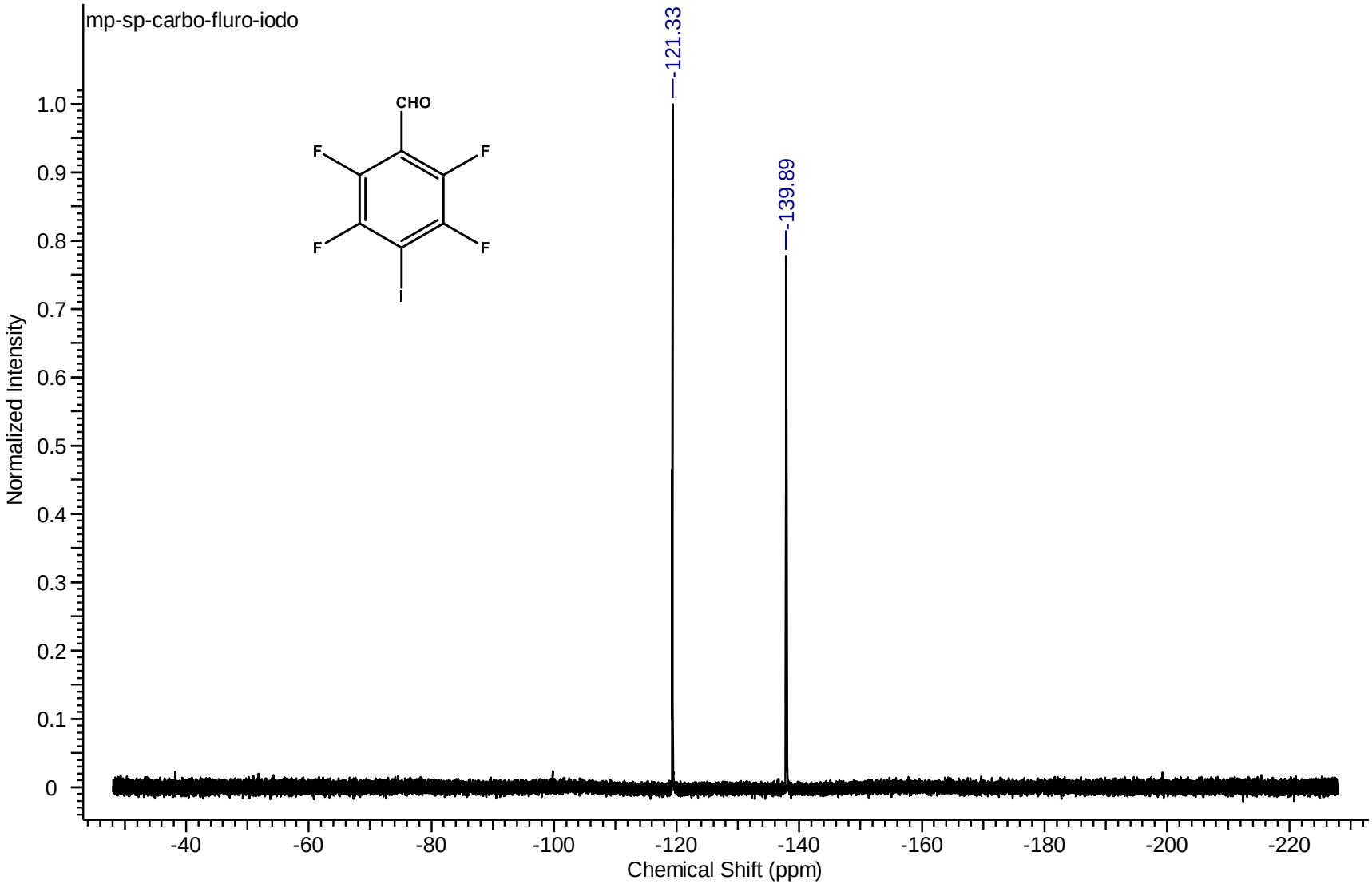
mp-sp-carbo-fluro-iodo
CHO
F
F
F
F
I
-121.33
-139.89
Normalized Intensity
1.0
0.9
0.8
0.7
0.6
0.5
0.4
0.3
0.2
0.1
0
-40
-60
-80
-100
-120
-140
-160
-180
-200
-220
Chemical Shift (ppm)

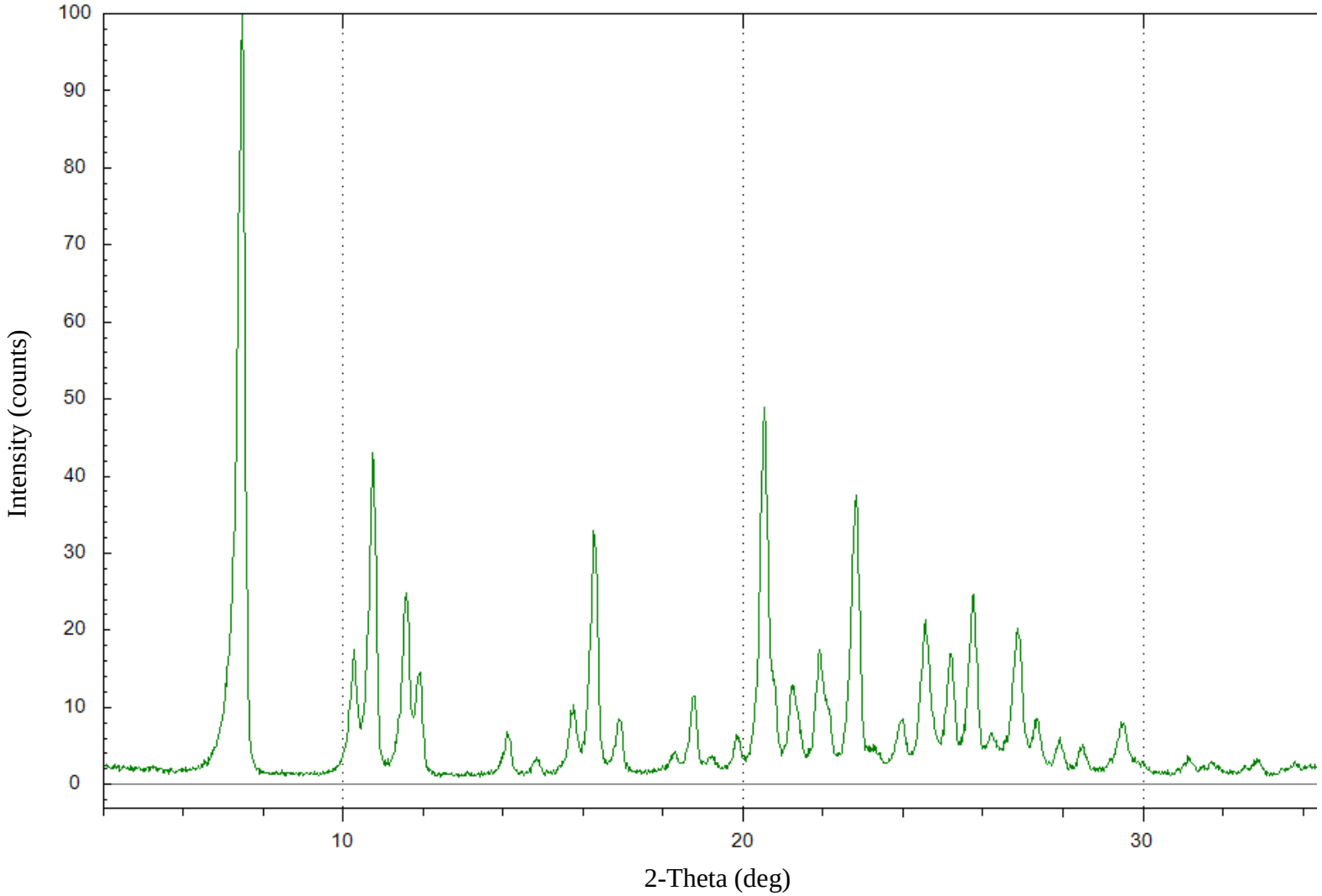

Powder pattern of **$(A1)_2$:DOD** co-crystal obtained through solvothermal method

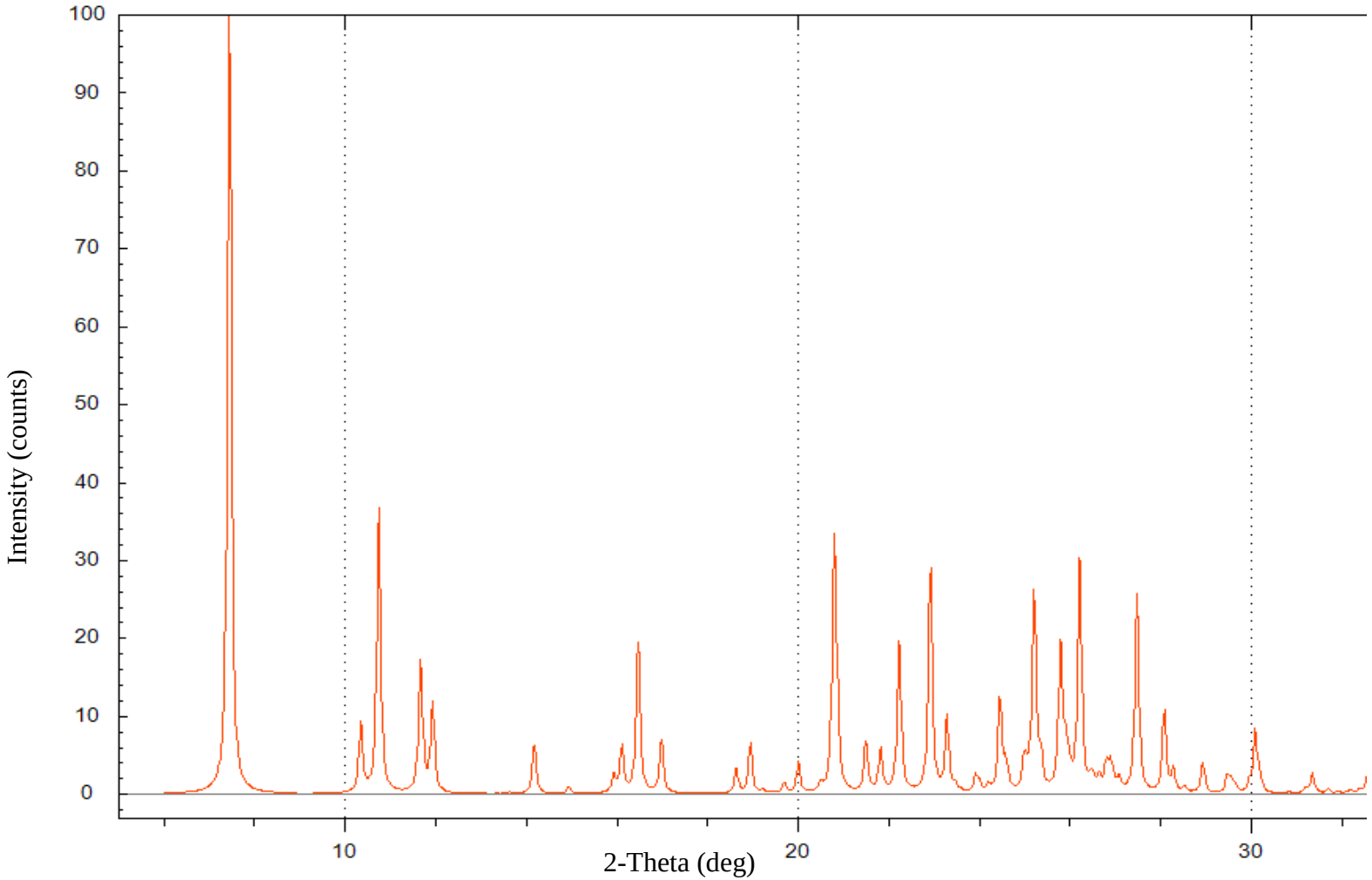

Stimulated powder pattern of **$(A1)_2$:DOD** co-crystal analysis

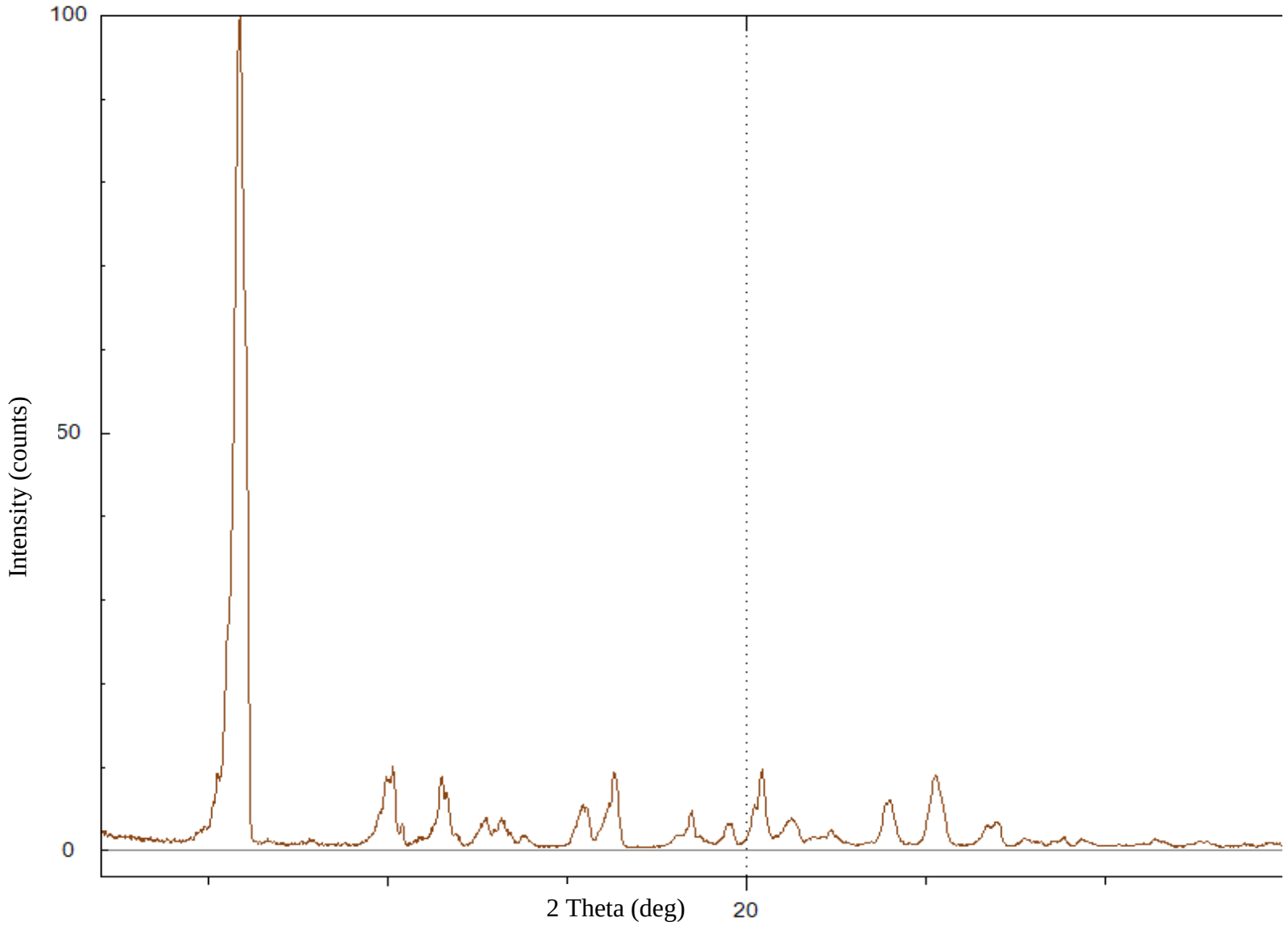

Powder patter of $(A1)_2$:SUB co-crystal obtained through solvothermal method

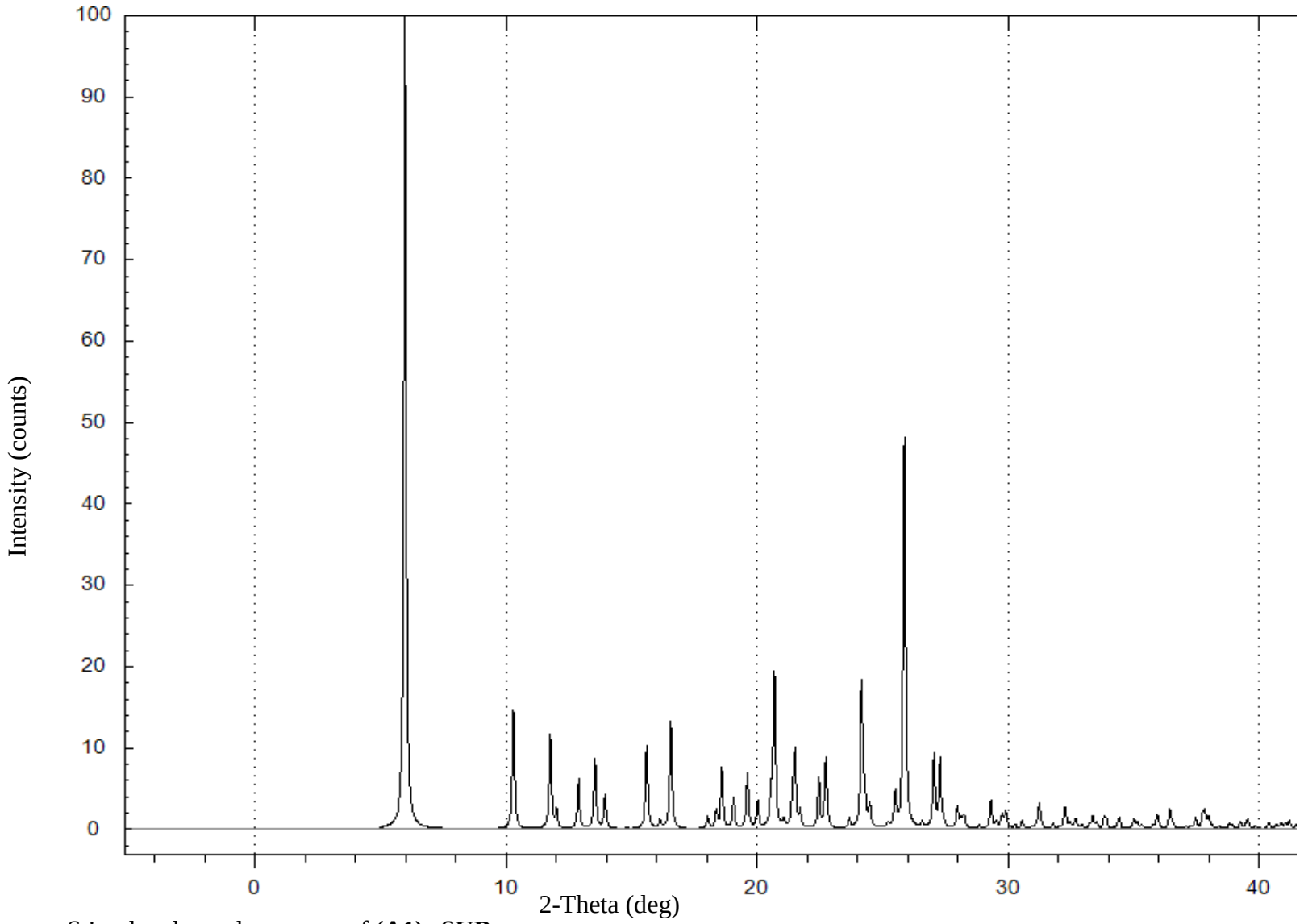

Stimulated powder pattern of **$(A1)_2$:SUB**

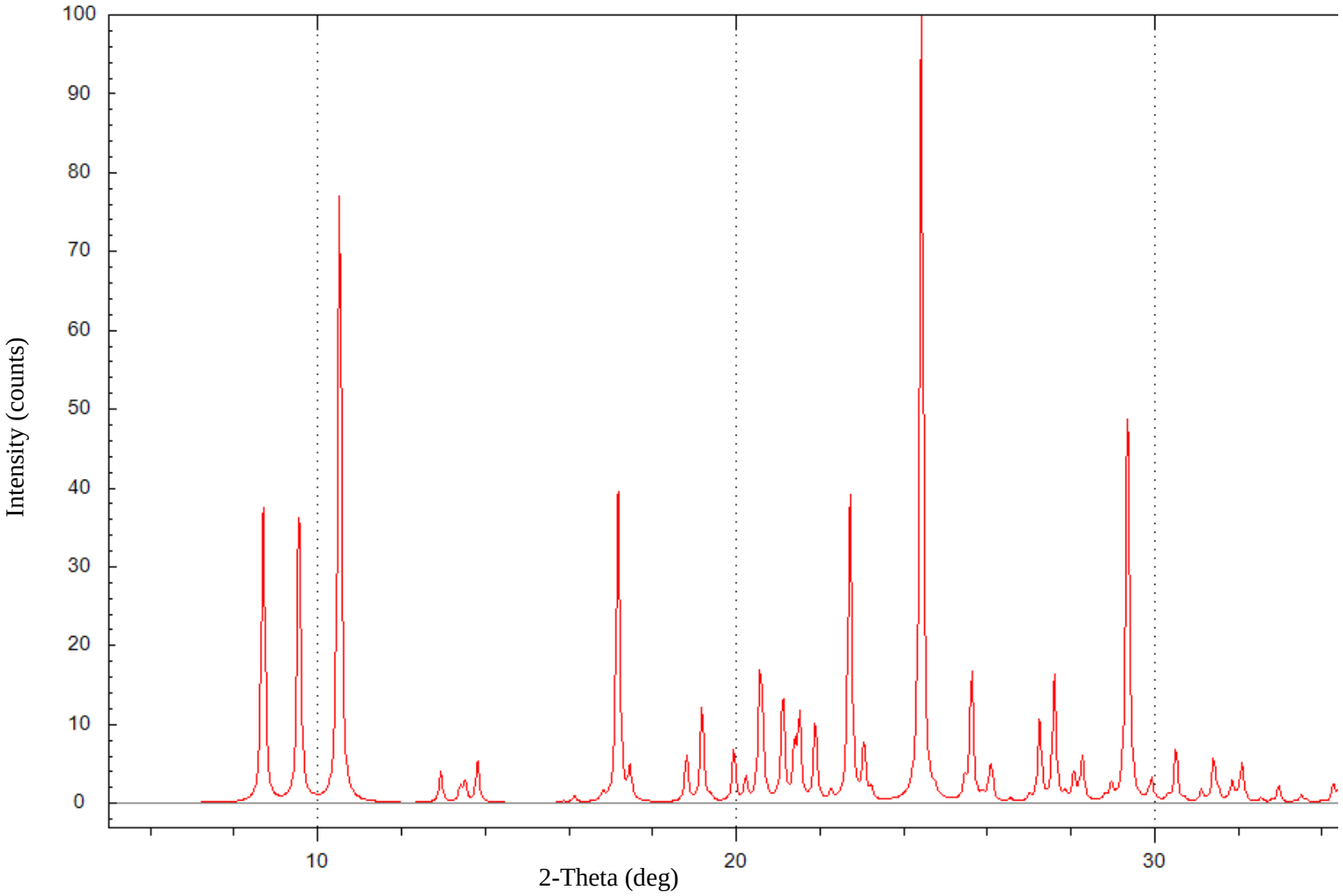

Stimulated powder pattern of **(A1)$_2$:SUC**

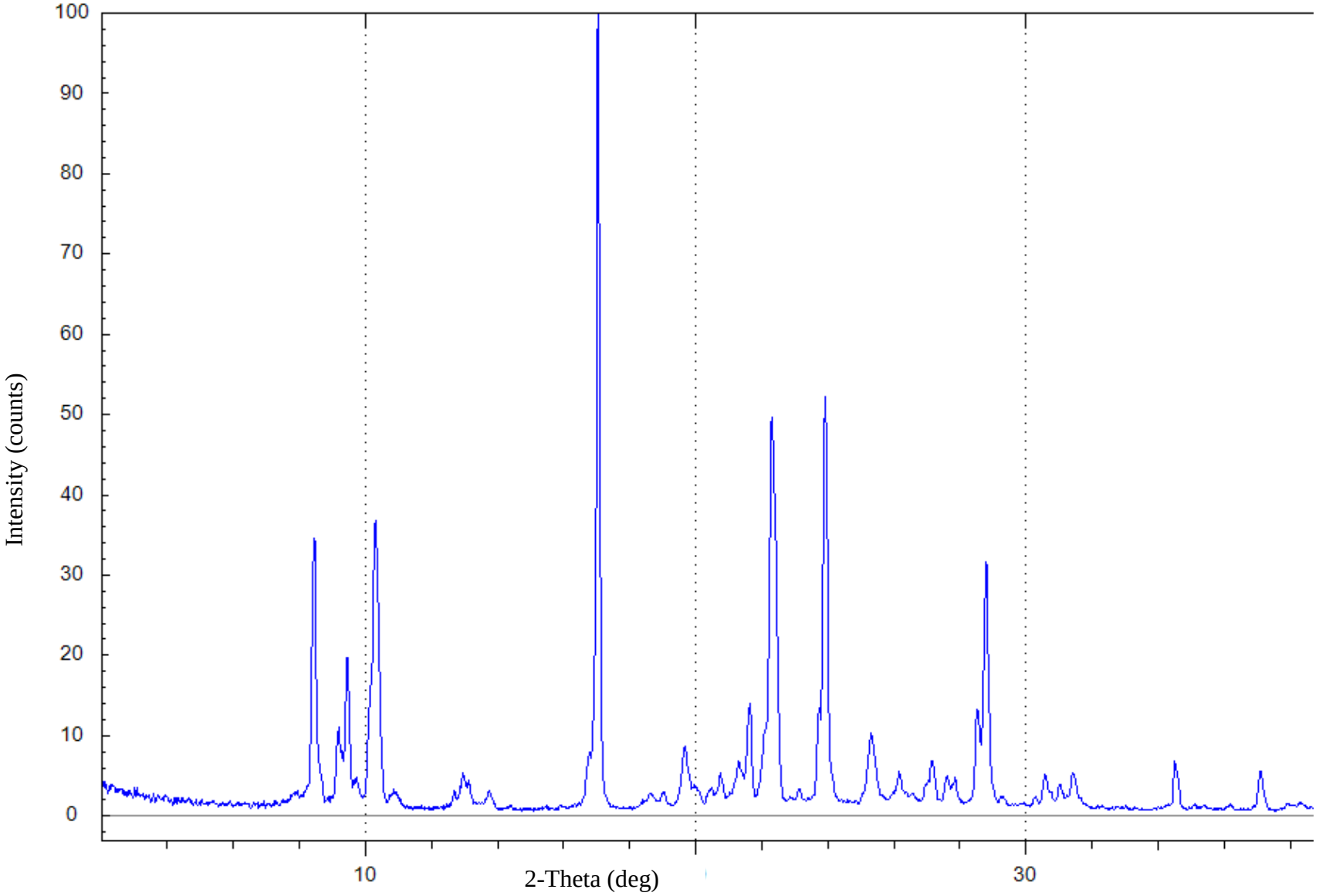

Powder pattern of **$(A1)_2$:SUC** obtained through solvothermal method